Swansea University

Faculty of Science and Engineering

New Time Integration Schemes for Computational Fluid and Structural Dynamics and Their Application in Staggered Fluid–Structure Interaction Solvers

Eman Alhayki

A thesis submitted to Swansea University in fulfilment of the requirements for the degree of Doctor of Philosophy

March 2025

Declarations

This work has not previously been accepted in substance for any degree and is not being concurrently submitted in candidature for any degree.

Signed: Eman Alhayki .....

Date: 10 November 2025 .....

This thesis is the result of my own investigations, except where otherwise stated. Other sources are acknowledged by footnotes giving explicit references. A bibliography is appended.

Signed: Eman Alhayki .....

Date: 10 November 2025 .....

I hereby give consent for my thesis, if accepted, to be available for photocopying and for interlibrary loan, and for the title and summary to be made available to outside organisations.

Signed: Eman Alhayki .....

Date: 10 November 2025 .....

The University's ethical procedures have been followed and, where appropriate, that ethical approval has been granted.

Signed: Eman Alhayki .....

Date: 10 November 2025 .....

Acknowledgements

I would like to express my sincere gratitude to my supervisor, Prof. Wulf Dettmer, for his consistent support, thoughtful feedback, and kind guidance throughout every stage of this journey. I was truly fortunate to have such an inspiring supervisor, who made this experience immensely enjoyable.

I am endlessly grateful to my family for their boundless love and support throughout this journey. Their encouragement, understanding, and unwavering belief in me gave me the strength to persevere, even during the most challenging times. None of this would have been possible without their constant presence in my life.

Abstract

Implicit time integration schemes are widely used in computational science and engineering, yet improving their accuracy and high-frequency damping characteristics remains an active area of research. This thesis introduces a novel family of implicit time integration schemes suitable for both first order and second order systems. The schemes are constructed as linear combinations of the well-known generalised-α method and its higher order extensions. The weighting of each component is determined using the Jury stability criterion, ensuring that the resulting methods are unconditionally stable. In addition to stability, the proposed methods offer improved second order accuracy and enhanced control over high-frequency numerical dissipation.

Subsequently, the newly formulated implicit schemes are applied in the context of computational fluid structure interaction and a family of staggered Dirichlet-Neumann coupling schemes is presented. The methods incorporate an enhanced second order predictor, developed using a strategy analogous to that employed in the formulation of the implicit schemes, and include a relaxation step to improve stability. Furthermore, a non-iterative n-cycle version of the staggered scheme is introduced, in which a predefined number of computational cycles is performed at each time step. The stability and accuracy of the proposed methods are analysed using a linear model problem involving a thin-walled elastic tube conveying fluid. Further validation is provided through a number of benchmark examples, demonstrating that the schemes are suitable for a wide range of added-mass cases.

Contents

List of Figures

List of Tables

Publications

The work presented in this thesis has contributed to the following publications

[1] W. G. Dettmer and E. Alhayki. “New implicit time integration schemes combining high frequency damping with high second order accuracy”. In: *Journal of Computational Physics* 514 (2024), pp. 113260.

[2] E. Alhayki and W. G. Dettmer. “New implicit time integration schemes for structural dynamics combining high frequency damping and high second order accuracy”. In: *Computers & Structures* 305 (2024), pp. 107587.

[3] E. Alhayki, W. G. Dettmer, and D. Perić. “An efficient non-intrusive strategy for weakly coupled fluid–structure interaction”. In: *Journal of Physics: Conference Series* 2647.5 (2024).

Chapter 1

Introduction

On 7 November 1940, the Tacoma Narrows Bridge suffered a catastrophic structural failure, widely regarded as one of the most significant events in the history of civil engineering. The collapse was caused by aeroelastic flutter, a dynamic instability arising from the interaction between aerodynamic forces and the structural motion of the bridge [1, 14].

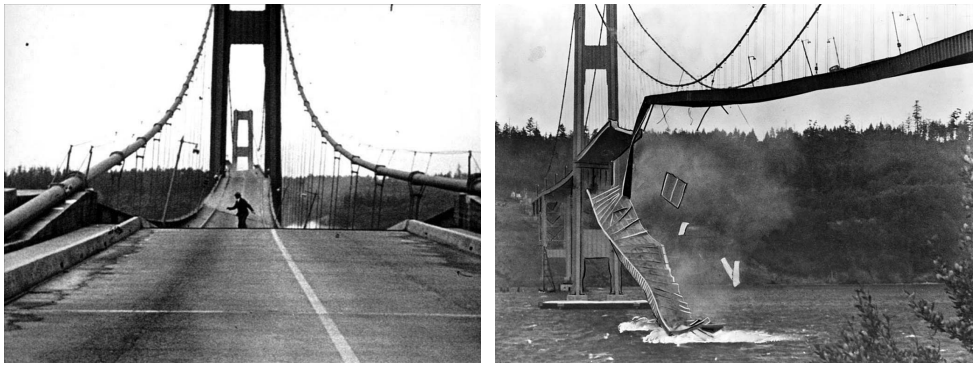

Figure 1.1.: Oscillations and collapse of the Tacoma Narrows Bridge [98].

This event showed that an insufficient understanding of fluid-structure interactions can lead to serious failures, highlighting the need for reliable mathematical and computational frameworks to simulate such coupled dynamics. Accurately modelling and interpreting these systems often requires the development of time-dependent mathematical models, typically expressed in the form of ordinary or partial differential equations (ODEs or PDEs). In

most practical cases, these equations are highly complex and cannot be solved analytically, and must therefore be approximated using numerical methods. Time integration schemes play a crucial role in these numerical approaches, as they capture the temporal evolution of the system.

Time integration schemes are typically classified as either explicit or implicit. Explicit methods calculate the future state of a system directly from its current state. These schemes are relatively straightforward to implement and computationally inexpensive per time step. However, they are conditionally stable, meaning the time step Δt must be sufficiently small to maintain numerical stability [83, 99, 115]. As a result, explicit methods become computationally inefficient for systems exhibiting stiffness, strong coupling, or fine spatial discretisation.

In contrast, implicit methods determine the future state by solving equations that involve both the current and future states. This approach requires solving a system of equations at each step, thereby increasing the computational cost. However, it offers unconditional stability for many classes of problems, allowing substantially larger time steps without compromising numerical robustness. These characteristics make implicit methods particularly well suited to stiff systems, coupled multiphysics simulations, and long-term integration [23, 117].

Despite their robust stability, the accuracy of implicit methods is inherently constrained by the second Dahlquist barrier, which states that the maximum order of accuracy for a linear A-stable implicit method is two. Moreover, for second order methods, the best possible error constant is $\frac{1}{12}$. The trapezoidal rule achieves this optimal error constant, making it the most accurate A-stable method of order two [5, 57]. However, the trapezoidal rule is known to provide insufficient numerical damping, which may result in non-physical oscillations, particularly in dynamic analyses involving high-frequency responses.

Extensive research has resulted in the development of several time integration schemes, including but not limited to the Newmark-β method [93], the Wilson-θ method [118], the WBZ-α method [118], the HHT-α method [63], and the generalised-α method [27]. Among these, the generalised-α method

is widely recognised for its effective combination of second order accuracy, numerical stability, and its ability to dampen high-frequency numerical noise while preserving low-frequency response characteristics. Although the method was initially developed for structural dynamics [27], the generalised-α method has since been applied across a wide range of disciplines. These include computational fluid dynamics [10, 36, 68, 77, 78], fluid–structure interaction [37, 62, 70, 74, 108], and biomechanics [79, 101], among others.

Despite recent progress, there is still a need for new time integration schemes that retain the strengths of existing methods while introducing improvements such as enhanced second order accuracy and reduced numerical dissipation, particularly for coupled problems where numerical formulations significantly affect stability and solution accuracy.

Fluid–structure interaction (FSI) refers to a class of coupled problems involving the dynamic interaction between a fluid domain and a solid or structural domain, where the motion of one directly influences the behaviour of the other. Such interactions are commonly observed in nature and are widely utilised across various engineering disciplines. Examples include aerofoils and engine blades in aerospace engineering [87]; prosthetic heart valves and drug delivery systems in biomedical engineering [48]; bridges and skyscrapers in civil engineering [107]; risers and offshore platforms in ocean engineering [123]; and piezoelectric devices and wind turbines in energy systems [58].

Numerical solution strategies in computational fluid-structure interaction are typically categorised as either monolithic or partitioned. Monolithic schemes solve the coupled fluid-structure system as a unified set of equations, which often results in improved numerical stability and convergence, particularly in cases involving strong coupling. However, the implementation of monolithic methods can be complex and computationally expensive, due to the need to formulate and solve large, coupled systems of equations. In contrast, partitioned schemes decouple the fluid and structural solvers, allowing each subdomain to be solved separately. The interaction between the fluid and structure is enforced through boundary conditions at their interface. This approach offers greater adaptability, as it enables the reuse of existing solvers with minimal modification and improves computational efficiency by avoiding large, fully

coupled systems. However, partitioned methods are more prone to numerical instabilities, particularly in cases involving incompressible flows and lightweight structures [12].

Partitioned methods can be further classified into weakly coupled (staggered) and strongly coupled schemes, as illustrated in Figure 1.2. Staggered schemes are favored for their ease of implementation and computational efficiency, as they typically solve the fluid and structural subproblems only once per time step. Coupling at the interface is commonly achieved using Dirichlet–Neumann boundary conditions, where one subproblem imposes displacement or velocity (Dirichlet), and the other returns forces (Neumann). This approach is widely adopted in commercial and industrial codes due to its simplicity and compatibility with existing solvers.

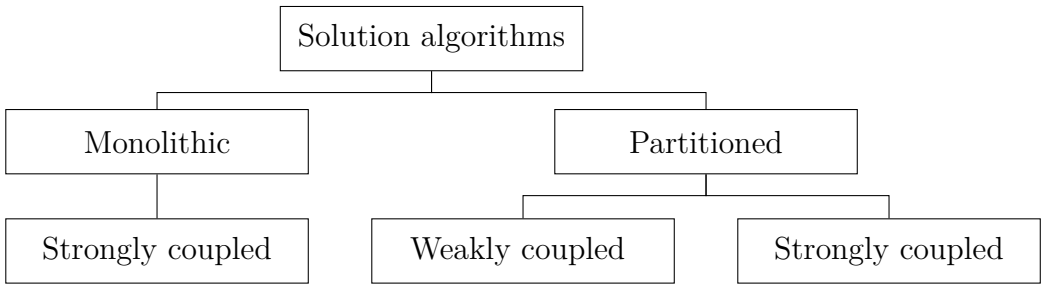

Figure 1.2.: Classification of different solution algorithms.

Despite ongoing progress in the field of computational fluid–structure interaction, staggered schemes based on Dirichlet–Neumann coupling continue to exhibit significant challenges related to stability and accuracy, which become particularly evident in the presence of strong added-mass effects, where the inertia of the surrounding fluid imposes significant dynamic loads on the structure [102]. Nevertheless, staggered schemes remain of interest due to their robustness, simplicity, and ease of integration with existing solvers. This motivates continued research into the development of new staggered methods aimed at improving their stability and accuracy without compromising computational efficiency. Achieving this would significantly enhance their suitability for simulating a broader class of complex FSI problems.

1.1. Objectives

The primary objective of this thesis is to develop a novel family of implicit time integration schemes that retain the key features of the generalised-α method, including second order accuracy, unconditional stability, and user-controlled high-frequency damping through the parameter ρ_∞, while also offering improved numerical dissipation and enhanced second order accuracy. The proposed schemes aim to address both first order problems common in fluid dynamics and second order problems encountered in structural dynamics, which makes them suitable for a wide range of applications. The second main objective is to utilise the proposed time integration schemes to develop new staggered methods for fluid-structure interaction problems based on Dirichlet-Neumann coupling. The aim is to present a practical and robust staggered solution strategy that remains stable and effective across a wide range of applications, offering a simpler alternative to fully coupled monolithic solvers.

1.2. Thesis Layout

This thesis is organised into five main chapters following the introduction, each addressing a key component of the research objectives.

Chapter 2 formulates a new family of implicit time integration schemes for first order problems by using a weighted linear combination of the generalised-α method and a new variant of the generalised-α method that achieves higher order accuracy. The chapter includes a detailed analysis of their stability, showing that the methods are unconditionally stable; accuracy, demonstrating that the schemes are second order accurate; and numerical damping characteristics. Several numerical examples are presented to illustrate the performance and robustness of the schemes.

Chapter 3 extends the time integration schemes formulated in Chapter 2 to second order problems. A comprehensive analysis is conducted to demonstrate that the schemes retain key properties, including unconditional stability,

second order accuracy, and controllable numerical damping. Several numerical benchmark problems are included to illustrate the effectiveness of the schemes in structural dynamics applications.

Chapter 4 discusses preliminary FSI concepts and introduces three staggered solution schemes, formulated using the time integration methods proposed in Chapters 2 and 3 for the fluid and solid subproblems, respectively. A theoretical analysis is carried out based on a linear model problem to assess the stability of the staggered schemes. The results show that the schemes are unconditionally stable up to a critical amount of added mass. In terms of accuracy, the schemes are shown to be second order accurate. The concept of multi-cycling is also introduced, and the advantages of multi-cycling are demonstrated.

Chapter 5 evaluates the proposed staggered schemes introduced in Chapter 4 by applying them to several benchmark problems in fluid–structure interaction, in both two-dimensional and three-dimensional settings. The problems are designed to challenge the schemes at their stability limits, allowing for a thorough assessment of their performance under strongly coupled interaction conditions.

Chapter 6 summarises the main contributions of the thesis, presents the concluding remarks, and outlines directions for future research.

Chapter 2

Time Integration Schemes for First Order Problems

Implicit time integration schemes are widely used in numerical simulations of dynamic systems, particularly when explicit methods become impractical due to stability constraints. In computational fluid dynamics, they are extensively used in a broad range of applications, including but not limited to simulating incompressible flows, modelling turbulence, and analysing compressible aerodynamics [9, 26, 41, 28, 78]. Likewise, in computational solid dynamics, these methods are applied across various problems, such as analysing nonlinear material properties, assessing structural deformations, and modelling contact mechanics, among other applications [2, 40, 43].

Since unconditional stability is a fundamental requirement for an implicit time integration scheme, its performance is evaluated based on two key factors, the accuracy with which it approximates the solution and its ability to control high frequency numerical oscillations [60]. However, while implicit methods guarantee stability, their accuracy is restricted to first or second order due to the second Dahlquist barrier and cannot exceed the accuracy of the trapezoidal rule [30, 66]. Yet, the trapezoidal rule lacks numerical damping, which can be problematic in fluid and solid dynamics, where unresolved high frequency responses must be suppressed. Hence, an optimal implicit scheme should achieve second order accuracy with small absolute error values while introducing moderate numerical damping in the high frequency regime.

The generalised-α method is particularly well suited for this, as it provides second order accuracy and user-controlled high frequency damping via the parameter ρ_∞ [27, 68]. For specific values of ρ_∞, the method recovers several well-known time integration schemes. For $\rho_\infty = 1$, it reduces to the trapezoidal rule, which is also equivalent to the Crank-Nicolson method [29]. For $\rho_\infty = 0$, it coincides with the second order backward difference formula BDF-2 [54] and aligns with the Wilson θ-method [118] and the Houbolt method [64].

This chapter introduces new implicit time integration schemes developed based on the generalised-α method for first order problems. These schemes maintain second order accuracy, unconditional stability, and user-controlled high frequency damping through ρ_∞, while offering improved accuracy and enhanced numerical damping. For $\rho_\infty = 0$, the new methods reduce to new, more accurate second order backward difference formulae, while for $\rho_\infty = 1$, they recover the trapezoidal rule.

2.1. Time Integration Schemes of Order p

Consider the first order initial value problem of the form

$$\dot{u}(t) \; - \; f(u(t), t) \; = \; 0, \quad \text{with} \quad u(0) \; = \; u_0, \tag{2.1}$$

where u is the solution variable, t represents time, and $\dot{u} = \mathrm{d}u/\mathrm{d}t$. To simplify the analysis of numerical time integration schemes, it is common practice to consider the special case of the scalar linear problem

$$\dot{u}(t) \; - \; \lambda\, u(t) \; = \; 0, \quad \text{with} \quad u(0) \; = \; u_0, \tag{2.2}$$

where $\lambda = -\xi + i\,\omega$. The exact solution can be expressed as

$$u(t) \; = \; u_0\, e^{\lambda\, t}. \tag{2.3}$$

By introducing a sequence of discrete time instants t_n for $n = 0, 1, 2, \ldots$ and defining the step size as $\Delta t = t_{n+1} - t_n$, the evolution of the numerical solution can be expressed in discrete form, giving rise to the exact amplification factor

$$\zeta_{\text{exact}} \;=\; e^{\lambda\,\Delta t}, \quad \text{with} \quad u_{n+1} \;=\; \zeta_{\text{exact}}\, u_n. \tag{2.4}$$

A general family of implicit time integration schemes can be formulated as

$$\dot{u}_{n+\beta} \;-\; \lambda\, u_{n+\alpha} \;=\; 0 \tag{2.5}$$

$$u_{n+\alpha} \;=\; \alpha\, u_{n+1} \;+\; (1-\alpha)\, u_n \tag{2.6}$$

$$u_{n+\beta} \;=\; \beta_0\, \dot{u}_{n+1} \;+\; \sum_{i=1}^{p-1} \beta_i\, u_n^{(i)'}\, \Delta t^{i-1} \tag{2.7}$$

$$u_{n+1}^{(i)'} = u_n^{(i)'} + \Delta t\, \left(\gamma\, u_{n+1}^{(i+1)'} + (1-\gamma)\, u_n^{(i+1)'}\right) \tag{2.8}$$

with $p \geq 2$ defining the number of terms in the formulation, the term $u_n^{(i)'}$ represents the i-th derivative of u at the discrete time instant t_n, where $i = 0, 1, 2, \ldots, p-2$. The numerical properties of these schemes and the conditions for the scalar parameters α, β_i, and γ are determined as follows. First, the associated amplification matrix $\mathbf{A}^{(p)}$ of the schemes is introduced. It is defined as

$$\left\{ \begin{array}{c} u_{n+1} \\ \dot{u}_{n+1}\, \Delta t \\ u_{n+1}^{(2)'}\, \Delta t^2 \\ \cdots \\ u_{n+1}^{(p-1)'}\, \Delta t^{p-1} \end{array} \right\} = \mathbf{A}^{(p)} \left\{ \begin{array}{c} u_n \\ \dot{u}_n\, \Delta t \\ u_n^{(2)'}\, \Delta t^2 \\ \cdots \\ u_n^{(p-1)'}\, \Delta t^{p-1} \end{array} \right\}. \tag{2.9}$$

The matrix $\mathbf{A}^{(p)}$ is of size $p \times p$ and can be determined using symbolic mathematical software. For $p = 4$, it is explicitly written as

$$\mathbf{A}^{(4)} = \frac{1}{\delta} \begin{bmatrix} \delta + \gamma\lambda\Delta t & \beta_0\eta - \beta_1\gamma & -\beta_2\gamma & -\beta_3\gamma \\ \lambda\Delta t & \alpha\eta\lambda\Delta t - \beta_1 & -\beta_2 & -\beta_3 \\ \dfrac{\lambda\Delta t}{\gamma} & \dfrac{\alpha\lambda\Delta t - \beta_0 - \beta_1}{\gamma} & -\dfrac{\delta\eta + \beta_2}{\gamma} & -\dfrac{\beta_3}{\gamma} \\ \dfrac{\lambda\Delta t}{\gamma^2} & \dfrac{\alpha\lambda\Delta t - \beta_0 - \beta_1}{\gamma^2} & -\dfrac{\delta + \beta_2}{\gamma^2} & -\dfrac{\gamma\delta\eta + \beta_3}{\gamma^2} \end{bmatrix} \tag{2.10}$$

where $\delta = \beta_0 - \alpha\gamma\lambda\Delta t$ and $\eta = 1 - \gamma$. The amplification matrices $\mathbf{A}^{(2)}$ and $\mathbf{A}^{(3)}$ correspond to the top left submatrices of $\mathbf{A}^{(4)}$ with dimensions 2×2 and 3×3, respectively.

To analyse numerical accuracy, it is convenient to first examine the high frequency damping behaviour of the schemes. The spectral radius of the matrix $\mathbf{A}^{(p)}$ is given by

$$\rho(\mathbf{A}^{(p)}) = \max\left(|\zeta_i|\right), \tag{2.11}$$

where ζ_i with $i = 1, 2, \ldots, p$ are the eigenvalues of $\mathbf{A}^{(p)}$. For an infinite time step, the spectral radius ρ_∞ is expressed as

$$\rho_\infty = \lim_{\Delta t \to \infty} \rho(\mathbf{A}^{(p)}) = \max\left(\left|\frac{1-\alpha}{\alpha}\right|, \left|\frac{1-\gamma}{\gamma}\right|\right). \tag{2.12}$$

Setting

$$\alpha = \gamma = \frac{1}{1+\rho_\infty} \tag{2.13}$$

ensures that the absolute values of all eigenvalues converge to ρ_∞ as Δt tends to infinity.

To evaluate the accuracy of the family of schemes defined by Equations (2.5) to (2.8), the amplification factor ζ_{exact} is substituted into the characteristic polynomial of $\mathbf{A}^{(p)}$. The resulting expression is then expanded as a power series in Δt. By equating the first p terms of series the to zero, an accuracy of order p is achieved, and a set of equations is obtained to solve for the coefficients β_i, where $i = 0, 1, 2, \ldots, p-1$. This procedure is implemented using symbolic mathematical software, and the resulting expressions for β_i are summarised in Box 1.

Hence, by using Equation (2.13) and the coefficients defined in Box 1, the resulting schemes achieve an accuracy of order p and are referred to as the *generalised-α method of order p*, or *GA-p*. The formulated schemes allow for user-controlled high frequency damping, with ρ_∞ being the only free parameter, constrained within the range $0 \leq \rho_\infty \leq 1$.

For $p = 2$:

$$\beta_0 = \frac{-\rho_\infty + 3}{2(\rho_\infty + 1)} \qquad \beta_1 = \frac{3\rho_\infty - 1}{2(\rho_\infty + 1)}$$

For $p = 3$:

$$\beta_0 = \frac{2\rho_\infty^2 - 5\rho_\infty + 11}{6(\rho_\infty + 1)} \quad \beta_1 = \frac{-2\rho_\infty^2 + 11\rho_\infty - 5}{6(\rho_\infty + 1)} \quad \beta_2 = \frac{-\rho_\infty^2 + \rho_\infty - 1}{3(\rho_\infty + 1)}$$

For $p = 4$:

$$\beta_0 = \frac{-3\rho_\infty^3 + 7\rho_\infty^2 - 13\rho_\infty + 25}{12(\rho_\infty + 1)} \qquad \beta_1 = \frac{3\rho_\infty^3 - 7\rho_\infty^2 + 25\rho_\infty - 13}{12(\rho_\infty + 1)}$$

$$\beta_2 = \frac{3\rho_\infty^3 - 7\rho_\infty^2 + 7\rho_\infty - 7}{12(\rho_\infty + 1)} \qquad \beta_3 = \frac{\rho_\infty^3 - \rho_\infty^2 + \rho_\infty - 1}{4(\rho_\infty + 1)^2}$$

Box 1: Coefficients β_i for the family of time integration schemes GA-p.

Remark 2.1.1: As presented in Equations (2.5) to (2.8), the scheme is not suitable for $p = 1$. However, an alternative unconditionally stable first order scheme, known as the generalised midpoint rule (GM), can be obtained by setting $p = 1$ and $\gamma = 1$ (see [36]). For $\rho_\infty = 0$, it recovers the first order backward Euler method. For $\rho_\infty = 1$, it recovers the second order trapezoidal rule, which is known for its minimal truncation error and lack of numerical dissipation [31]. For convenience, the GM scheme is summarised in Box 2.

Remark 2.1.2: The family of time integration schemes defined by Equations (2.5) to (2.8) is unconditionally stable only for $p = 2$. This is illustrated in Figure 2.1, which presents the spectral radii $\rho(\mathbf{A}^{(p)})$ of GM, GA-2, GA-3, and GA-4. For the method to achieve unconditional stability, the spectral radius must not exceed 1 for all values of Δt.

Remark 2.1.3: For $\rho_\infty = 0$, the proposed family of schemes is identical to the well-known backward difference formulae of order p. This is further elaborated in Section 2.4.

Remark 2.1.4: For $p = 2$, the formulated scheme coincides with the well-known generalised-α method proposed in [68]. By replacing the parameters α, β_0, and β_1 with α_f, α_m, and $1 - \alpha_m$, respectively, the formulation presented in [68] is recovered. For convenience, the GA-2 scheme is summarised in Box 3.

$$
\begin{aligned}
\dot{u}_{n+\alpha} \;-\; f(u_{n+\alpha},\, t_{n+\alpha}) \;&=\; 0 \\
u_{n+\alpha} \;&=\; \alpha\, u_{n+1} \;+\; (1-\alpha)\, u_n \\
\dot{u}_{n+\alpha} \;&=\; \frac{u_{n+1} - u_n}{\Delta t} \\
\alpha \;&=\; \frac{1}{1+\rho_\infty}
\end{aligned}
$$

Box 2: Summary of the generalised midpoint rule method GM.

$$
\begin{aligned}
\dot{u}_{n+\beta} \;-\; f(u_{n+\alpha},\, t_{n+\alpha}) \;&=\; 0 \\
u_{n+\alpha} \;&=\; \alpha\, u_{n+1} \;+\; (1-\alpha)\, u_n \\
\dot{u}_{n+\beta} \;&=\; \beta_0\, \dot{u}_{n+1} \;+\; \beta_1\, \dot{u}_n \\
u_{n+1} \;&=\; u_n \;+\; (\gamma\, \dot{u}_{n+1} \;+\; (1-\gamma)\; \dot{u}_n)\; \Delta t \\
\alpha = \gamma = \frac{1}{1+\rho_\infty}, \quad \beta_0 &= \frac{3-\rho_\infty}{2(1+\rho_\infty)}, \quad \beta_1 = \frac{-1+3\rho_\infty}{2(1+\rho_\infty)}.
\end{aligned}
$$

Box 3: Summary of method GA-2 (equivalent to the generalised-α method).

2.2. Ensuring Unconditional Stability

The GA-p method, introduced in Section 2.1, is unconditionally stable only for $p = 2$. However, to improve accuracy while maintaining unconditional stability, the following variation of Equation (2.5) is considered

$$
\delta_3\, \dot{u}^{(3)}_{n+\beta} \;+\; (1-\delta_3)\, \dot{u}^{(2)}_{n+\beta} \;-\; \lambda\, u_{n+\alpha} \;=\; 0, \tag{2.14}
$$

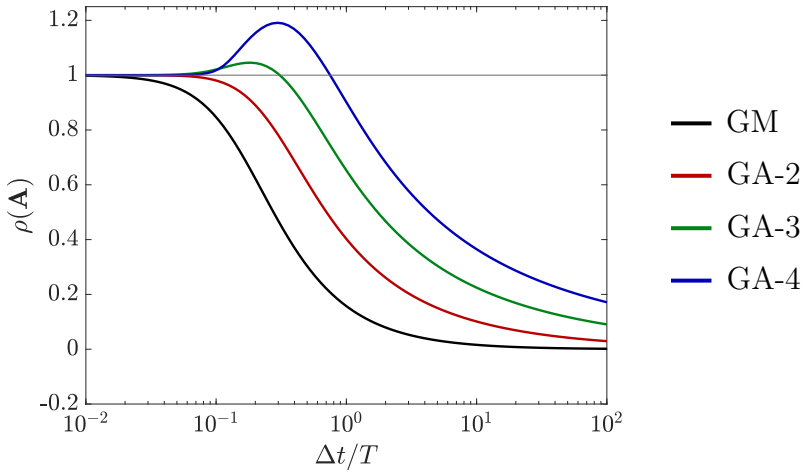

Figure 2.1.: Spectral radii of GM, GA-2, GA-3, and GA-4 for $\rho_\infty = 0$ and $\xi = 0$.

where $u_{n+\beta}^{(j)}$ is defined by Equation (2.7) with $p = j$. The coefficients β_i in Equation (2.7) are provided in Box 1 and must also be selected for $p = j$.

Equation (2.14) represents the linear combination of the GA-2 and GA-3 schemes. For $\delta_3 = 0$, the scheme reduces to GA-2 which is unconditionally stable. For $\delta_3 = 1$, the scheme recovers GA-3, which offers higher accuracy but is only conditionally stable. Clearly, it is desirable to find the largest possible value for $\delta_3 \geq 0$ that ensures unconditional stability.

The Jury Stability Criterion [71, 72, 105] is a method used to determine the stability of discrete-time linear systems. It assesses the coefficients of the characteristic equation by systematically arranging them in a structured table, known as the Jury table. Specific mathematical conditions are then applied to check whether all poles of the system lie within the unit circle in the complex plane. The criterion serves as a suitable tool for this investigation. However, the analytical procedure is tedious and results in lengthy algebraic expressions. To simplify the process, symbolic mathematical software was employed to carry out the derivations. The detailed analytical steps are presented in Appendix A. The resulting optimal δ_3 is

$$\delta_3 = \frac{(1-\rho_\infty)^2}{2(1-\rho_\infty+\rho_\infty^2)}. \tag{2.15}$$

For $\rho_\infty = 0$, one obtains $\delta_3 = \frac{1}{2}$, which corresponds to an equal weighting of the second and third order accurate terms. As ρ_∞ increases and approaches the value of 1, the weighting of GA-3 decreases, and the method eventually recovers the trapezoidal rule. The time integration scheme described by Equations (2.14), (2.6), (2.7), (2.8), (2.13), and (2.15), together with the relevant expressions from Box 1, is referred to as GA-23. The full set of equations describing GA-23 is summarised in Box 4.

$$\dot{u}_{n+\beta} \; - \; f(u_{n+\alpha},\, t_{n+\alpha}) \; = \; 0$$

$$u_{n+\alpha} \; = \; \alpha\, u_{n+1} \; + \; (1-\alpha)\, u_n$$

$$\dot{u}_{n+\beta} \; = \; \beta_0\, \dot{u}_{n+1} \; + \; \beta_1\, \dot{u}_n \; + \; \beta_2\, \ddot{u}_n\, \Delta t$$

$$u_{n+1}^{(i)'} \; = \; u_n^{(i)'} \; + \; \Big(\gamma\, u_{n+1}^{(i+1)'} \; + \; (1-\gamma)\; u_n^{(i+1)'}\Big)\, \Delta t \quad \text{for} \;\; i = 0,\, 1$$

$$\alpha = \gamma = \frac{1}{1+\rho_\infty}, \quad \beta_0 = \frac{10 - 5\rho_\infty + \rho_\infty^2}{6\,(1+\rho_\infty)}, \quad \beta_1 = \frac{-4 + 11\rho_\infty - \rho_\infty^2}{6\,(1+\rho_\infty)},$$

$$\beta_2 \; = \; \frac{-(1-\rho_\infty)^2}{6\,(1+\rho_\infty)}.$$

Box 4: Summary of method GA-23.

Linear combinations of higher order terms can also be investigated. Consider

$$\delta_4\, \dot{u}_{n+\beta}^{(4)} + (1-\delta_4)\Big(\delta_3\, \dot{u}_{n+\beta}^{(3)} + (1-\delta_3)\, \dot{u}_{n+\beta}^{(2)}\Big) - \lambda\, u_{n+\alpha} = 0, \tag{2.16}$$

which represents a linear combination of the GA-23 and GA-4 schemes. The Jury Table is again employed to determine the critical value of δ_4. The resulting expression is obtained as

$$\delta_4 = \frac{(1-\rho_\infty)^2}{5(1+\rho_\infty^2)}. \tag{2.17}$$

For $\rho_\infty = 1$, one obtains $\delta_4 = \delta_3 = 0$, and the scheme reduces to the trapezoidal rule. For $\rho_\infty = 0$, the weighting factors for GA-2, GA-3, and GA-4 are $\frac{2}{5}$, $\frac{2}{5}$, and $\frac{1}{5}$, respectively. Thus, while GA-4 contributes to the overall accuracy of

the method, its influence is less significant compared to GA-3. The scheme based on Equation (2.16) is referred to as GA-234. The full set of equations describing GA-234 is summarised in Box 5.

The investigation of unconditionally stable linear combinations of GA-p schemes with $p > 4$ is omitted, as such schemes, if they exist, are expected to offer little benefit due to the small weighting of higher-order terms.

$$\dot{u}_{n+\beta} \; - \; f(u_{n+\alpha},\, t_{n+\alpha}) \; = \; 0$$

$$u_{n+\alpha} \; = \; \alpha\, u_{n+1} \; + \; (1-\alpha)\, u_n$$

$$\dot{u}_{n+\beta} \; = \; \beta_0\, \dot{u}_{n+1} \; + \; \beta_1\, \dot{u}_n \; + \; \beta_2\, \ddot{u}_n\, \Delta t \; + \; \beta_3\, \dddot{u}_n\, \Delta t^2$$

$$u_{n+1}^{(i)'} \; = \; u_n^{(i)'} \; + \; \left(\gamma\, u_{n+1}^{(i+1)'} \; + \; (1-\gamma)\; u_n^{(i+1)'}\right) \Delta t \quad \text{for} \;\; i = 0,\, 1{,}2$$

$$\alpha = \gamma = \frac{1}{1+\rho_\infty}, \qquad \beta_0 = \frac{35 - 21\rho_\infty + 7\rho_\infty^2 - \rho_\infty^3}{20\,(1+\rho_\infty)},$$

$$\beta_1 = \frac{-15 + 41\rho_\infty - 7\rho_\infty^2 + \rho_\infty^3}{20\,(1+\rho_\infty)}, \qquad \beta_2 = \frac{(\rho_\infty - 5)(\rho_\infty - 1)^2}{20\,(1+\rho_\infty)},$$

$$\beta_3 = \frac{(\rho_\infty - 1)^3}{20\,(1+\rho_\infty)^2}.$$

Box 5: Summary of method GA-234.

2.3. Analysis of the Methods GA-23 and GA-234

- **Stability:** As described in Section 2.2, the schemes GA-23 and GA-234 have been derived based on the Jury table and are provably unconditionally stable. The stability regions are shown in Figure 2.2, as ρ_∞ increases from zero to one. A scheme is considered unconditionally stable if its stability region (gray area) completely encompasses the left half of the complex plane for all values of ρ_∞.

In anticipation of Section 2.4, it is noted that for $\rho_\infty = 0$, the schemes GA-p coincide with the BDF-p methods, and therefore render the well-known stability regions shown in the first row of the figure for GA-2, GA-3, and GA-4. The eigenvalues of the amplification matrices are shown in the complex plane in Figure 2.3. These figures illustrate the evolution of the methods as higher order terms are included or as ρ_∞ changes.

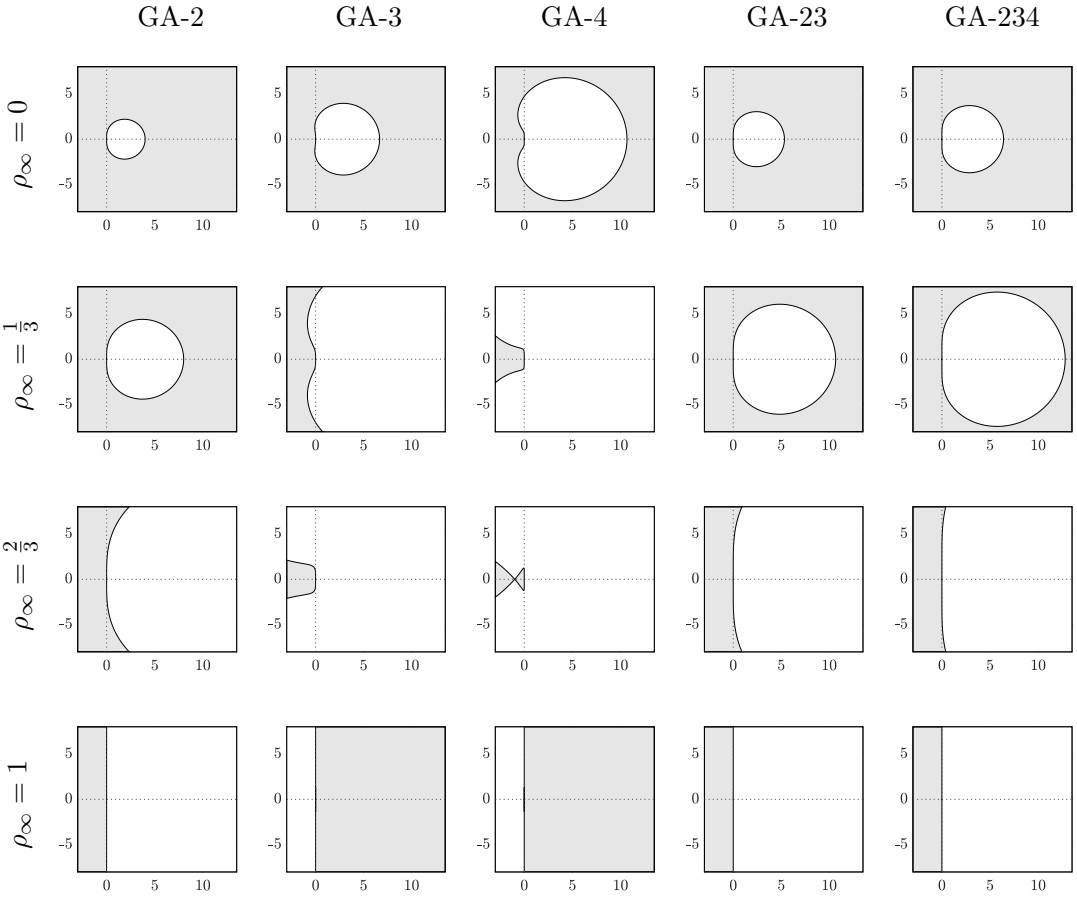

Figure 2.2.: Stability regions (grey), uniform scaling, $\mathrm{Im}(\lambda\Delta t)$ displayed over $\mathrm{Re}(\lambda\Delta t)$.

- **High Frequency Damping:** Figure 2.4 shows the spectral radius as a function of the normalised time step for different values of ρ_∞. Compared to the original generalised-α method (GA-2), the proposed schemes GA-23 and GA-234 delay the onset of noticeable numerical damping to larger time steps, around $\Delta t/T \approx 0.1$. This reduces artificial

dissipation and improves the preservation of dynamic response accuracy. The transition from GA-2 to GA-234 is nearly as significant as the shift from the generalised midpoint rule (GM) to the generalised-α method (GA-2). Thus, GA-23 and GA-234 exhibit significantly less numerical damping than GA-2 in the regime of large time steps while still accurately resolving temporal features of the solution.

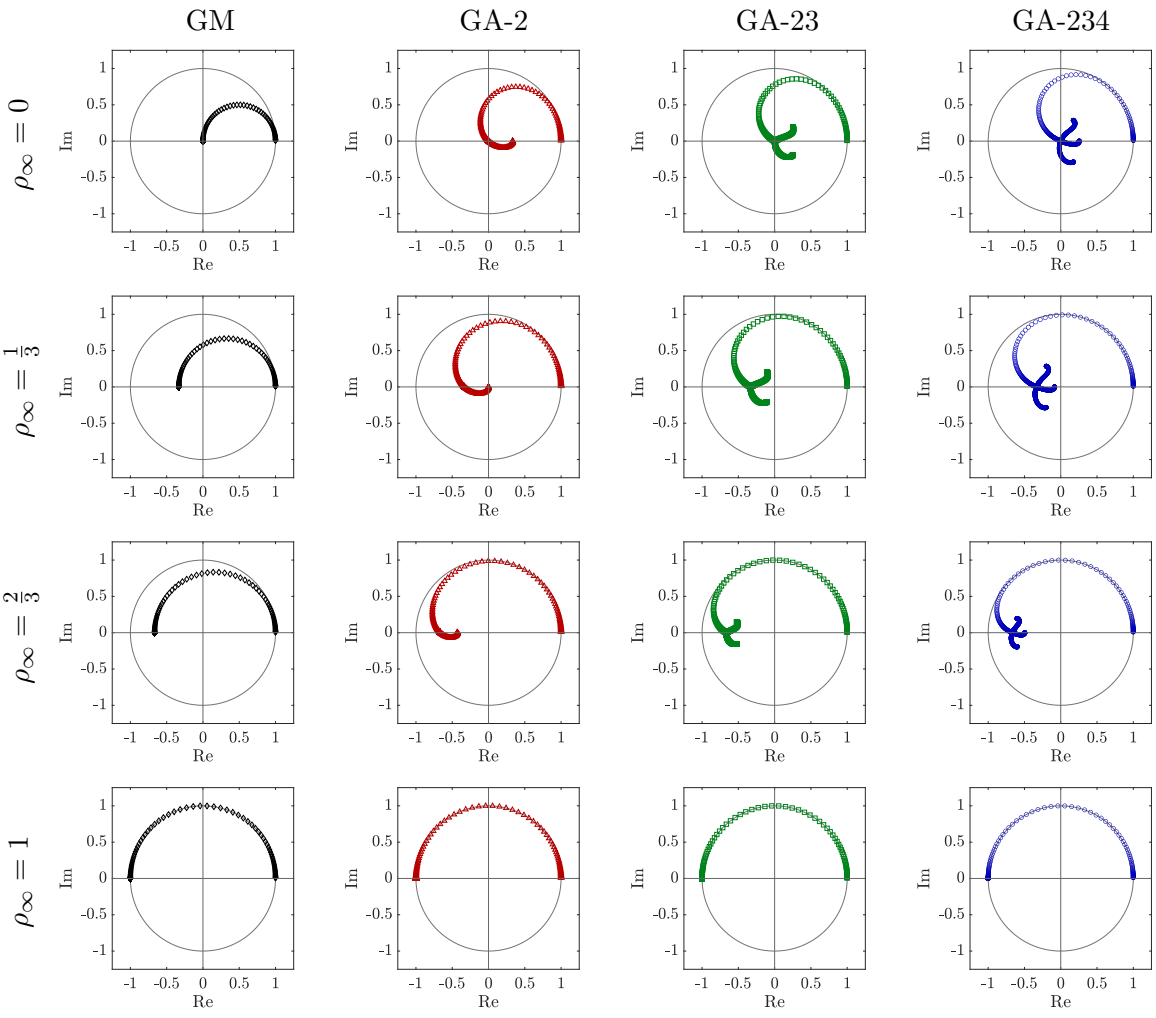

Figure 2.3.: Eigenvalues of the amplification matrices for $\xi = 0$, displayed in the complex plane for a range of time step sizes Δt.

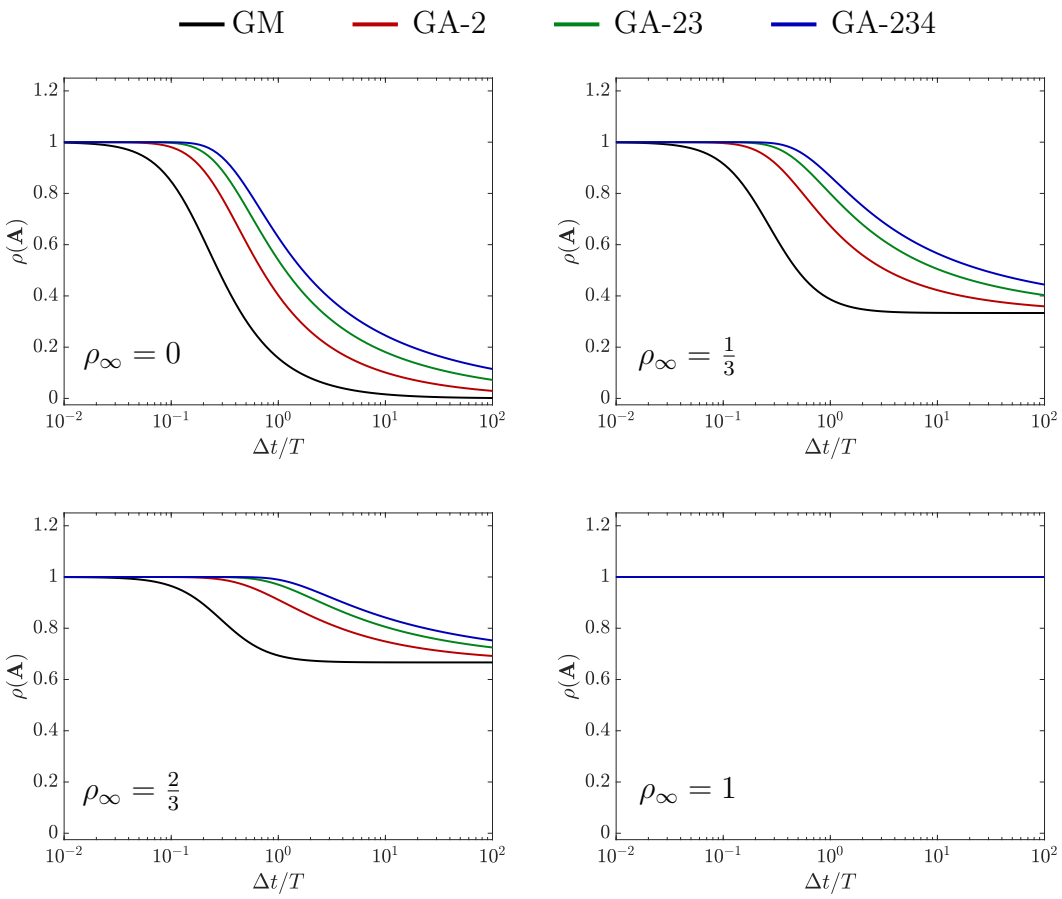

Figure 2.4.: Spectral radii of GM, GA-2, GA-23, and GA-234 for $\omega = 1$ and $\xi = 0$.

- **Accuracy:** To evaluate the accuracy of GA-23 and GA-234 in terms of dispersion and damping, the numerical counterparts ω^h and ξ^h, of, respectively, ω and ξ, are considered and expressed as

$$\omega^h = \frac{1}{\Delta t}\arg(\zeta_{\max}) \quad \text{and} \quad \xi^h = -\frac{1}{\Delta t}\ln(|\zeta_{\max}|), \tag{2.18}$$

  where $\zeta_{\max}$ is the maximum eigenvalue of the amplification matrix. Figure 2.5 illustrate the evolution of ω^h and ξ^h with respect to the time step size Δt. It is observed that GA-23 exhibits smaller approximation errors compared to GA-2; however, it is less accurate than GA-234. Moreover, GA-234 shows noticeably improved damping performance compared to GA-2 and the trapezoidal rule (TR).

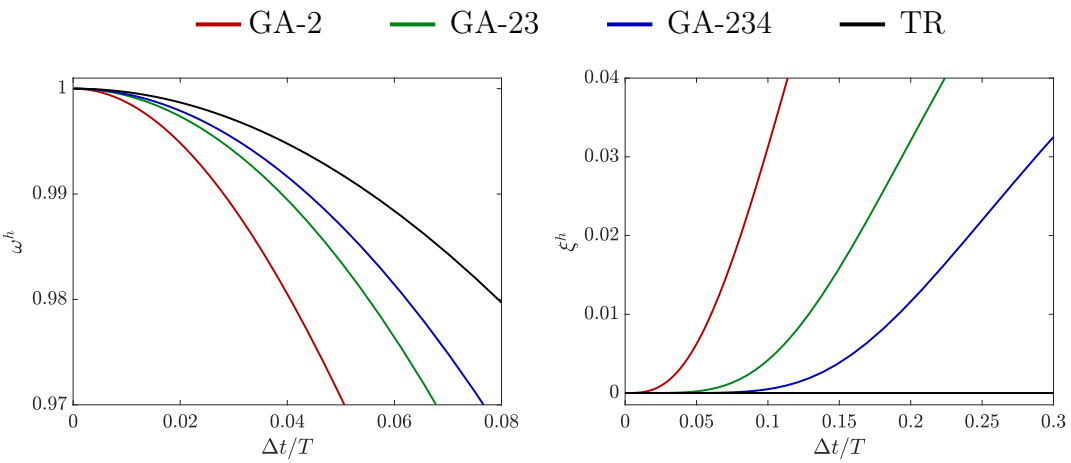

Figure 2.5.: Frequency ω^h and damping coefficient ξ^h of GA-2, GA-23, GA-234, and TR for $\rho_\infty = 0$, $\omega = 1$, and $\xi = 0$.

- **Computational cost:** In comparison to the generalised-α method GA-2, the schemes GA-23 and GA-234 require the allocation of one or two additional history data arrays, respectively, to store $\ddot{u}_n$ and $\dddot{u}$. However, these additional memory requirements are minimal, especially when compared to the storage needed for the global system solver. The additional computational time is also negligible, as the additional operations are limited to updating the global arrays $\ddot{u}_n$ and $\dddot{u}$.

2.4. Backward Difference Formulae

For $\rho_\infty = 0$, the time integration schemes GA-p described by Equations (2.5) to (2.8) are equivalent to the well-known backward difference formulae BDF-p, described for instance in [16, 103]. To show this, Equation (2.8) is reformulated as

$$u_{n+1}^{(i+1)'} = \frac{1}{\Delta t\,\gamma}\left(u_{n+1}^{(i)'} - u_n^{(i)'}\right) - \frac{(1-\gamma)}{\gamma}\,u_n^{(i+1)'} \tag{2.19}$$

where $\gamma = 1$ for $\rho_\infty = 0$.

This formula can be applied recursively to each term on the right-hand side, thereby reducing the order of the derivatives and involving terms from earlier time instants. Eventually, all derivatives on the right side of Equation (2.7) can be reformulated using the historical values of the primary variable u, thus resulting in the backward difference formula.

The BDF-p schemes are given by

$$\dot{u}_{n+1} \; - \; \lambda u_{n+1} \; = \; 0 \tag{2.20}$$

$$\dot{u}_{n+1} \; = \; \frac{1}{\Delta t} \sum_{i=0}^{p} \beta_i u_{n+1-i}, \tag{2.21}$$

the coefficients β_i are given in Table 2.1. This procedure can also be applied to the methods GA-23 and GA-234, resulting in linear combinations of BDF-2, BDF-3, and BDF-4. The formulated methods are denoted as BDF-23 and BDF-234 and are summarised in Boxes 6 and 7, respectively. As opposed to GA-23 and GA-234, the schemes BDF-23 and BDF-234 do not allow for varying time step sizes or for user-controlled high frequency damping. However, their implementation in any existing computer code based on BDF-1 (backward Euler) or BDF-2 is trivial and renders an immediate benefit in terms of improved accuracy.

Table 2.1.: Coefficients β_i for backward difference formulae BDF-p.

p	β_0	β_1	β_2	β_3	β_4
1	1	-1			
2	$3/2$	-2	$1/2$		
3	$11/6$	-3	$3/2$	$-1/3$	
4	$25/12$	-4	3	$-4/3$	$1/4$

The numerical properties of BDF-23 and BDF-234 are identical to those of GA-23 and GA-234 for $\rho_\infty = 0$ and are thus represented in Figures 2.3 to 2.5 by their GA counterparts. For convenience, the stability regions of the BDF schemes are presented together in Figure 2.6. For linear problems with correct initial conditions, BDF-23 and BDF-234 yield identical numerical results to

those of GA-23 and GA-234 for $\rho_\infty = 0$. Therefore, to avoid redundancy BDF-23 and BDF-234 are represented by GA-23 and GA-234 with $\rho_\infty = 0$ in sections 2.5 to 2.7.

$$\dot{u}_{n+1} - f(u_{n+1}, t_{n+1}) = 0$$

$$\dot{u}_{n+1} = \frac{10\,u_{n+1} - 15\,u_n + 6\,u_{n-1} - u_{n-2}}{6\,\Delta t}$$

Box 6: Summary of method BDF-23 (equivalent to Park's method).

$$\dot{u}_{n+1} - f(u_{n+1}, t_{n+1}) = 0$$

$$\dot{u}_{n+1} = \frac{35\,u_{n+1} - 56\,u_n + 28\,u_{n-1} - 8\,u_{n-2} + u_{n-3}}{20\,\Delta t}$$

Box 7: Summary of method BDF-234.

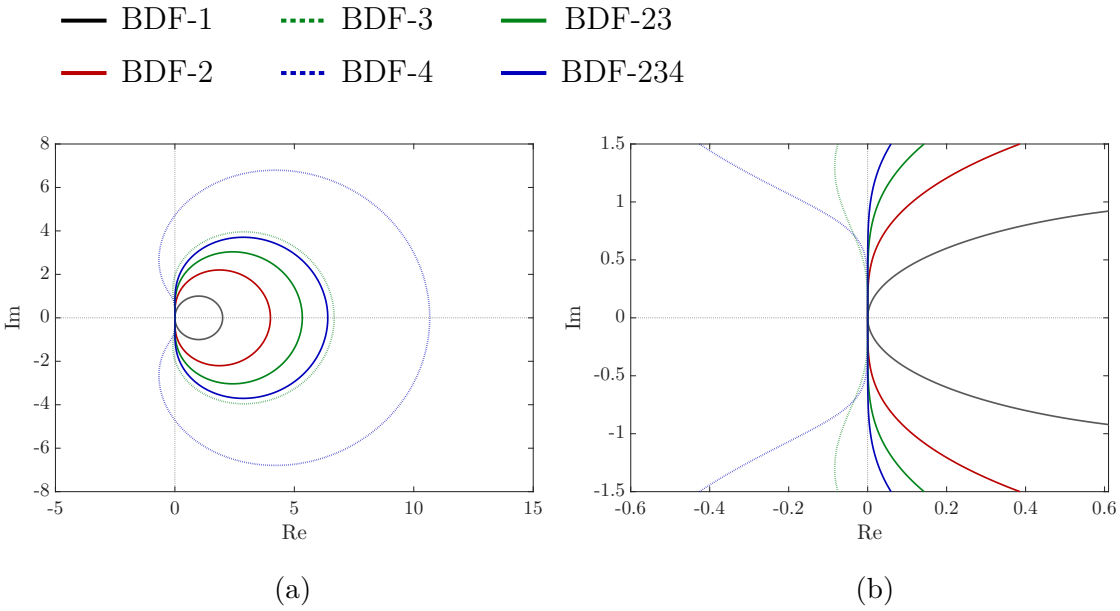

(a) (b)

Figure 2.6.: Stability regions for BDF methods; overview of stability regions (a), close-up view near the origin (b).

Remark 2.4.5: The BDF-23 method (GA-23 for $\rho_\infty = 0$) is equivalent to both Park's method and the BDF2OPT(4) scheme, proposed in [66, 100] and [113], respectively. Hence, GA-23 can be seen as an interpolation between Park's method and the trapezoidal rule, as illustrated in Figure 2.7. Park's method is regarded as advantageous for stiff problems in structural dynamics, as discussed in [100].

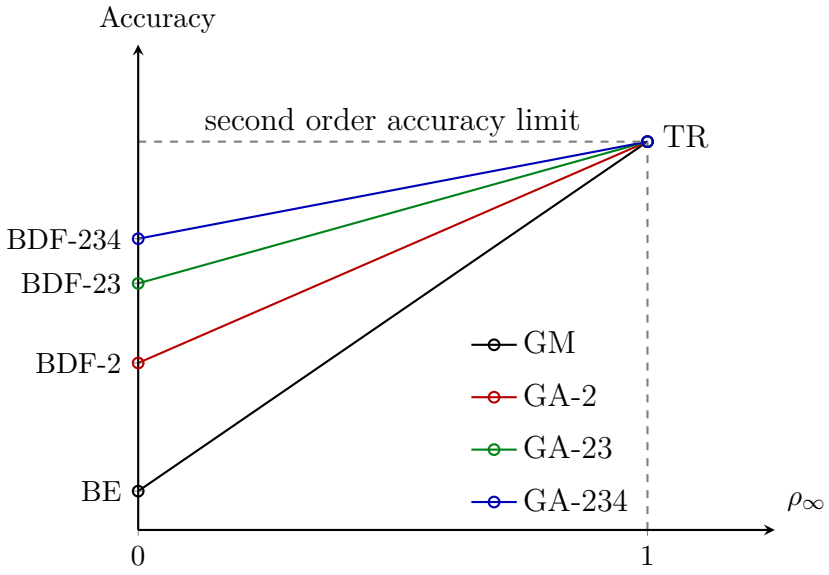

Figure 2.7.: Overview of unconditionally stable implicit time integration schemes. The methods GM, GA-2, GA-23, and GA-234 are viewed as interpolations between various BDF methods and the trapezoidal rule.

Remark 2.4.6: The BDF-234 method achieves higher accuracy than BDF-23 while maintaining unconditional stability. The BDF2OPT(5) scheme, introduced in [113], is defined as

$$\text{BDF2OPT(5)} = \left(1 - \frac{1}{\sqrt{2}}\right) \text{BDF4} + \left(2\sqrt{2} - \frac{5}{2}\right) \text{BDF3} + \left(\frac{5\sqrt{2} - 6}{2\sqrt{2}}\right) \text{BDF2}.$$

The stability region of BDF2OPT(5) is non-convex and intersects the imaginary axis at three distinct points, as shown in Figure 2.8. As reported in [113], this behaviour may compromise the long-term stability of numerical

simulations, particularly for stiff or oscillatory problems. By contrast, the BDF-234 method exhibits a more desirable stability behaviour, with its stability region intersecting the imaginary axis only at the origin, as illustrated in Figure 2.6. This property makes BDF-234 potentially more dependable for long-term integrations.

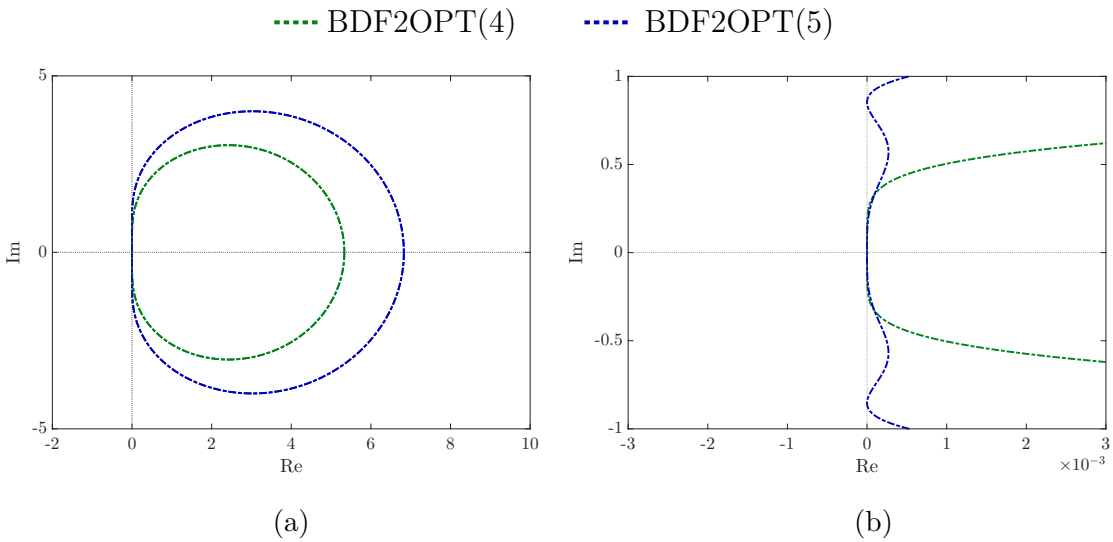

Figure 2.8.: Stability regions for the BDF2OPT schemes; overview of stability regions (a), close-up view near the origin (b).

2.5. Example 1: Linear Model Problem

The standard scalar linear initial-value problem, as defined by Equation (2.2), is used to evaluate and compare the performance of the numerical methods presented in Sections 2.2 to 2.4. The exact analytical solution is given in Equation (2.3). For a comprehensive assessment, two cases are considered; one with $\xi = 0$, representing the undamped case, and the other with $\xi = 0.1$, representing the damped case. The frequency parameter is set to $\omega = 1$ rad/s, giving an oscillation period of $T = 2\pi$ s. The initial condition is specified as $u(0) = \omega + i\xi$.

The numerical results obtained using the GA-2, GA-23, and GA-234 schemes for various time-step sizes Δt and values of ρ_∞ are presented in Figures 2.9 and 2.10 for $\xi = 0$ and $\xi = 0.1$, respectively. The figures illustrate the real part of the numerical solutions. The imaginary part, although phase-shifted, exhibits qualitatively and quantitatively similar behaviour to the real part and is therefore omitted for brevity.

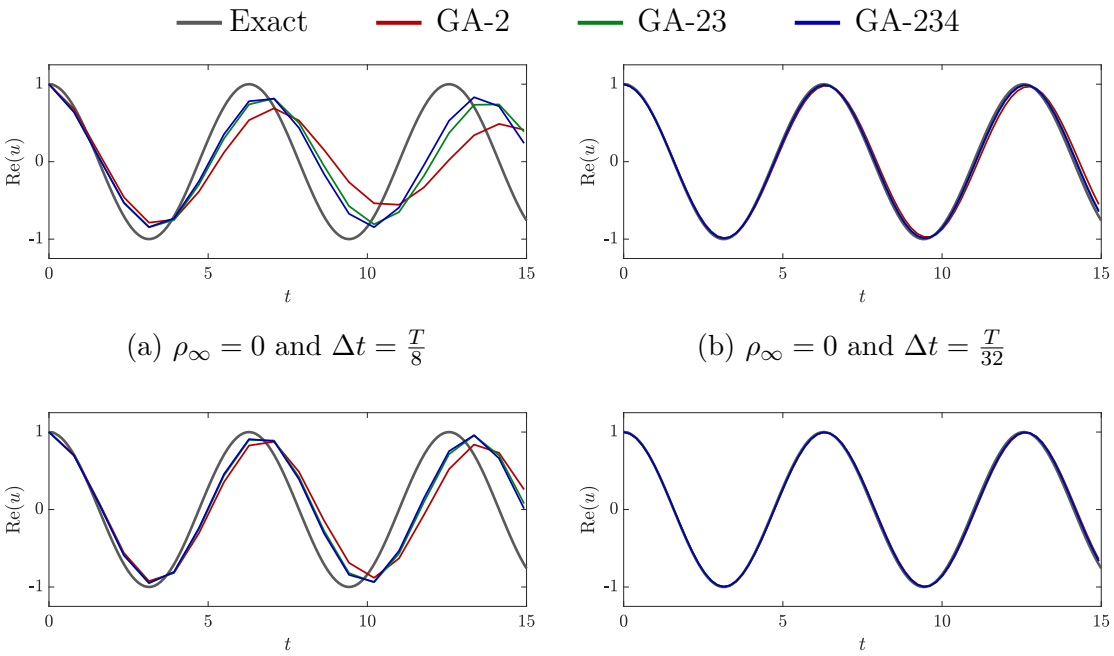

(a) $\rho_\infty = 0$ and $\Delta t = \frac{T}{8}$

(b) $\rho_\infty = 0$ and $\Delta t = \frac{T}{32}$

(c) $\rho_\infty = \frac{1}{3}$ and $\Delta t = \frac{T}{8}$

(d) $\rho_\infty = \frac{1}{3}$ and $\Delta t = \frac{T}{32}$

Figure 2.9.: Linear model problem; system response obtained for $\omega = 1\ \mathrm{rad\,s^{-1}}$ and $\xi = 0.0$.

The following observations are made from Figures 2.9 and 2.10:

1. Subfigures (c) and (d) show that all three numerical solutions align more closely with the exact solution than those in subfigures (a) and (b), respectively. This indicates that the deviation is smaller for $\rho_\infty = \frac{1}{3}$ than for $\rho_\infty = 0$, which is expected, since all the considered schemes reduce to the trapezoidal rule when $\rho_\infty = 1$.

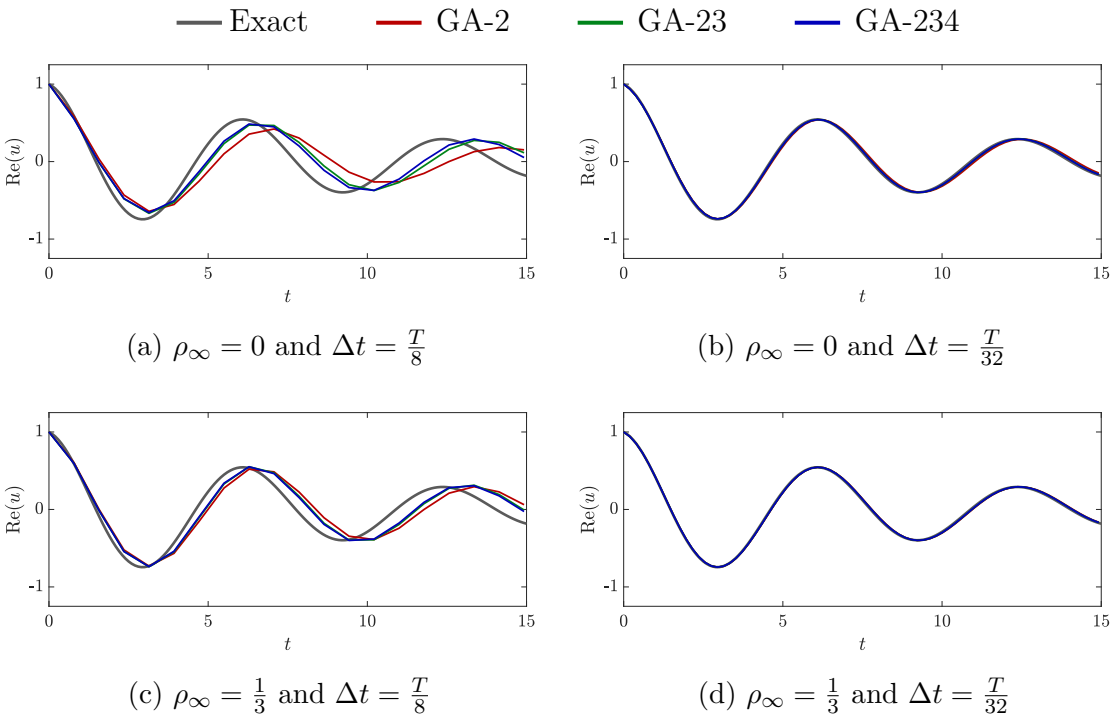

(a) $\rho_\infty = 0$ and $\Delta t = \frac{T}{8}$

(b) $\rho_\infty = 0$ and $\Delta t = \frac{T}{32}$

(c) $\rho_\infty = \frac{1}{3}$ and $\Delta t = \frac{T}{8}$

(d) $\rho_\infty = \frac{1}{3}$ and $\Delta t = \frac{T}{32}$

Figure 2.10.: Linear model problem; system response obtained for $\omega = 1\ \mathrm{rad\,s^{-1}}$ and $\xi = 0.1$.

2. Both GA-23 and GA-234 exhibit less numerical damping and smaller frequency errors than GA-2. This is evident in all subfigures, where GA-2 shows faster amplitude decay than the other methods.

3. For small time steps, $\Delta t = T/32$, all methods improve and converge towards the exact solution, with the differences between GA-2, GA-23, and GA-234 becoming minimal.

4. For large time steps, $\Delta t = T/8$, GA-23 and GA-234 demonstrate higher accuracy, maintaining better agreement with the exact solution than the generalised-α method, GA-2. Furthermore, GA-234 performs slightly better than GA-23.

Figure 2.11 shows the convergence of the numerical solution as Δt decreases for GM, GA-2, GA-23, and GA-234 for different values of ρ_∞. The error is computed by comparing the exact solution from Equation (2.3), denoted by $\tilde{u}$,

to the numerical solution obtained from each method, i.e.,

$$\epsilon = \sqrt{\frac{1}{N}\sum_{n=1}^{N} |u_n - \tilde{u}_n|^2} \tag{2.22}$$

where N is the number of time steps used in the respective computation to reach $t_N = 35$.

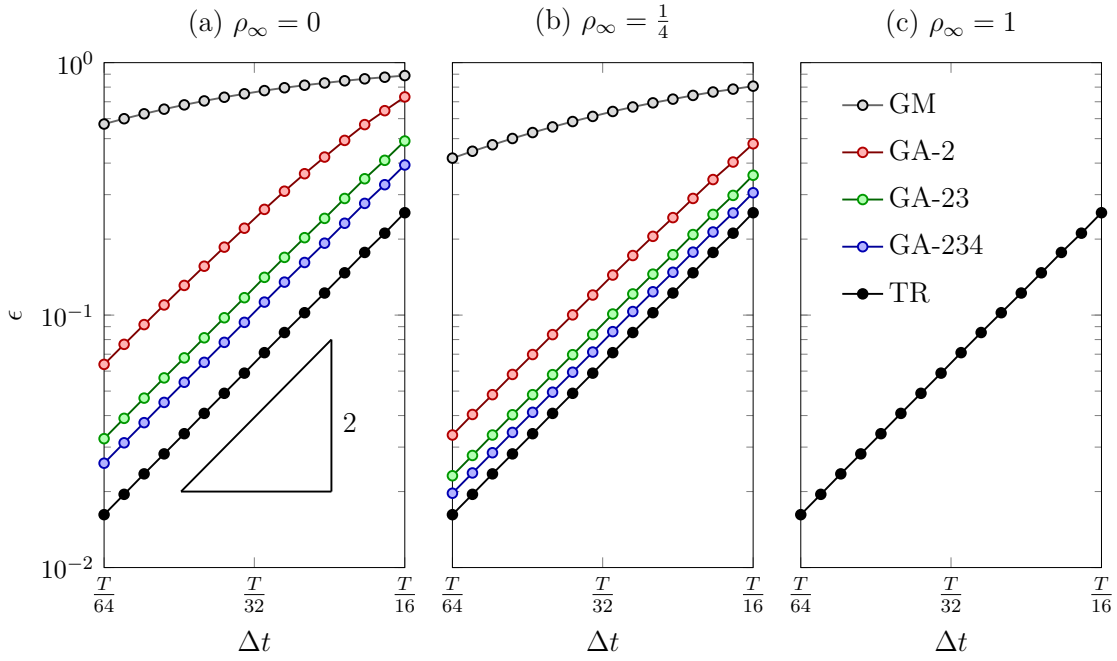

Figure 2.11.: Linear model problem; convergence rates.

The following observations are made from Figure 2.11:

1. The differences between the subfigures for GA-2, GA-23, and GA-234 reduce as ρ_∞ increases. For $\rho_\infty = 1$, all methods coincide with the trapezoidal rule (TR).

2. GA-23 and GA-234 consistently produce smaller approximation errors than GA-2 across all cases. Notably, the accuracy level of GA-234 is closer to that of the trapezoidal rule (TR) than to GA-2.

3. For $\rho_\infty = 0$, the improvement in accuracy from GA-2 to GA-234 in the regime of time steps around $\Delta t = T/32$ is similar to that from the first order accurate method GM to the second order accurate scheme GA-2. This is also reflected in Figure 2.9, where, for $\rho_\infty = 0$, GA-234 renders significantly more accurate results than GA-2.

Importantly, Observation 3 indicates that within the time step range of $T/50 < \Delta t < T/25$, which is crucial for industrial applications involving implicit time integration, GA-234 offers substantial performance gains over the standard generalised-α method GA-2. Additionally, since BDF-2 is equivalent to GA-2, and BDF-234 to GA-234 for $\rho_\infty = 0$, this also demonstrates the advantages of BDF-234 over the standard method, BDF-2.

2.6. Example 2: Flow Around Cylinder

The following benchmark example examines the flow of an incompressible fluid around a stationary circular cylinder. The flow is governed by the incompressible Navier–Stokes equations. Figure 2.12 shows the geometry and boundary conditions, while Figure 2.13 illustrates the finite element mesh employed, consisting of 12,258 elements.

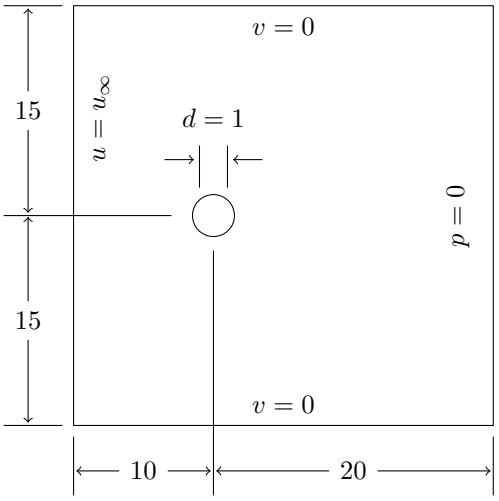

Figure 2.12.: Flow around cylinder; geometry and boundary conditions.

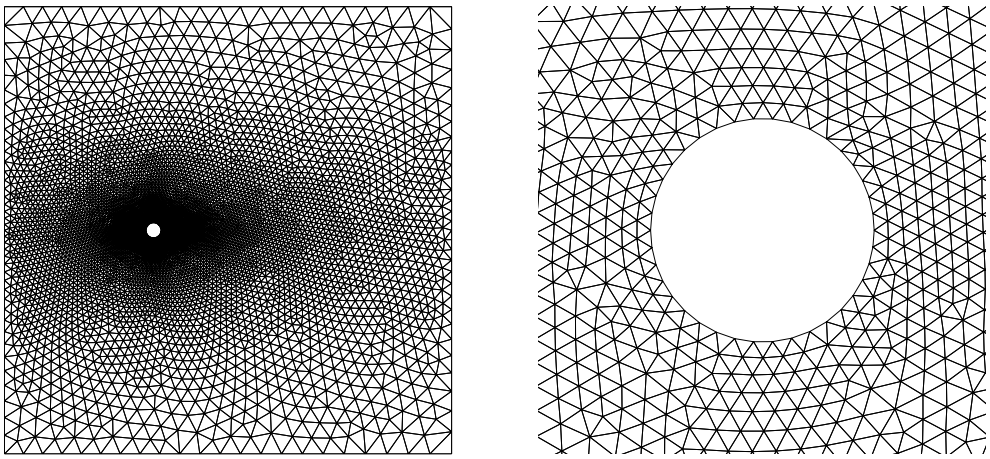

(a) (b)

Figure 2.13.: Flow around cylinder; finite element mesh (a), mesh refinement around the cylinder (b).

The spatial discretisation is based on P2/P1 Taylor–Hood velocity–pressure elements (quadratic interpolation for velocity and linear interpolation for pressure); see, for example, [124]. The convective velocity is approximated with second order accuracy, as described in [76], which results in a linear global system of equations that is solved at each time step for the velocity and pressure degrees of freedom. The total number of degrees of freedom is 55,138.

The vertical velocity component v is set to zero at the upper and lower boundaries, while the horizontal velocity component u remains unconstrained. At the outlet boundary, the pressure is set to zero, and at the inlet boundary, the horizontal velocity is prescribed uniformly as $u_\infty = 1.0$ m/s. The cylinder diameter is $d = 1.0$ m, while the fluid density and dynamic viscosity are given by $\rho = 1.0$ kg/m^3 and $\mu = 0.01$ Pa s, respectively. Hence, the Reynolds number is defined as

$$Re = \frac{\rho\, u_\infty\, d}{\mu} = 100 \tag{2.23}$$

The Strouhal number is defined as $St = \frac{fd}{u_0}$, where f is the frequency of vortex shedding, i.e., the frequency of oscillation of the lift force on the cylinder. The flow is simulated using the schemes GM, GA-2, GA-23, and GA-234.

Figure 2.14 illustrates the evolution of the drag (C_D) and lift (C_L) coefficients over time. Figure 2.15 shows the convergence of the Strouhal number as the time step size Δt is reduced.

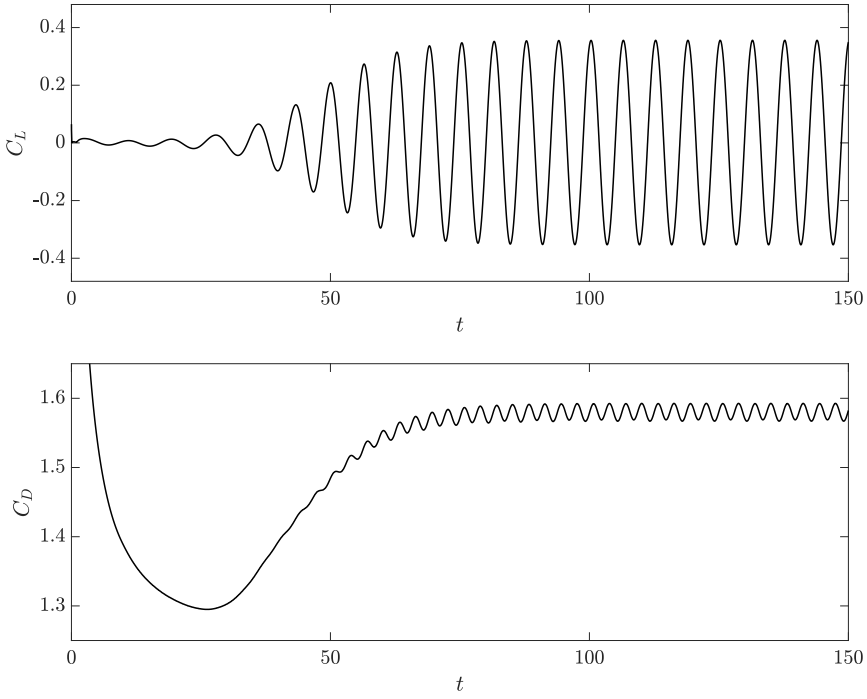

Figure 2.14.: Flow around cylinder; Typical evolution of the lift and drag coefficients.

Clearly, as Δt is reduced, all methods converge to the Strouhal number $St = 0.1728$. This value depends on several factors, including the Reynolds number, the size of the computational domain, and the mesh resolution employed in the simulation. The obtained value agrees well with results reported in the literature, such as those in [36, 76] and references therein. The convergence pattern observed here is consistent with that noted for the linear model problem in Section 2.6. Among the methods tested, GA-23 and GA-234 demonstrate superior performance compared to GA-2, particularly for smaller values of ρ_∞ and within the range of physically relevant time step sizes. It is also worth noting that the TR scheme fails to produce results in the small time step regime due to insufficient numerical damping, which results in instability of the solution.

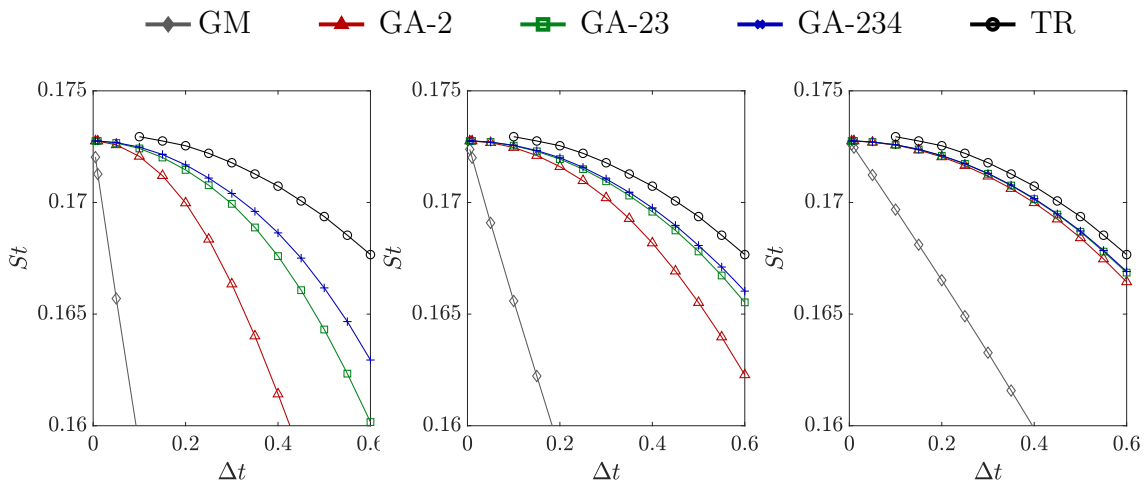

(a) $\rho_\infty = 0$ (b) $\rho_\infty = \frac{1}{3}$ (c) $\rho_\infty = \frac{2}{3}$

Figure 2.15.: Flow around cylinder; St convergence.

2.7. Example 3: Pulsatile Flow Through a Cavity

The following example presents a two-dimensional cavity with inflow and outflow channels, as shown in Figure 2.16. The fluid flow is governed by the incompressible Navier–Stokes equations. The fluid density and dynamic viscosity are given by $\rho = 1.0$ kg/m^3 and $\mu = 0.01$ Pa s, respectively. A no-slip boundary condition is applied to all channel and cavity walls.

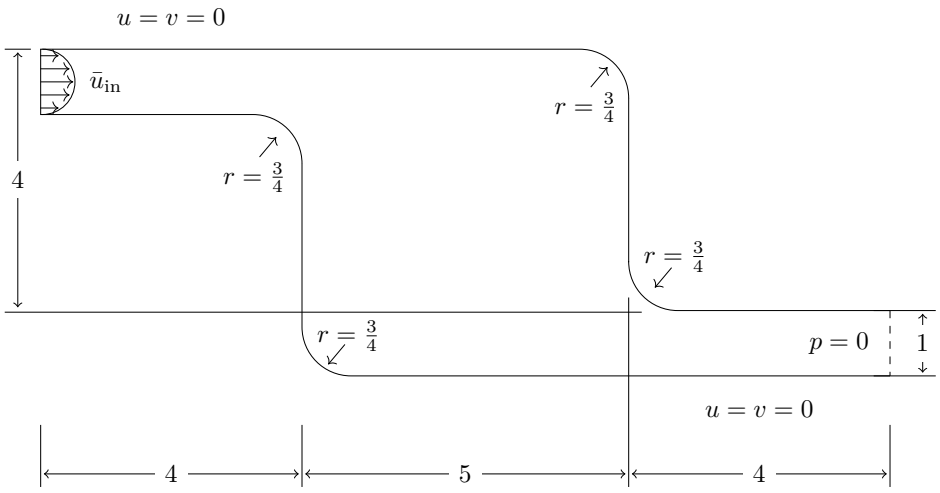

Figure 2.16.: Flow through a cavity; geometry and boundary conditions.

The fluid domain is discretised using 7,890 P2/P1 Taylor–Hood velocity–pressure elements, yielding a total of 35,010 degrees of freedom. The corresponding finite element mesh is depicted in Figure 2.17.

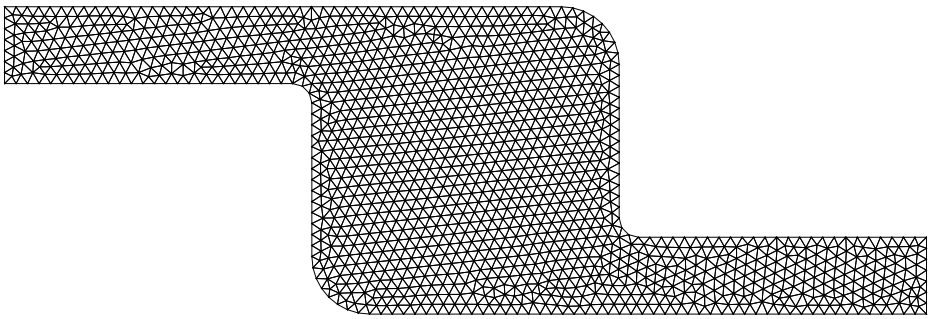

Figure 2.17.: Flow through a cavity; finite element mesh.

The inflow velocity is prescribed with a quadratic profile, where the peak velocity $\bar{u}_{\text{in}}$ oscillates between 0 and 8.0 m/s, and is defined as

$$\bar{u}_{\text{in}}(t) = 4\left(1 - \cos\left(\frac{2\pi t}{5}\right)\right). \tag{2.24}$$

The simulation is conducted using the GA-2, GA-23, and GA-234 methods for $\rho_\infty = 0$ with different time-step sizes Δt. For the given finite element mesh and time-step sizes, the simulation can also be performed using the trapezoidal rule (TR). All simulations are terminated at $t = 15$ s.

A mesh-dependent reference solution is obtained using the numerical method GA-234 with a time step of $\Delta t = 0.001$ s. This reference solution is used to approximate the error ϵ, defined as

$$\epsilon = \sqrt{\int ||\mathbf{u} - \tilde{\mathbf{u}}||^2 \, \mathrm{d}a}, \tag{2.25}$$

where $\tilde{\mathbf{u}}$ denotes the velocity field of the reference solution, and $\mathbf{u}$ is the velocity field computed by other numerical methods at $t = 15$ s. Figure 2.18 presents the convergence of the error estimate against this mesh-dependent reference solution. The observed convergence pattern confirms that GA-23 surpasses the accuracy of GA-2, while GA-234 demonstrates greater accuracy than GA-23

and produces errors nearly as small as those achieved by the TR scheme. Figure 2.19 illustrates typical velocity and vorticity distributions, highlighting the vortex formation within the cavity.

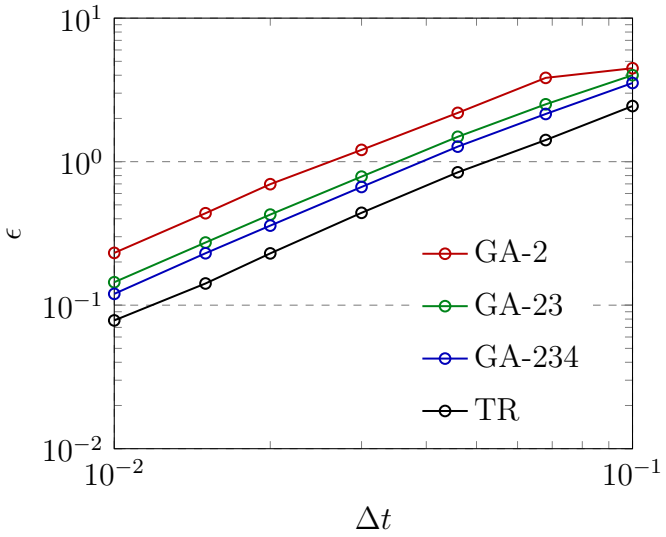

Figure 2.18.: Flow through a cavity; temporal convergence.

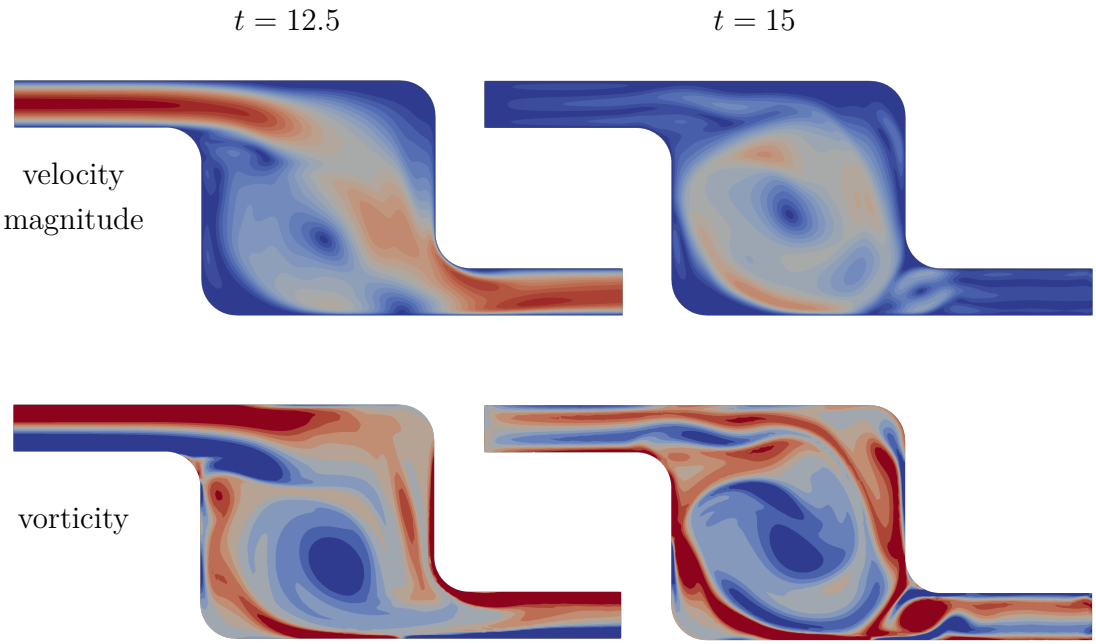

Figure 2.19.: Flow through a cavity; typical velocity magnitude (0 [blue] to 8 [red]) and vorticity (-10 [blue] to +10 [red]) contour plots.

Chapter 3

Time Integration Schemes for Second Order Problems

This chapter builds upon the GA-23 and GA-234 time integration schemes, initially developed in Chapter 2 for first order problems, by extending their application to second order structural dynamics problems. For clarity of the context, it is important to distinguish between the various versions of the generalised-α method. The original version was introduced for second order structural dynamics problems in [27]. Later, a related scheme was developed in [68] specifically for first order problems in time, which was primarily applied in computational fluid dynamics. In subsequent work, [73] highlighted the advantages of using the first order generalised-α scheme from [68] for second order structural dynamic problems. By applying a standard order reduction procedure combined with auxiliary solution variables, this approach successfully adapted the first order method for second order equations. This adaptation resulted in a scheme that differed from the original second order formulation in [27], yet it maintained comparable efficiency and offered enhanced approximation properties.

The GA-23 and GA-234 schemes are extended to second order problems by employing a similar procedure to the one outlined in [73]. The resulting schemes outperform the methods presented in [27] and [73] while retaining the key properties of the original first order formulation schemes presented in Chapter 2, including enhanced accuracy and reduced numerical dispersion.

Notably, they achieve these advantages with minimal additional computational cost, making them a competitive alternative to multi-sub-step or composite methods, which divide a single time step into multiple sub-steps and apply different numerical schemes within each sub-step, thereby requiring additional computations for each time step (see [82, 116, 122]).

3.1. Application to Second Order Problems

The methodology outlined in this section follows the procedure and notation adopted in [73] for applying first order time integration schemes to structural dynamics. The governing equation for linear structural dynamics is expressed in matrix form as

$$\mathbf{M}\,\ddot{\mathbf{d}} \;+\; \mathbf{C}\,\dot{\mathbf{d}} \;+\; \mathbf{K}\,\mathbf{d} \;=\; \mathbf{F}, \tag{3.1}$$

where $\mathbf{M}$, $\mathbf{C}$, and $\mathbf{K}$ denote the mass, damping, and stiffness matrices respectively, and $\mathbf{F}$ is the vector of external forces. The vector $\mathbf{d}$ denotes the displacements, while $\dot{\mathbf{d}}$ and $\ddot{\mathbf{d}}$ represent the velocity and acceleration vectors respectively. The initial conditions are given as $\mathbf{d}(0) = \mathbf{d}_0$ and $\dot{\mathbf{d}}(0) = \dot{\mathbf{d}}_0$. The initial acceleration is calculated from Equation (3.1) as

$$\ddot{\mathbf{d}}_0 = \mathbf{M}^{-1}\left(\mathbf{F}(0) - \mathbf{C}\,\dot{\mathbf{d}}_0 - \mathbf{K}\,\mathbf{d}_0\right). \tag{3.2}$$

The second order Equation (3.1) is converted into a system of first order equations by introducing the velocities $\mathbf{v}$ as auxiliary variables

$$\mathbf{v} = \dot{\mathbf{d}}, \tag{3.3}$$

resulting in

$$\mathbf{M}\,\dot{\mathbf{v}} + \mathbf{C}\,\mathbf{v} + \mathbf{K}\,\mathbf{d} = \mathbf{F}. \tag{3.4}$$

Equations (3.3) and (3.4) represent a first order system in terms of $\mathbf{d}$ and $\mathbf{v}$. Any of the time integration schemes GM, GA-2, GA-23, and GA-234 proposed in Chapter 2 can be applied for temporal discretisation. Each method requires the implicit solution of a single set of variables. The application of the

generalised midpoint rule GM is straightforward, and the resulting equations are summarised in Box 8. Applying GA-2, GA-23, or GA-234 requires storing one, two, or three instances of the velocity vectors $\dot{\mathbf{d}}$ and $\mathbf{v}$, respectively. Deriving the required equations for GA-23 and GA-234 is tedious and lengthy, yet the process is straightforward and follows a procedure analogous to that used for GA-2, which is therefore described in the following. The resulting schemes for GA-2, GA-23, and GA-234 are summarised respectively in Boxes 9, 10, and 11. Note that the scheme in Box 9, is equivalent to the method described in [73]. The schemes presented in Boxes 10 and 11 are newly developed and are the primary focus of this chapter. For nonlinear problems, the stiffness matrix $\mathbf{K}$ has to be evaluated in the configuration defined by the displacements $\mathbf{d}_{n+\alpha}$. Applying GA-2 to Equations (3.3) and (3.4) yields the following

$$\mathbf{v}_{n+\alpha} = \dot{\mathbf{d}}_{n+\beta} \tag{3.5}$$

$$\mathbf{M}\,\dot{\mathbf{v}}_{n+\beta} \;+\; \mathbf{C}\,\mathbf{v}_{n+\alpha} \;+\; \mathbf{K}\,\mathbf{d}_{n+\alpha} \;=\; \mathbf{F}_{n+\alpha}, \tag{3.6}$$

where

$$\mathbf{F}_{n+\alpha} \;=\; \alpha\,\mathbf{F}_{n+1} \;+\; (1 \;-\; \alpha)\,\mathbf{F}_n, \tag{3.7}$$

$$\mathbf{d}_{n+\alpha} \;=\; \alpha\,\mathbf{d}_{n+1} \;+\; (1 \;-\; \alpha)\,\mathbf{d}_n, \tag{3.8}$$

$$\dot{\mathbf{d}}_{n+\beta} \;=\; \beta_0\,\dot{\mathbf{d}}_{n+1} \;+\; \beta_1\,\dot{\mathbf{d}}_n, \tag{3.9}$$

$$\mathbf{d}_{n+1} \;=\; \mathbf{d}_n + \Delta t\,\left(\gamma\,\dot{\mathbf{d}}_{n+1} \;+\; (1 \;-\; \gamma)\,\dot{\mathbf{d}}_n\right), \tag{3.10}$$

$$\mathbf{v}_{n+\alpha} \;=\; \alpha\,\mathbf{v}_{n+1} \;+\; (1 \;-\; \alpha)\,\mathbf{v}_n, \tag{3.11}$$

$$\dot{\mathbf{v}}_{n+\beta} \;=\; \beta_0\,\dot{\mathbf{v}}_{n+1} \;+\; \beta_1\,\dot{\mathbf{v}}_n, \tag{3.12}$$

$$\mathbf{v}_{n+1} \;=\; \mathbf{v}_n \;+\; \Delta t\,(\gamma\,\dot{\mathbf{v}}_{n+1} \;+\; (1 \;-\; \gamma)\,\dot{\mathbf{v}}_n)\,. \tag{3.13}$$

For convenience, Equations (3.10) and (3.13) are rewritten as,

$$\dot{\mathbf{d}}_{n+1} = \frac{1}{\gamma\,\Delta t}\,(\mathbf{d}_{n+1} - \mathbf{d}_n) - \frac{1 \;-\; \gamma}{\gamma}\,\dot{\mathbf{d}}_n \tag{3.14}$$

$$\dot{\mathbf{v}}_{n+1} = \frac{1}{\gamma\,\Delta t}\,(\mathbf{v}_{n+1} - \mathbf{v}_n) - \frac{1 \;-\; \gamma}{\gamma}\,\dot{\mathbf{v}}_n. \tag{3.15}$$

By equating $\dot{\mathbf{d}}_{n+\beta}$ and $\mathbf{v}_{n+\alpha}$ from Equations (3.9) and (3.11), $\mathbf{v}_{n+1}$ can be reformulated as

$$\mathbf{v}_{n+1} = \frac{\beta_0}{\alpha}\,\dot{\mathbf{d}}_{n+1} + \frac{\beta_1}{\alpha}\,\dot{\mathbf{d}}_n - \frac{1-\alpha}{\alpha}\,\mathbf{v}_n. \tag{3.16}$$

Next, by substituting Equation (3.14) into Equation (3.16), $\mathbf{v}_{n+1}$ is obtained as

$$\mathbf{v}_{n+1} = \frac{\beta_0}{\alpha\,\gamma\,\Delta t}\,(\mathbf{d}_{n+1} - \mathbf{d}_n) + \frac{\gamma\,(\beta_0 \;+\; \beta_1) \;-\; \beta_0}{\alpha\,\gamma}\,\dot{\mathbf{d}}_n - \frac{1-\alpha}{\alpha}\,\mathbf{v}_n. \tag{3.17}$$

Subsequently, substituting Equation (3.17) into Equation (3.15), $\dot{\mathbf{v}}_{n+1}$ becomes

$$\dot{\mathbf{v}}_{n+1} = \frac{\beta_0}{\alpha\,\gamma^2\,\Delta t^2}\,(\mathbf{d}_{n+1} - \mathbf{d}_n) + \frac{\gamma\,(\beta_0 \;+\; \beta_1) \;-\; \beta_0}{\alpha\,\gamma^2\,\Delta t}\,\dot{\mathbf{d}}_n - \frac{1}{\alpha\,\gamma\,\Delta t}\,\mathbf{v}_n - \frac{1 \;-\; \gamma}{\gamma}\,\dot{\mathbf{v}}_n. \tag{3.18}$$

Finally, Equation (3.1) can be solved for $\mathbf{d}_{n+1}$ from

$$\hat{\mathbf{K}}\,\mathbf{d}_{n+1} = \hat{\mathbf{F}}, \tag{3.19}$$

where $\hat{\mathbf{K}}$ is the effective stiffness matrix

$$\hat{\mathbf{K}} = \frac{\beta_0^2}{\alpha\,\gamma^2\,\Delta t^2}\,\mathbf{M} \;+\; \frac{\beta_0}{\gamma\,\Delta t}\,\mathbf{C} \;+\; \alpha\,\mathbf{K}, \tag{3.20}$$

and $\hat{\mathbf{F}}$ is the effective force vector

$$\begin{aligned}\hat{\mathbf{F}} = {}& \mathbf{F}_{n+\alpha} \;-\; \beta_1\,\mathbf{M}\,\dot{\mathbf{v}}_n \;-\; (1-\alpha)\,\mathbf{C}\,\mathbf{v}_n \;-\; (1-\alpha)\,\mathbf{K}\,\mathbf{d}_n \\ & + \alpha\,\mathbf{C}\left[\frac{\beta_0}{\alpha\,\gamma\,\Delta t}\,\mathbf{d}_n \;-\; \frac{\gamma\,(\beta_0 \;+\; \beta_1) \;-\; \beta_0}{\alpha\,\gamma}\,\dot{\mathbf{d}}_n \;+\; \frac{1-\alpha}{\alpha}\,\mathbf{v}_n\right] \\ & + \beta_0\,\mathbf{M}\left[\frac{\beta_0}{\alpha\,\gamma^2\,\Delta t^2}\,\mathbf{d}_n \;-\; \frac{\gamma\,(\beta_0 \;+\; \beta_1) \;-\; \beta_0}{\alpha\,\gamma^2\,\Delta t}\,\dot{\mathbf{d}}_n \;+\; \frac{1}{\alpha\,\gamma\,\Delta t}\,\mathbf{v}_n \;+\; \frac{1-\gamma}{\gamma}\,\dot{\mathbf{v}}_n\right].\end{aligned} \tag{3.21}$$

Once $\mathbf{d}_{n+1}$ is obtained, $\dot{\mathbf{d}}_{n+1}$, $\mathbf{v}_{n+1}$, and $\dot{\mathbf{v}}_{n+1}$ can be computed using Equations (3.14), (3.17), and (3.18), respectively.

$$\mathbf{M}\,\ddot{\mathbf{d}}_{n+\alpha} \;+\; \mathbf{C}\,\dot{\mathbf{d}}_{n+\alpha} \;+\; \mathbf{K}\,\mathbf{d}_{n+\alpha} \;=\; \mathbf{F}_{n+\alpha}$$

$$\begin{aligned}
\mathbf{F}_{n+\alpha} &= \alpha\,\mathbf{F}_{n+1} \;+\; (1-\alpha)\,\mathbf{F}_n \\
\mathbf{d}_{n+\alpha} &= \alpha\,\mathbf{d}_{n+1} \;+\; (1-\alpha)\,\mathbf{d}_n \\
\dot{\mathbf{d}}_{n+\alpha} &= \frac{\mathbf{d}_{n+1} \;-\; \mathbf{d}_n}{\Delta t} \\
\ddot{\mathbf{d}}_{n+\alpha} &= \frac{\dot{\mathbf{d}}_{n+1} \;-\; \dot{\mathbf{d}}_n}{\Delta t} \\
\dot{\mathbf{d}}_{n+1} &= \frac{\mathbf{d}_{n+1} \;-\; \mathbf{d}_n}{\alpha\,\Delta t} \;-\; \frac{1-\alpha}{\alpha}\,\dot{\mathbf{d}}_n
\end{aligned}$$

Box 8: Summary of GM for second order problems. The coefficient α is given in Box 2.

$$\mathbf{M}\,\dot{\mathbf{v}}_{n+\beta} \;+\; \mathbf{C}\,\mathbf{v}_{n+\alpha} \;+\; \mathbf{K}\,\mathbf{d}_{n+\alpha} \;=\; \mathbf{F}_{n+\alpha}$$

$$\begin{aligned}
\mathbf{F}_{n+\alpha} &= \alpha\,\mathbf{F}_{n+1} \;+\; (1-\alpha)\,\mathbf{F}_n \\
\mathbf{d}_{n+\alpha} &= \alpha\,\mathbf{d}_{n+1} \;+\; (1-\alpha)\,\mathbf{d}_n \\
\mathbf{v}_{n+\alpha} &= \alpha\,\mathbf{v}_{n+1} \;+\; (1-\alpha)\,\mathbf{v}_n \\
\dot{\mathbf{v}}_{n+\beta} &= \beta_0\,\dot{\mathbf{v}}_{n+1} \;+\; \beta_1\,\dot{\mathbf{v}}_n \\
\mathbf{v}_{n+1} &= \frac{\beta_0\,\dot{\mathbf{d}}_{n+1} \;+\; \beta_1\,\dot{\mathbf{d}}_n}{\alpha} - \frac{1-\alpha}{\alpha}\,\mathbf{v}_n \\
\dot{\mathbf{v}}_{n+1} &= \frac{\mathbf{v}_{n+1} \;-\; \mathbf{v}_n}{\Delta t\,\gamma} \;-\; \frac{1 \;-\; \gamma}{\gamma}\,\dot{\mathbf{v}}_n \\
\dot{\mathbf{d}}_{n+1} &= \frac{\mathbf{d}_{n+1} \;-\; \mathbf{d}_n}{\Delta t\,\gamma} \;-\; \frac{1 \;-\; \gamma}{\gamma}\,\dot{\mathbf{d}}_n
\end{aligned}$$

Box 9: Summary of GA-2 for second order problems. The coefficients α, β_0, β_1 and γ are given in Box 3.

$$\mathbf{M}\,\dot{\mathbf{v}}_{n+\beta} \;+\; \mathbf{C}\,\mathbf{v}_{n+\alpha} \;+\; \mathbf{K}\,\mathbf{d}_{n+\alpha} \;=\; \mathbf{F}_{n+\alpha}$$

$$\begin{aligned}
\mathbf{F}_{n+\alpha} &= \alpha\,\mathbf{F}_{n+1} \;+\; (1-\alpha)\,\mathbf{F}_n \\
\mathbf{d}_{n+\alpha} &= \alpha\,\mathbf{d}_{n+1} \;+\; (1-\alpha)\,\mathbf{d}_n \\
\mathbf{v}_{n+\alpha} &= \alpha\,\mathbf{v}_{n+1} \;+\; (1-\alpha)\,\mathbf{v}_n \\
\dot{\mathbf{v}}_{n+\beta} &= \beta_0\,\dot{\mathbf{v}}_{n+1} \;+\; \beta_1\,\dot{\mathbf{v}}_n \;+\; \beta_2\,\ddot{\mathbf{v}}_n\,\Delta t
\end{aligned}$$

$$\begin{aligned}
\mathbf{v}_{n+1} &= \frac{\beta_0\,\dot{\mathbf{d}}_{n+1} \;+\; \beta_1\,\dot{\mathbf{d}}_n \;+\; \beta_2\,\ddot{\mathbf{d}}_n\,\Delta t}{\alpha} \;-\; \frac{1-\alpha}{\alpha}\,\mathbf{v}_n \\
\mathbf{v}_{n+1}^{(i+1)'} &= \frac{\mathbf{v}_{n+1}^{(i)'} - \mathbf{v}_n^{(i)'}}{\Delta t\,\gamma} + \frac{1-\gamma}{\gamma}\,\mathbf{v}_n^{(i+1)'} \qquad \text{for} \qquad i = 0, 1 \\
\mathbf{d}_{n+1}^{(i+1)'} &= \frac{\mathbf{d}_{n+1}^{(i)'} - \mathbf{d}_n^{(i)'}}{\Delta t\,\gamma} + \frac{1-\gamma}{\gamma}\,\mathbf{d}_n^{(i+1)'} \qquad \text{for} \qquad i = 0, 1
\end{aligned}$$

Box 10: Summary of GA-23 for second order problems. The coefficients α, β_0, β_1, β_2 and γ are given in Box 4.

3.2. Analysis of the Methods GA-23 and GA-234

This section investigates the numerical properties of the new GA-23 and GA-234 formulations for second order problems. The coupled equations of motion are applied to a single-degree-of-freedom system for analysis. The governing equation of the unforced system is given by

$$\ddot{d} + 2\,\xi\,\omega\,\dot{d} + \omega^2 d = 0, \tag{3.22}$$

where ω denotes the natural frequency of the system, and ξ represents the damping ratio. The corresponding oscillation period is defined as $T = \frac{2\pi}{\omega}$. The solutions at t_{n+1} can be expressed as

$$\mathbf{X_{n+1}} \;=\; \mathbf{A}\,\mathbf{X_n}, \tag{3.23}$$

$$\mathbf{M}\,\dot{\mathbf{v}}_{n+\beta} \;+\; \mathbf{C}\,\mathbf{v}_{n+\alpha} \;+\; \mathbf{K}\,\mathbf{d}_{n+\alpha} \;=\; \mathbf{F}_{n+\alpha}$$

$$\mathbf{F}_{n+\alpha} \;=\; \alpha\,\mathbf{F}_{n+1} + (1-\alpha)\,\mathbf{F}_n$$

$$\mathbf{d}_{n+\alpha} \;=\; \alpha\,\mathbf{d}_{n+1} + (1-\alpha)\,\mathbf{d}_n$$

$$\mathbf{v}_{n+\alpha} \;=\; \alpha\,\mathbf{v}_{n+1} + (1-\alpha)\,\mathbf{v}_n$$

$$\dot{\mathbf{v}}_{n+\beta} \;=\; \beta_0\,\dot{\mathbf{v}}_{n+1} \;+\; \beta_1\,\dot{\mathbf{v}}_n + \beta_2\,\ddot{\mathbf{v}}_n\,\Delta t \;+\; \beta_3\,\dddot{\mathbf{v}}_n\,\Delta t^2$$

$$\mathbf{v}_{n+1} \;=\; \frac{\beta_0\,\dot{\mathbf{d}}_{n+1} \;+\; \beta_1\,\dot{\mathbf{d}}_n \;+\; \beta_2\,\ddot{\mathbf{d}}_n\,\Delta t \;+\; \beta_3\,\dddot{\mathbf{d}}_n\,\Delta t^2}{\alpha} \;-\; \frac{1-\alpha}{\alpha}\,\mathbf{v}_n$$

$$\mathbf{v}_{n+1}^{(i+1)'} \;=\; \frac{\mathbf{v}_{n+1}^{(i)'} - \mathbf{v}_n^{(i)'}}{\Delta t\,\gamma} - \frac{1-\gamma}{\gamma}\,\mathbf{v}_n^{(i+1)'} \qquad \text{for} \qquad i = 0, 1, 2$$

$$\mathbf{d}_{n+1}^{(i+1)'} \;=\; \frac{\mathbf{d}_{n+1}^{(i)'} - \mathbf{d}_n^{(i)'}}{\Delta t\,\gamma} - \frac{1-\gamma}{\gamma}\,\mathbf{d}_n^{(i+1)'} \qquad \text{for} \qquad i = 0, 1, 2$$

Box 11: Summary of GA-234 for second order problems. The coefficients α, β_0, β_1, β_2, β_3 and γ are given in Box 5.

where

$$\text{GA-2:} \quad \mathbf{X_n} = \left\{ \; d_n,\, v_n\Delta t,\, \dot{d}_n\Delta t,\, \dot{v}_n\Delta t^2 \; \right\}^T$$

$$\text{GA-23:} \quad \mathbf{X_n} = \left\{ \; d_n,\, v_n\Delta t,\, \dot{d}_n\Delta t,\, \dot{v}_n\Delta t^2,\, \ddot{d}_n\Delta t^2,\, \ddot{v}_n\Delta t^3 \; \right\}^T$$

$$\text{GA-234:} \quad \mathbf{X_n} = \left\{ \; d_n,\, v_n\Delta t,\, \dot{d}_n\Delta t,\, \dot{v}_n\Delta t^2,\, \ddot{d}_n\Delta t^2,\, \ddot{v}_n\Delta t^3,\, \dddot{d}_n\Delta t^3,\, \dddot{v}_n\Delta t^4 \; \right\}^T$$

and $\mathbf{A}$ denotes the corresponding amplification matrix. The coefficients of the amplification matrices depend on ω, ξ, Δt, and the parameters α, β_i, and γ. These matrices can be derived using symbolic mathematical software. The amplification matrix of GA-2 with $\rho_\infty = 0$ is presented in Equation (3.24). The corresponding matrices for GA-23 and GA-234 are comparatively lengthy and are therefore omitted for brevity.

$$\mathbf{A} = \begin{bmatrix} \dfrac{12\,\Delta t\,\omega\,\xi + 9}{\eta} & \dfrac{4\,\Delta t\,\omega\,\xi + 3}{\eta} & \dfrac{6}{\eta} & \dfrac{2}{\eta} \\ \dfrac{4(\Delta t\,\omega)^2}{\eta} & \dfrac{4\,\Delta t\,\omega\,\xi + 3}{\eta} & \dfrac{6}{\eta} & \dfrac{2}{\eta} \\ \dfrac{6(\Delta t\,\omega)^2}{\eta} & -\dfrac{2(\Delta t\,\omega)^2}{\eta} & \dfrac{9}{\eta} & \dfrac{3}{\eta} \\ \dfrac{6(\Delta t\,\omega)^2}{\eta} & -\dfrac{2(\Delta t\,\omega)^2}{\eta} & -\dfrac{\Delta t\,\omega\,(3\xi + 4\Delta t\,\omega)}{\eta} & \dfrac{3}{\eta} \end{bmatrix} \tag{3.24}$$

where $\eta = 4\,\Delta t^2\,\omega^2 + 12\,\xi\,\Delta t\,\omega + 9$. The spectral radius, $\rho(\mathbf{A})$, is defined as $\rho = \max(|\lambda_1|, |\lambda_2|, \ldots, |\lambda_d|)$, where λ_i is the i-th eigenvalue of $\mathbf{A}$ and $d = 4, 6, 8$ for GA-2, GA-23 and GA-234, respectively. A scheme is unconditionally stable if $\rho(\mathbf{A}) \leq 1$ for any $\Delta t \geq 0$.

Figures 3.1 and 3.2 show the eigenvalues of the amplification matrices in the complex plane and the spectral radii as a function of time step size for different values of ρ_∞, respectively. Figure 3.1 confirms the unconditional stability of all methods, as the eigenvalues remain within or on the unit circle across all tested cases, ensuring no numerical instability for any time step size. Similarly, Figure 3.2 demonstrates that the spectral radius $\rho(\mathbf{A})$ remains at or below one for all time step sizes, further reinforcing stability. Moreover, Figure 3.2 indicates that GA-23 and GA-234 shift the onset of significant numerical damping to larger time steps, reducing artificial dissipation in the low-frequency regime compared to GA-2.

To evaluate numerical dissipation and dispersion, the algorithmic damping ratio and the relative period error are defined as follows

$$\bar{\xi} = -\frac{\ln|\lambda|}{\bar{\Omega}} \qquad \text{and} \qquad \varepsilon_T = \frac{\bar{T} - T}{T}, \tag{3.25}$$

where

$$\bar{T} = \frac{2\pi}{\bar{\omega}}, \qquad \bar{\omega} = \frac{\bar{\Omega}}{\Delta t}, \qquad \bar{\Omega} = \arg(\lambda). \tag{3.26}$$

Figures 3.3 and 3.4 display the relative period errors and algorithmic damping ratios over the time step size, respectively. Notably, GA-23 and GA-234 exhibit smaller approximation errors compared to GA-2. Additionally, GA-234 is more accurate than GA-23.

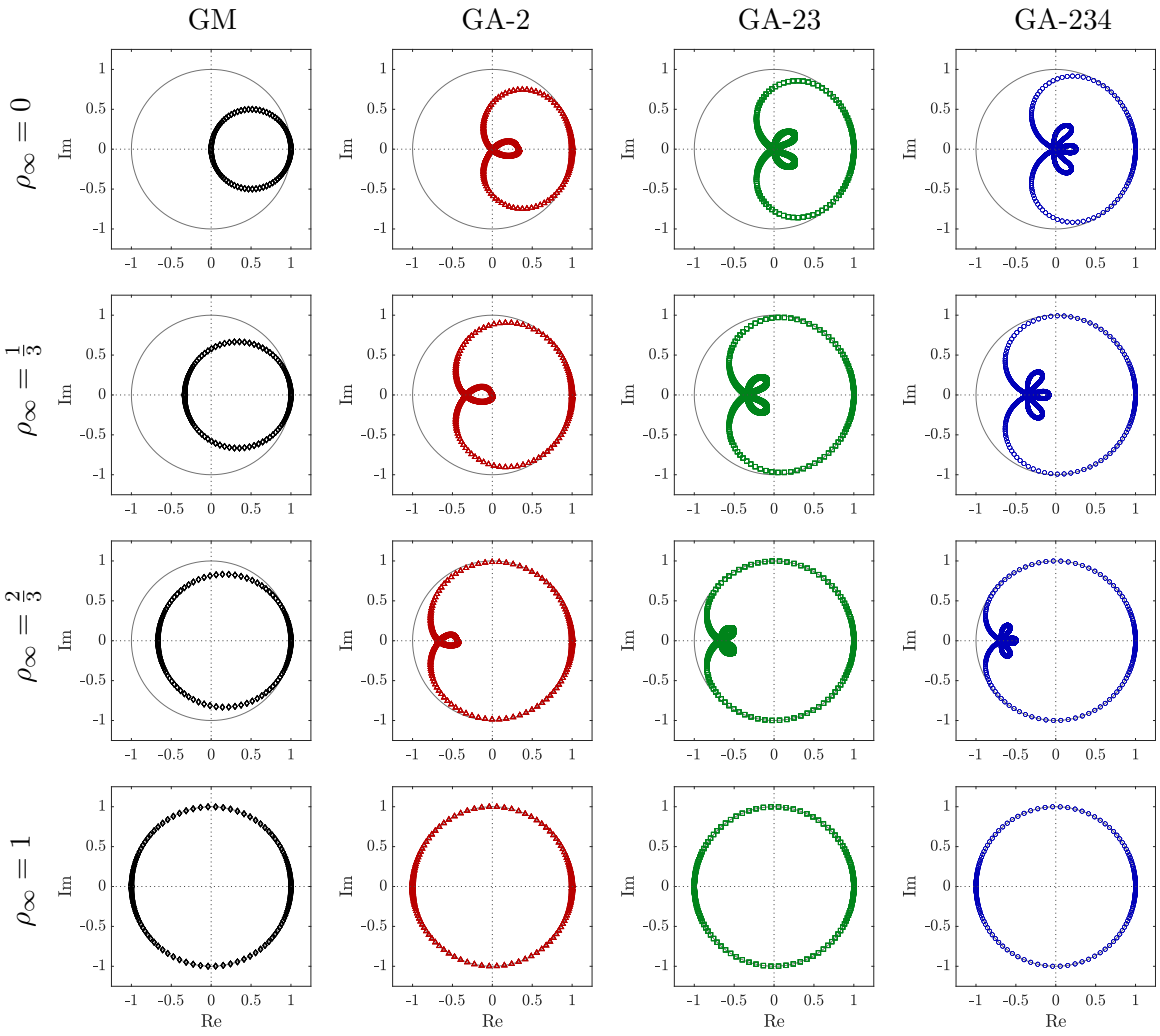

Figure 3.1.: Eigenvalues of the amplification matrices for $\xi = 0$, displayed in the complex plane for a range of time step sizes Δt.

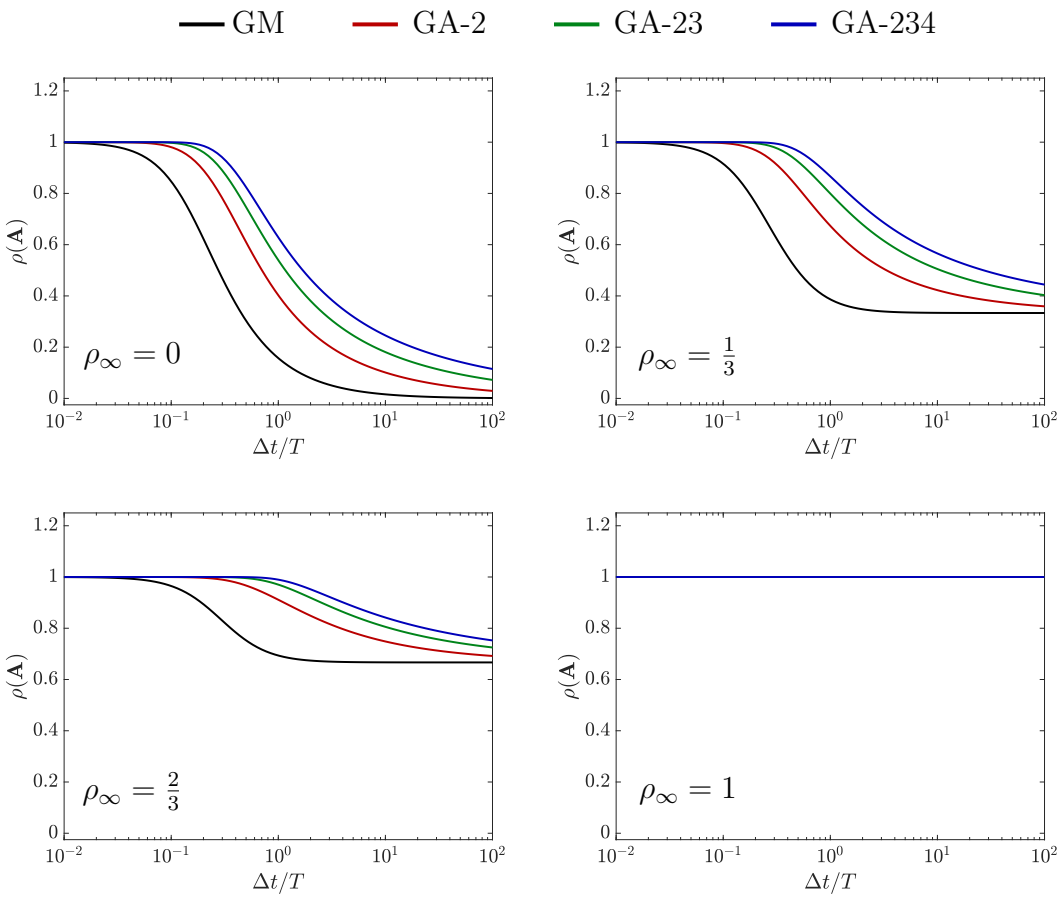

Figure 3.2.: Spectral radii of GM, GA-2, GA-23 and GA-234 for $\xi = 0$.

3.3. Backward Difference Formulae

For $\rho_\infty = 0$, the GA-23 and GA-234 schemes can be reformulated as backward difference formulae, as discussed in Section 2.4. Boxes 12 and 13 present the BDF-23 and BDF-234 formulations for second order problems.

For linear problems with correct initial conditions, the numerical properties of the BDF methods are equivalent to those of their GA counterparts, resulting in identical solutions. Since GA-23 and GA-234 demonstrate improved accuracy over GA-2, this advantage also applies to BDF-23 and BDF-234 in comparison with the standard BDF-2 scheme. As a result, integrating these schemes into any existing codes based on BDF-2 is both straightforward and advantageous,

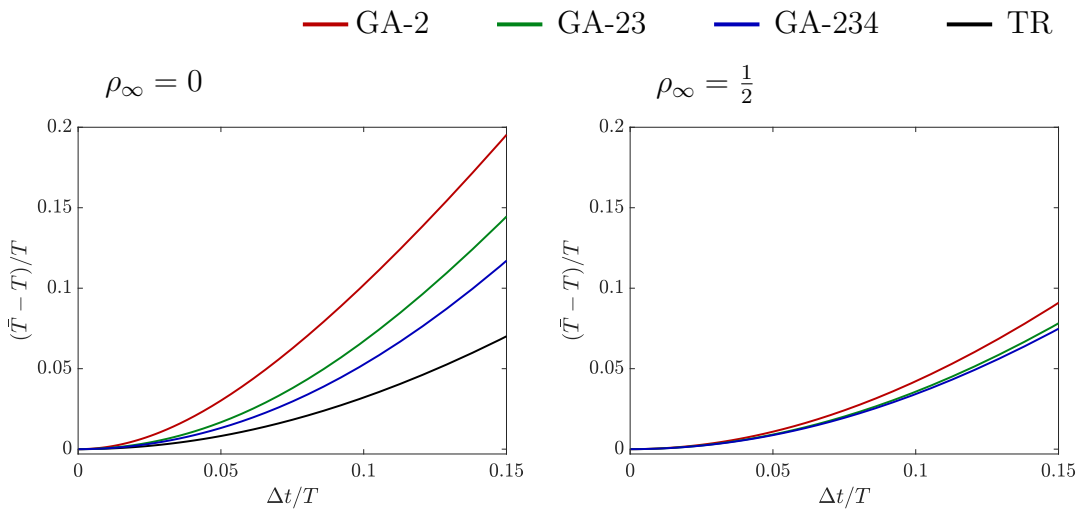

Figure 3.3.: Relative period error of GA-2, GA-23 and GA-234 $\xi = 0$.

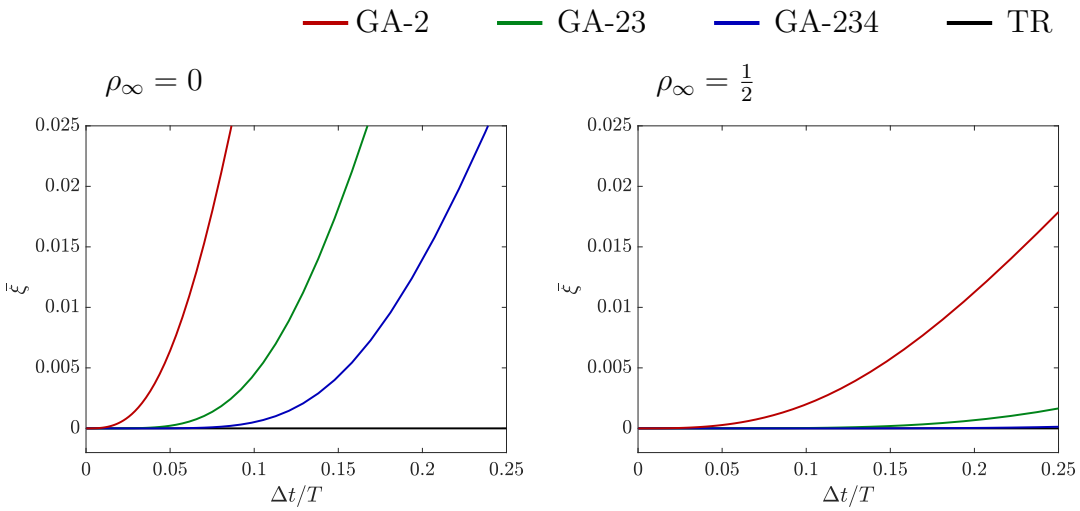

Figure 3.4.: Algorithmic damping ratios of GA-2, GA-23 and GA-234 for $\xi = 0$.

yielding greater accuracy with negligible additional storage cost. In the numerical examples presented in Sections 3.5 to 3.9, BDF-23 and BDF-234 are represented by GA-23 and GA-234 with $\rho_\infty = 0$.

$$\mathbf{M}\,\ddot{\mathbf{d}}_{n+1} \;+\; \mathbf{C}\,\dot{\mathbf{d}}_{n+1} \;+\; \mathbf{K}\,\mathbf{d}_{n+1} \;=\; \mathbf{F}_{n+1}$$

$$\ddot{\mathbf{d}}_{n+1} \;=\; \frac{10\,\dot{\mathbf{d}}_{n+1} - 15\,\dot{\mathbf{d}}_{n} + 6\,\dot{\mathbf{d}}_{n-1} - \dot{\mathbf{d}}_{n-2}}{6\,\Delta t}$$

$$\dot{\mathbf{d}}_{n+1} \;=\; \frac{10\,\mathbf{d}_{n+1} - 15\,\mathbf{d}_{n} + 6\,\mathbf{d}_{n-1} - \mathbf{d}_{n-2}}{6\,\Delta t}$$

Box 12: Summary of method BDF-23 for structural dynamics.

$$\mathbf{M}\,\ddot{\mathbf{d}}_{n+1} \;+\; \mathbf{C}\,\dot{\mathbf{d}}_{n+1} \;+\; \mathbf{K}\,\mathbf{d}_{n+1} \;=\; \mathbf{F}_{n+1}$$

$$\ddot{\mathbf{d}}_{n+1} \;=\; \frac{35\,\dot{\mathbf{d}}_{n+1} - 56\,\dot{\mathbf{d}}_{n} + 28\,\dot{\mathbf{d}}_{n-1} - 8\,\dot{\mathbf{d}}_{n-2} + \dot{\mathbf{d}}_{n-3}}{20\,\Delta t}$$

$$\dot{\mathbf{d}}_{n+1} \;=\; \frac{35\,\mathbf{d}_{n+1} - 56\,\mathbf{d}_{n} + 28\,\mathbf{d}_{n-1} - 8\,\mathbf{d}_{n-2} + \mathbf{d}_{n-3}}{20\,\Delta t}$$

Box 13: Summary of method BDF-234 for structural dynamics.

3.4. Comparison with the Bathe Method

The Bathe method is a well-known composite or multi-sub-step scheme. The original Bathe method [7, 8] combines the trapezoidal rule, which improves accuracy, with the BDF-2 method, which enhances stability. This combination ensures unconditional stability while controlling numerical dissipation, making it highly effective for structural dynamics and fluid-structure interaction problems [61, 94].

Note that the GA-23 and GA-234 schemes are developed based on a completely different approach compared to the Bathe method. While the latter divides each time step into two substeps and applies different time integration schemes to each, GA-23 and GA-234 are single-step methods that use a linear combination of second and higher order schemes.

Several variations of the Bathe method have been proposed. These include the energy-conserving Bathe method, which modifies the original scheme to conserve energy over long simulations [6]. The β_1/β_2-Bathe method introduces two adjustable parameters that allow users to control numerical damping [89]. The controllable ρ_∞-Bathe method provides tunable parameters for more precise control of stability and accuracy [96]. In addition, the modified Bathe method for nonlinear problems improves convergence and efficiency in large-scale nonlinear systems [90], and the adaptive Bathe method incorporates adaptive time-stepping to dynamically adjust step sizes based on system behaviour [86]. The analysis and numerical results in the following sections refer to the original Bathe method with $\gamma = 2 - \sqrt{2}$ [7].

The following remarks comment on computational cost and implementation, accuracy and suitability for modelling wave propagation of the two strategies.

- **Computational cost and implementation:** Due to its multi-sub-step nature, the implementation of the Bathe method is more intrusive. It requires solving two global systems. In many cases, the stiffness matrices involved are either identical or differ only by scalar factors, allowing the matrix factorisation to be reused, which keeps the additional computational cost relatively low. However, in nonlinear problems, the two stiffness matrices depend on different configurations, making the computational cost per time step significantly higher.

- **Accuracy:** Figure 3.5 shows the spectral radii for GA-2, GA-23, GA-234, and the Bathe method, while Figure 3.6 presents the algorithmic damping ratio and the relative period error. Due to its higher computational cost, the Bathe method is evaluated with time step sizes of Δt and $2\Delta t$, referred to as B-Δt and B-$2\Delta t$, respectively. These serve as upper and lower bounds for comparison with GA-2, GA-23, and GA-234. In Figure 3.5, for $\rho_\infty = 0$, GA-23 and B-$2\Delta t$ exhibit similar performance, while GA-234 lies between B-$2\Delta t$ and B-Δt. Numerical results obtained with B-Δt and B-$2\Delta t$ are provided in Section 3.6.

- **Modelling wave propagation:** The Bathe method has been shown to be highly effective in solving wave propagation problems in elastic solid materials [80, 85], particularly in accurately capturing velocity discontinuities. For GA-23 and GA-234, the combination of second order and higher order schemes results in improved accuracy for smooth wave propagation but also introduces a requirement for more smoothness. As a result, they dissipate shock wave discontinuities more quickly than the Bathe method. However, for smoothly propagating waves, GA-23 and GA-234 demonstrate exceptional accuracy, as shown in Section 3.9.

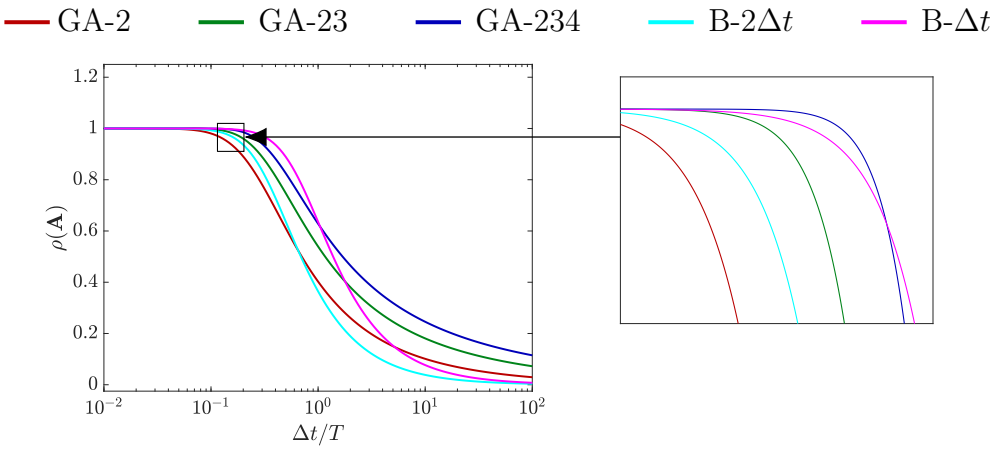

Figure 3.5.: Spectral radii of the GA methods with $\rho_\infty = 0$ and the Bathe method.

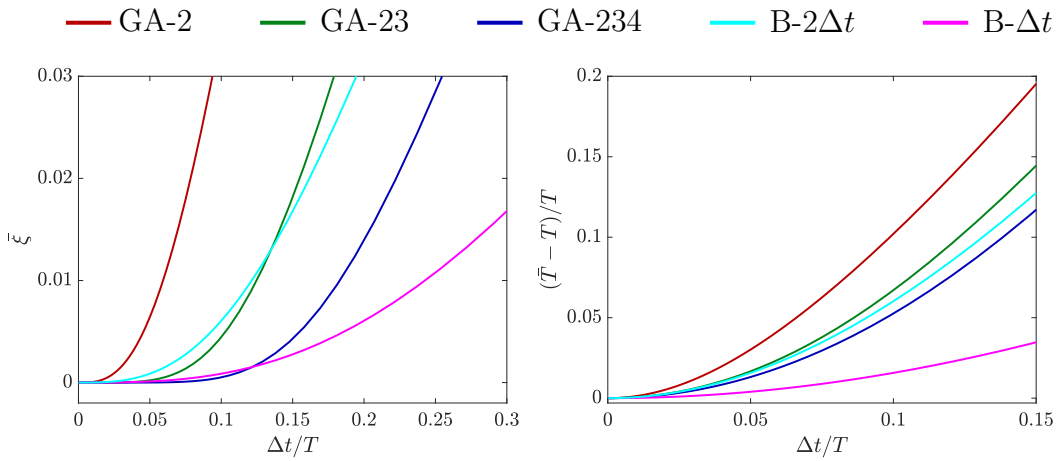

Figure 3.6.: Algorithmic damping ratios and relative period errors of the GA methods with $\rho_\infty = 0$ and the Bathe method.

3.5. Example 1: Linear Single Degree of Freedom Oscillator

To evaluate the performance and accuracy of the new GA-23 and GA-234 formulations, the single-degree-of-freedom system defined by Equation (3.22) is used. The frequency is set to $\omega = 1$ rad/s, which corresponds to an oscillation period of $T = 2\pi$ s. The initial displacement and velocity are specified as $d(0) = 1$ m and $\dot{d}(0) = 0$ m/s, respectively. Figures 3.7 and 3.8 present the responses obtained using the exact solution, alongside results computed with the GA-2, GA-23, and GA-234 schemes for $\xi = 0.0$ and $\xi = 0.1$, across a range of time step sizes and values of ρ_∞. Based on these results, the following observations are made

- GA-2 exhibits the greatest deviation from the exact solution across all tested cases.
- GA-23 demonstrates improved accuracy in comparison with GA-2, but still shows a noticeable loss of accuracy at larger time step sizes, particularly when $\rho_\infty = 0$.
- GA-234 is the most accurate method, consistently producing results that closely align with the exact solution across all cases.

Figure 3.9 displays the convergence of the numerical solutions for different values of ρ_∞. The error ϵ is determined by comparing the exact displacement $\tilde{d}$ with the numerical displacement $\bar{d}$ from each method, as given by

$$\epsilon(t_N) = \sqrt{\frac{t_N}{N} \sum_{i=1}^{N} \left| \tilde{d}(t_i) - \bar{d}(t_i) \right|^2}, \tag{3.27}$$

where N is the number of time steps used in the respective computation to reach $t_N = 35$.

As ρ_∞ increases towards 1, the differences between GA-2, GA-23, and GA-234 become less pronounced, and eventually, all methods converge to the trapezoidal rule for $\rho_\infty = 1$. For $\rho_\infty = 0$, the improvement from GA-2 to

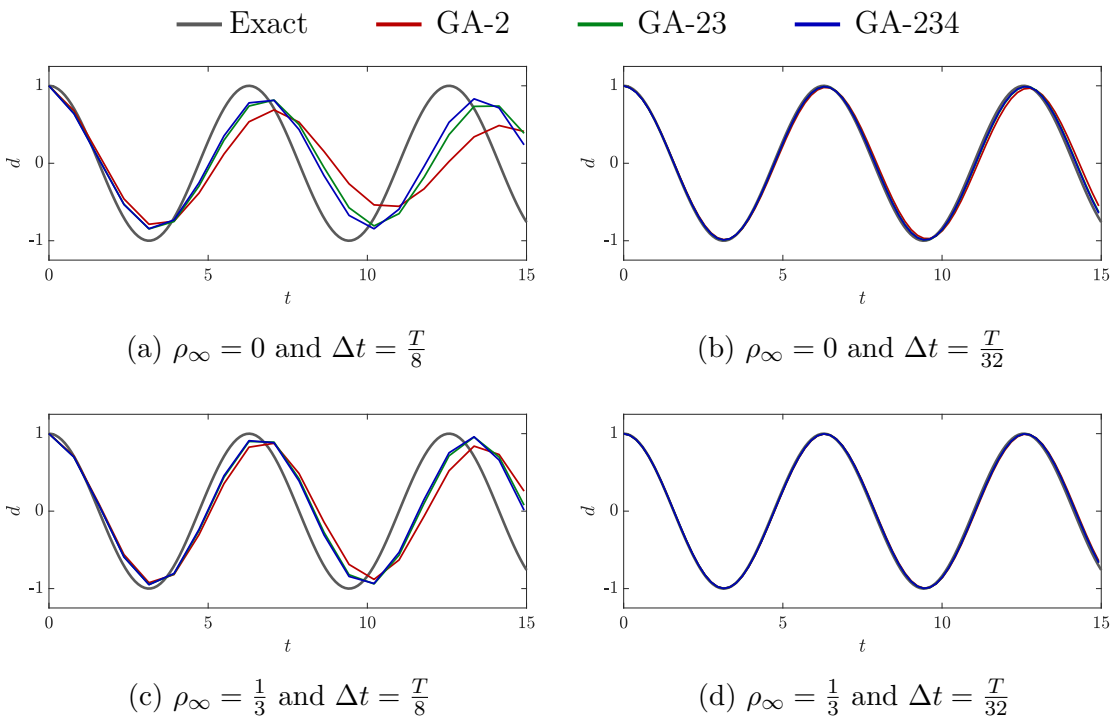

(a) $\rho_\infty = 0$ and $\Delta t = \frac{T}{8}$

(b) $\rho_\infty = 0$ and $\Delta t = \frac{T}{32}$

(c) $\rho_\infty = \frac{1}{3}$ and $\Delta t = \frac{T}{8}$

(d) $\rho_\infty = \frac{1}{3}$ and $\Delta t = \frac{T}{32}$

Figure 3.7.: Linear single degree of freedom oscillator; response obtained for $\xi = 0.0$.

GA-234 is substantial, particularly for time steps around $\Delta t = T/32$. The accuracy gain from GA-2 to GA-234 is comparable to that observed in the transition from GM (a first order method) to GA-2 (a second order method). This trend is also evident in Figures 3.7 and 3.8 for $\rho_\infty = 0$. This observation is crucial, as the time step range $T/50 < \Delta t < T/25$ is particularly relevant in industrial applications.

3.6. Example 2: Linear Stiff-Soft Spring System, Free Oscillation

To further evaluate the numerical damping properties of GA-23 and GA-234, the two-degree-of-freedom system depicted in Figure 3.10 is considered. This system is simple enough for theoretical analysis, yet sufficiently complex to highlight differences in numerical damping behaviour, making it a standard test case for assessing time integration methods. The setup consists of two

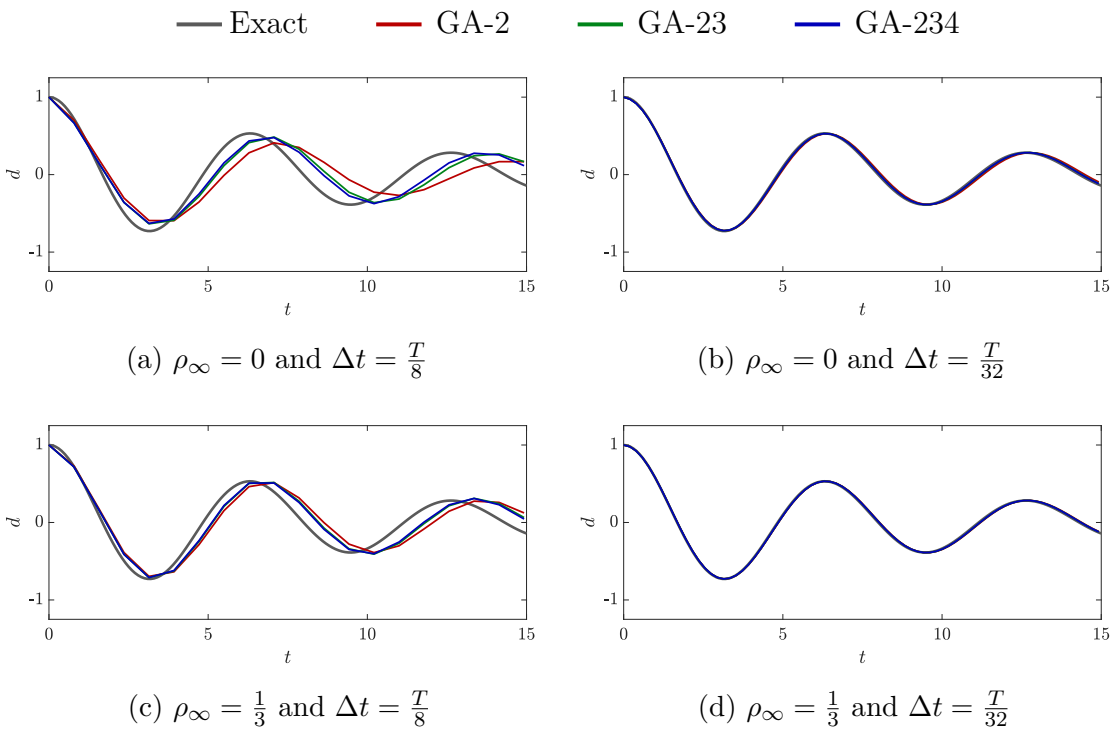

(a) $\rho_\infty = 0$ and $\Delta t = \frac{T}{8}$

(b) $\rho_\infty = 0$ and $\Delta t = \frac{T}{32}$

(c) $\rho_\infty = \frac{1}{3}$ and $\Delta t = \frac{T}{8}$

(d) $\rho_\infty = \frac{1}{3}$ and $\Delta t = \frac{T}{32}$

Figure 3.8.: Linear single degree of freedom oscillator; response obtained for $\xi = 0.1$.

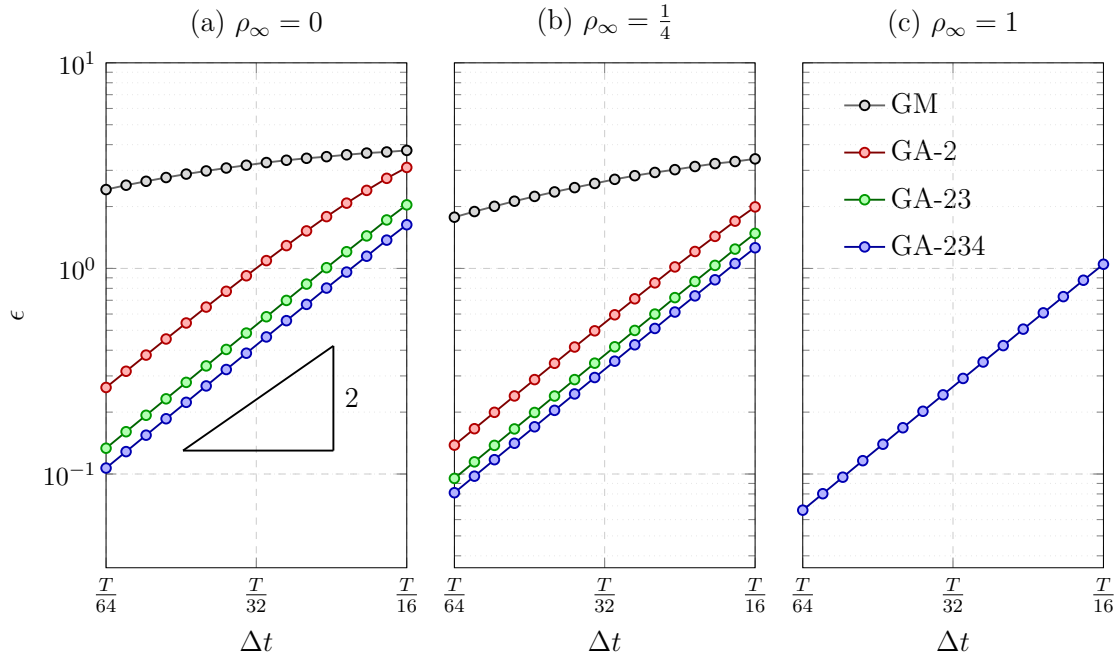

Figure 3.9.: Linear single degree of freedom oscillator; convergence rates.

equal masses, $m_1 = m_2 = 1$ kg, connected by two springs with stiffness values $k_1 = 1$ N/m and $k_2 = 100$ N/m. The governing equations can be expressed in matrix form as

$$\begin{bmatrix} m_1 & 0 \\ 0 & m_2 \end{bmatrix} \begin{Bmatrix} \ddot{d}_1 \\ \ddot{d}_2 \end{Bmatrix} + \begin{bmatrix} k_1 + k_2 & -k_2 \\ -k_2 & k_2 \end{bmatrix} \begin{Bmatrix} d_1 \\ d_2 \end{Bmatrix} = \begin{Bmatrix} 0 \\ 0 \end{Bmatrix}. \tag{3.28}$$

The initial conditions are specified as $d_1(0) = 0$ m and $\dot{d}_1(0) = 0$ m/s for mass 1, and $d_2(0) = 1$ m and $\dot{d}_2(0) = 0$ m/s for mass 2. Due to the large stiffness ratio, the oscillation associated with the high-frequency mode is not of interest and is therefore not resolved in the analysis. The lower-frequency mode dominates the system response, resulting in an oscillation period of $T = 8.897$ s.

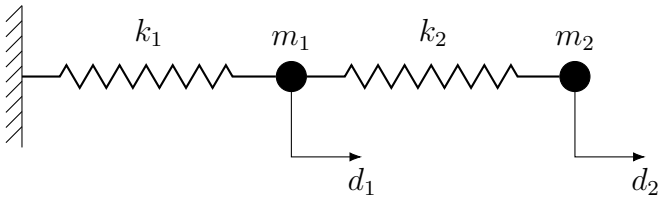

Figure 3.10.: Linear stiff-soft spring system, free oscillation; two-degree-of-freedom system.

The simulation is performed with GA-2, GA-23, and GA-234 for various values of ρ_∞, along with B-2Δt and B-Δ for $\Delta t = 0.5$. Figure 3.11 shows the responses obtained from the different schemes. The observed oscillation frequencies are summarised in Table 3.1. The following observations are made from Figure 3.11

- The initial conditions cause artificial numerical oscillations for $\rho_\infty = 1$ (trapezoidal rule), which are effectively damped out when smaller values of ρ_∞ are used.

- For $\rho_\infty = 0$, GA-23, GA-234, and the Bathe method demonstrate significantly better dissipation and frequency accuracy compared to GA-2. GA-23 closely matches B-2Δt, while GA-234 achieves results that lie between B-Δt and B-2Δt.
- For $\rho_\infty > 0$, the accuracy of GA-2, GA-23, and GA-234 improves significantly. Notably, GA-2 outperforms B-2Δt for $\rho_\infty = 1/3$.

Method	**Frequency**	**Error (%)**
Analytical	0.1125	-
GA-234 ($\rho_\infty = 0$)	0.1111	1.27
GA-23 ($\rho_\infty = 0$)	0.1108	1.54
GA-2 ($\rho_\infty = 0$)	0.1081	3.94
GA-234 ($\rho_\infty = \frac{1}{3}$)	0.1113	1.13
GA-23 ($\rho_\infty = \frac{1}{3}$)	0.1112	1.19
GA-2 ($\rho_\infty = \frac{1}{3}$)	0.1104	1.91
B-Δt	0.1116	0.86
B-2Δt	0.1103	1.95

Table 3.1.: Linear stiff-soft spring system, free oscillation; comparison of frequencies and error.

3.7. Example 3: Linear Elastic Cantilever Beam

In this example, a linear elastic cantilever beam with a length of $L = 4$ m, a height of $H = 0.2$ m, Young's modulus $E = 1.5 \times 10^{10}$ Pa, Poisson's ratio $\nu = 0.35$, and density $\rho = 1000$ kg/m^3 is considered. The thickness in the third direction is $w = 1$ m.

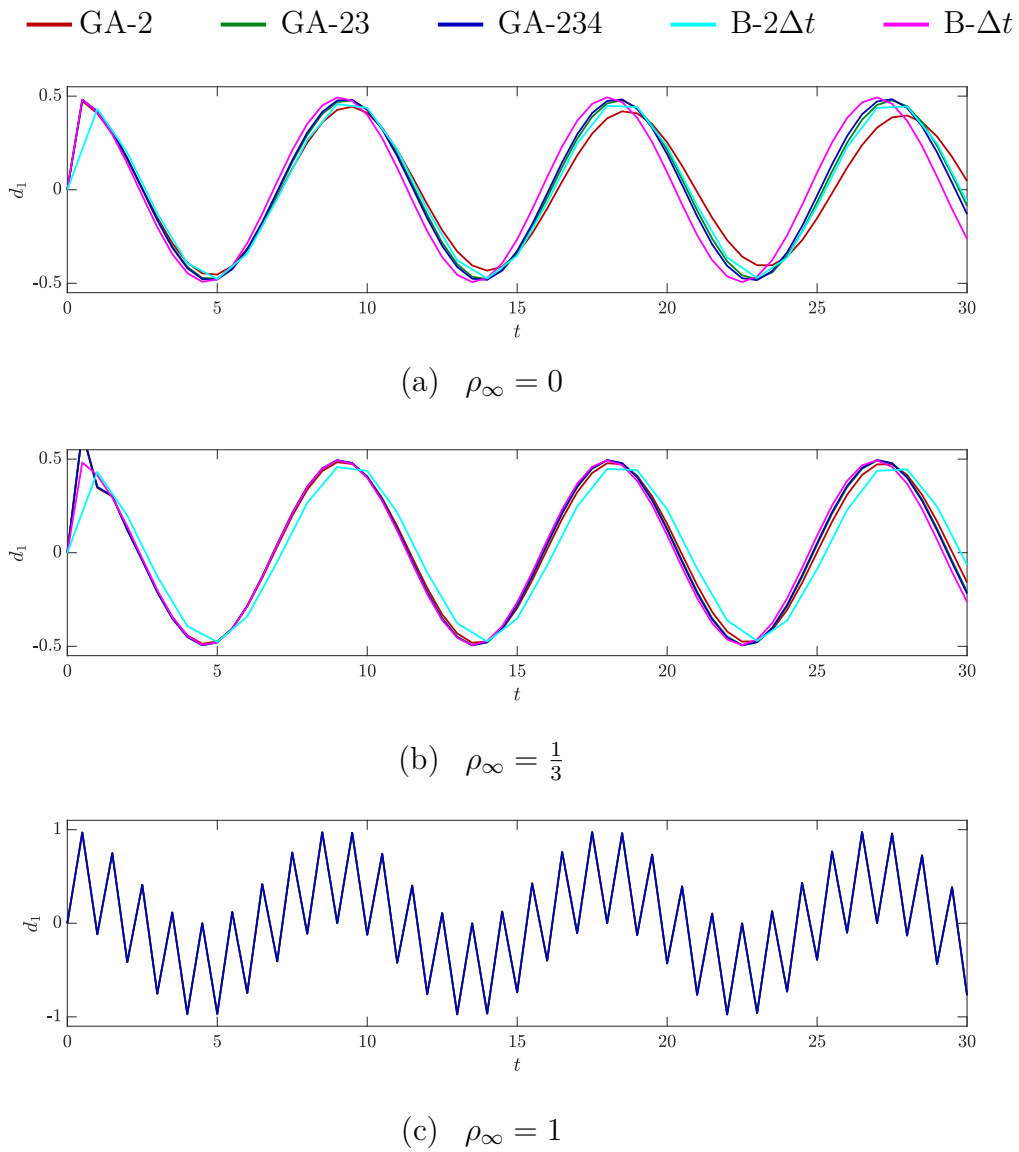

(a) $\rho_\infty = 0$

(b) $\rho_\infty = \frac{1}{3}$

(c) $\rho_\infty = 1$

Figure 3.11.: Linear stiff-soft spring system, free oscillation; response obtained with $\Delta t = 0.5$.

The beam is fully fixed on the left-hand side and free at the other end. The employed mesh consists of 160 nine-noded plane stress elements, as shown in Figure 3.12. Initially, a point load of $P = 0.2$ kN is applied at the central node of the free end. A steady-state analysis is then carried out to obtain the static response, which is used as the initial condition for the dynamic analysis. Figure 3.13 shows a typical deformed configuration. Figure 3.14 presents the

vertical displacement at the central node of the free end against time, obtained using GA-234 with $\rho_\infty = 0$ and a time step of $\Delta t = 0.1$ s. Figures 3.15 and 3.16 respectively show the shear force and bending moment at the clamped end.

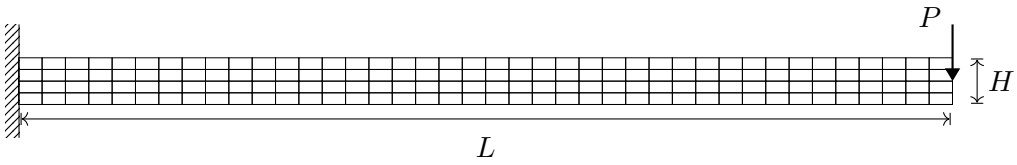

Figure 3.12.: Linear elastic cantilever beam; finite element mesh.

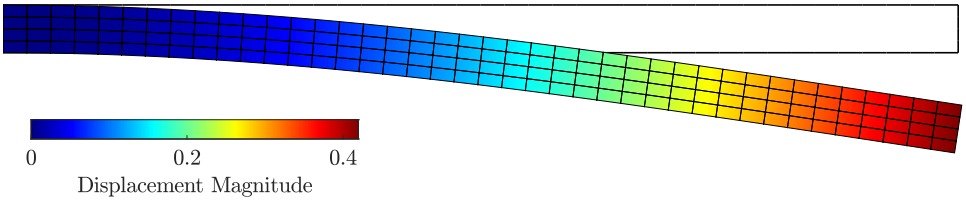

Figure 3.13.: Linear elastic cantilever beam; deformed and undeformed configurations.

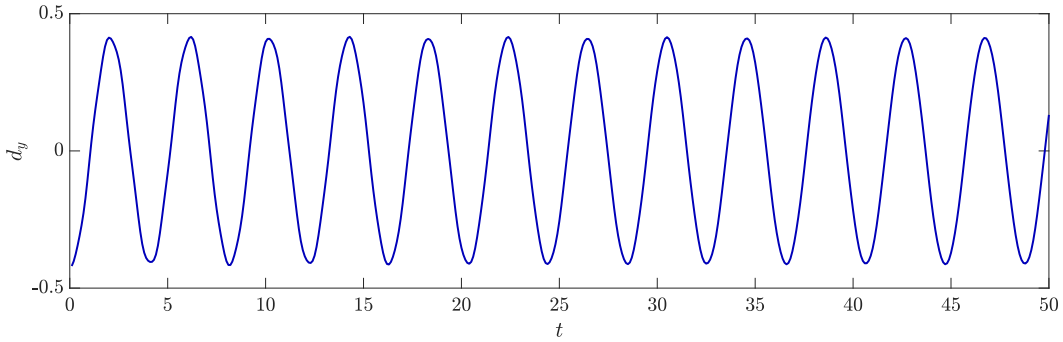

Figure 3.14.: Linear elastic cantilever beam; displacement over time obtained using GA-234, with $\rho_\infty = 0$ and $\Delta t = 0.1$.

A mesh-dependent reference solution is computed using GA-234 with a time step of $\Delta t = 0.0005$ s and $\rho_\infty = 0$. This solution yields a frequency of $f = 0.24531$ Hz, which deviates slightly from the lowest analytical frequency. Table 3.2 presents the frequency errors obtained with the different methods relative to the mesh-dependent reference solution. Figure 3.17 illustrates the frequency convergence for various values of ρ_∞.

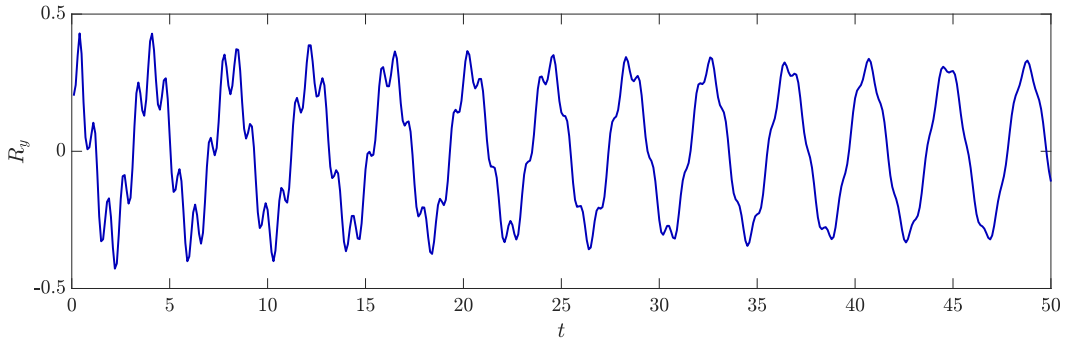

Figure 3.15.: Linear elastic cantilever beam; shear force over time obtained using GA-234, with $\rho_\infty = 0$ and $\Delta t = 0.1$.

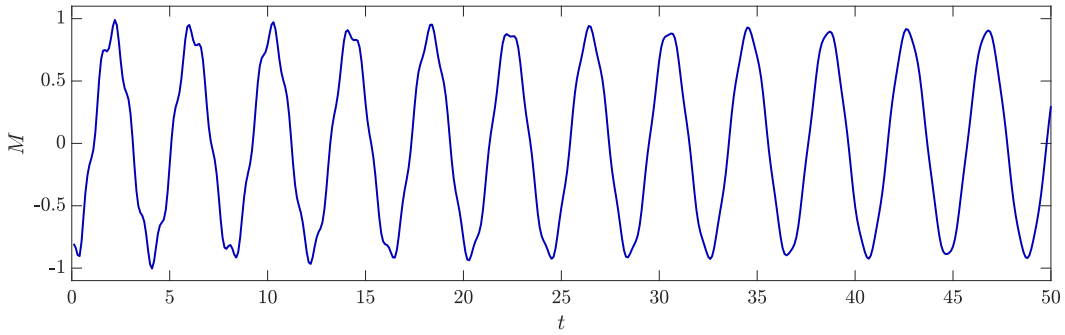

Figure 3.16.: Linear elastic cantilever beam; bending moment over time obtained using GA-234, with $\rho_\infty = 0$ and $\Delta t = 0.1$.

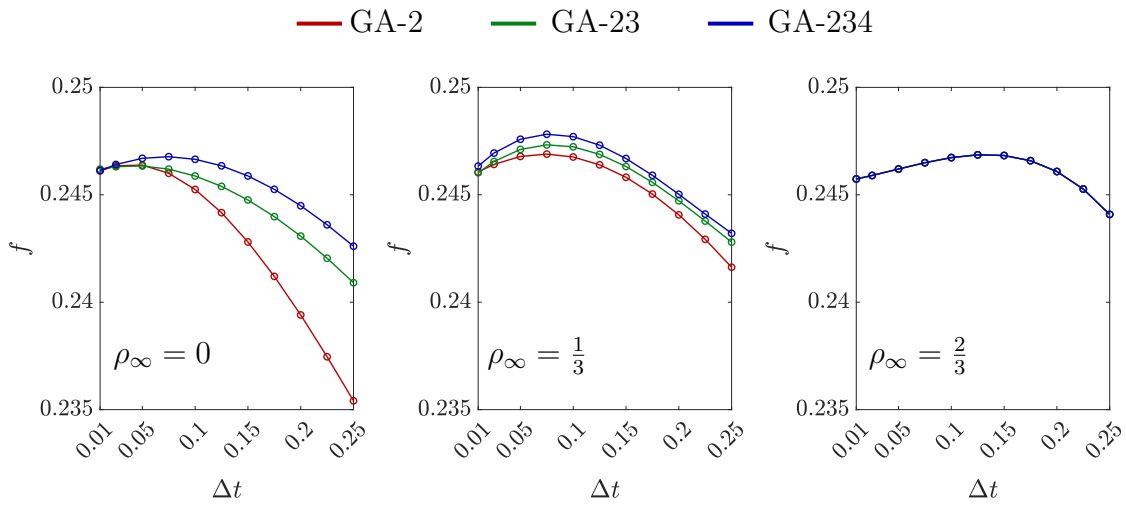

Figure 3.17.: Linear elastic cantilever beam; frequency convergence.

Method	**Frequency**	**Error (%)**
Reference	0.2453	-
GA-234	0.2448	0.21
GA-23	0.2431	0.90
GA-2	0.2397	2.29

Table 3.2.: Linear elastic cantilever beam; frequency comparison obtained with $\rho_\infty = 0$ and $\Delta t = 0.2$.

The results indicate that increasing ρ_∞ enhances frequency accuracy across all methods, as expected. GA-2 exhibits the weakest frequency convergence, especially at larger time steps. GA-23 shows improved accuracy relative to GA-2, though notable discrepancies persist for large Δt. In contrast, GA-234 consistently yields the most accurate frequency estimates across all cases.

3.8. Example 4: Nonlinear Two Degree of Freedom Oscillator

This example assesses the performance of GA-2, GA-23, and GA-234 in a nonlinear setting by analysing the spring pendulum illustrated in Figure 3.18. The pendulum has an initial length of $l_0 = 10$ m, a point mass of $m = 1$ kg, and a spring stiffness of $k = 25$ N/m. The initial conditions are defined such that, in the x-direction, the displacement is $x = 0$ m and the velocity is $\dot{x} = 1$ m/s. In the y-direction, the displacement is $y = -12$ m and the velocity is $\dot{y} = 0$ m/s. The governing equations of the system can be written as

$$\ddot{x}\, m + N \frac{x}{l} = 0, \qquad \ddot{y}\, m + N \frac{y}{l} = 0, \tag{3.29}$$

where $N = \varepsilon k$ is the elastic normal force in the spring, expressed in newtons (N), and the strain is calculated as $\varepsilon = \ln(\lambda)$, with $\lambda = l/l_0$ and l being the current length in metres (m). Figure 3.19 presents the evolution of the elastic force over time, obtained using $\rho_\infty = 0$.

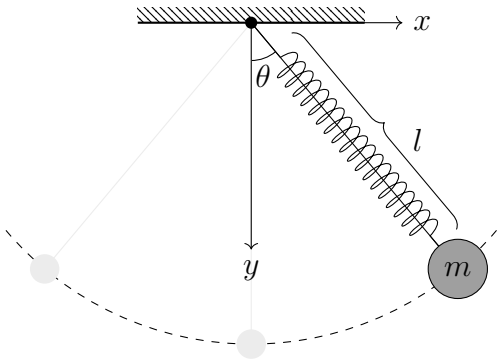

Figure 3.18.: Nonlinear two degree of freedom oscillator.

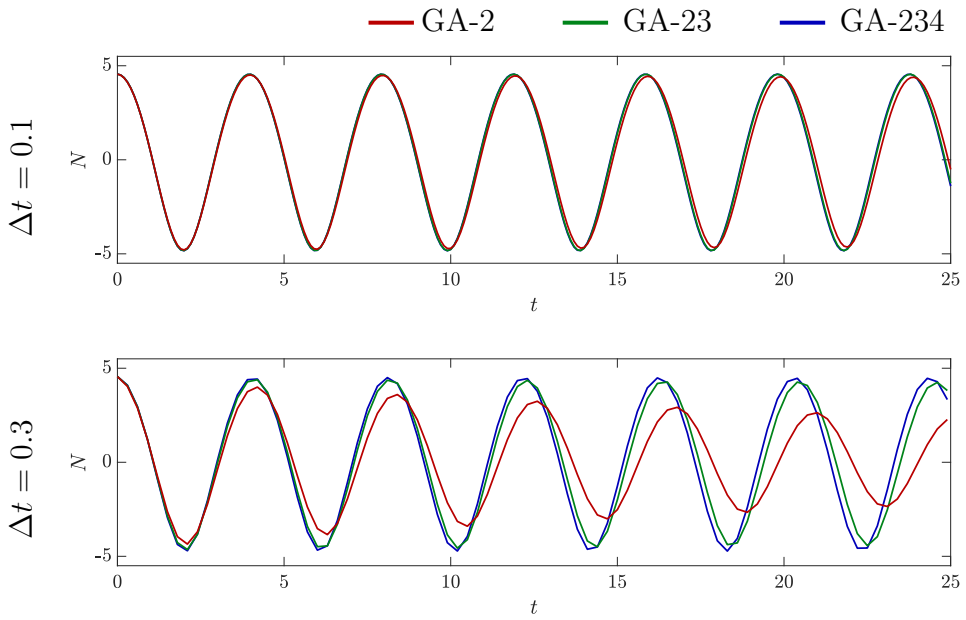

Figure 3.19.: Nonlinear two degree of freedom oscillator; evolution of the elastic normal force obtained using $\rho_\infty = 0$.

Figure 3.20 illustrates the evolution of displacement, velocity, and acceleration in the x-direction, while Figure 3.21 shows phase space trajectories. Both figures depict the results for two time step sizes, $\Delta t = 0.1$ and $\Delta t = 0.3$, alongside a reference solution obtained using GA-234 with $\Delta t = 0.001$. Responses in the y-direction resemble those in Figure 3.20 and have thus been omitted. The total energy of the system is given by

$$E_{\text{total}} = \frac{1}{2} m \left(\dot{x}^2 + \dot{y}^2 \right) + k \left(\lambda \ln(\lambda) - \lambda + 1 \right) l_0 \,. \tag{3.30}$$

Figure 3.22 shows the total energy for GA-2, GA-23, and GA-234, obtained using $\rho_\infty = 0$ and time step sizes $\Delta t = 0.1$ and $\Delta t = 0.3$. The figure shows that GA-23 and GA-234 conserve the total energy in the system far more accurately than GA-2.

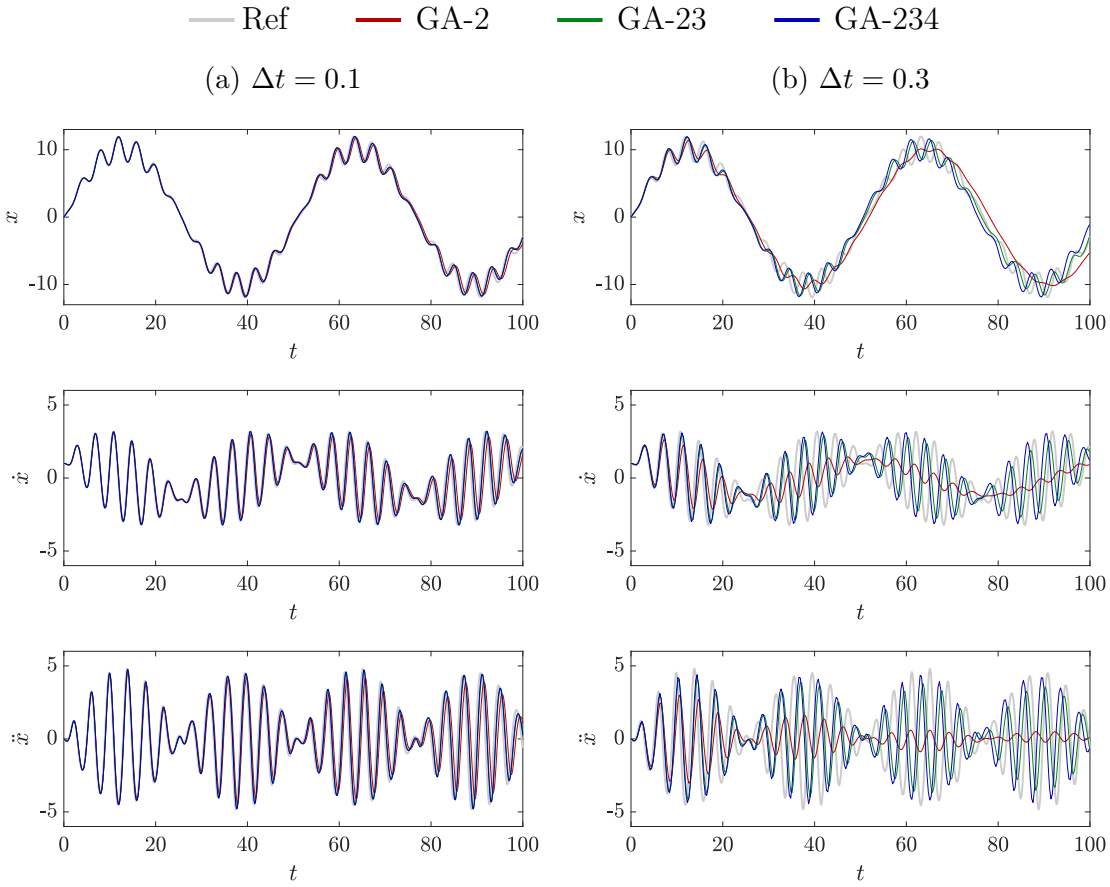

Figure 3.20.: Nonlinear two degree of freedom oscillator; solution obtained in x-direction with $\rho_\infty = 0$.

3.9. Example 5: Wave Propagation on a String

A string of length $L = 20\,\mathrm{m}$, cross-sectional area $A = 2.0 \times 10^{-4}\,\mathrm{m}^2$, density $\rho = 1.14 \times 10^3\,\mathrm{kg/m}^3$, and Young's modulus $E = 2.7$ GPa is considered. It is fixed at one end, while a constant horizontal force of 540 N and a prescribed vertical displacement are applied at the other end. The string is linear elastic,

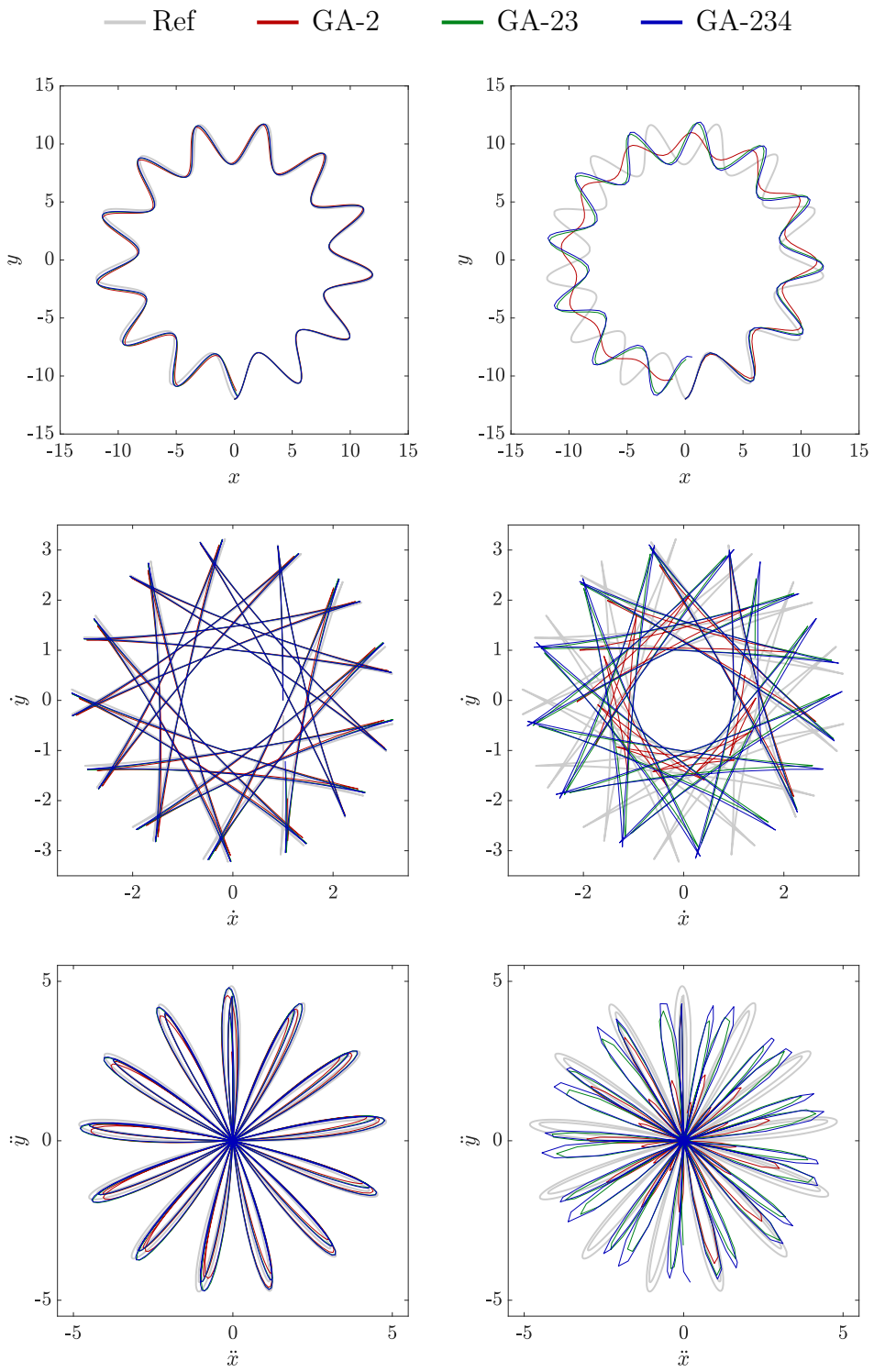

(a) $\Delta t = 0.1$ (b) $\Delta t = 0.3$

Figure 3.21.: Nonlinear two-degree-of-freedom oscillator; displacement, velocity, and acceleration trajectories obtained with $\rho_\infty = 0$.

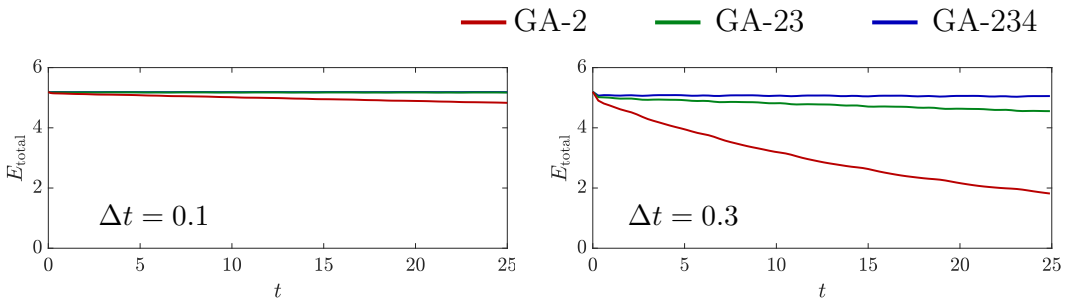

Figure 3.22.: Nonlinear two degree of freedom oscillator; evolution of the total energy over time obtained using $\rho_\infty = 0$.

and the horizontal force causes a strain of 0.1%. The string is represented by 1000 two-noded linear elements using mass lumping. The resolution of the displacements is geometrically exact, and a global Newton-Raphson procedure is employed to obtain the solutions at each time step. The prescribed vertical displacement is

$$d(t) = \frac{D}{2}\left(1 - \cos\left(\frac{2\pi t}{100}\right)\right) \qquad \text{for} \qquad 0 < t < 10 \tag{3.31}$$

where the time must be given in milliseconds. Two values of D are considered, namely, $D = 1\,\text{mm}$ and $D = 1\,\text{m}$, which result in linear and nonlinear responses, respectively.

Figure 3.23 captures snapshots of the string at different times. For the small initial displacement $D = 1$ mm, the wave propagates smoothly along the string, clearly demonstrating typical linear wave motion. The large displacement, $D = 1$ m, results in chaotic and highly nonlinear oscillatory behaviour following the wave reflection at the fixed end.

Figure 3.24 shows the vertical displacement at the midpoint of the string, obtained using GA-2, GA-23, and GA-234 with $\rho_\infty = 0$ and $\Delta t = 4$ ms. A reference solution using GA-234 with a time step of $\Delta t = 0.01$ ms is also provided. The results of the simulations are consistent with previous findings, confirming that GA-23 and GA-234 outperform GA-2 in terms of numerical accuracy and reduced numerical dissipation.

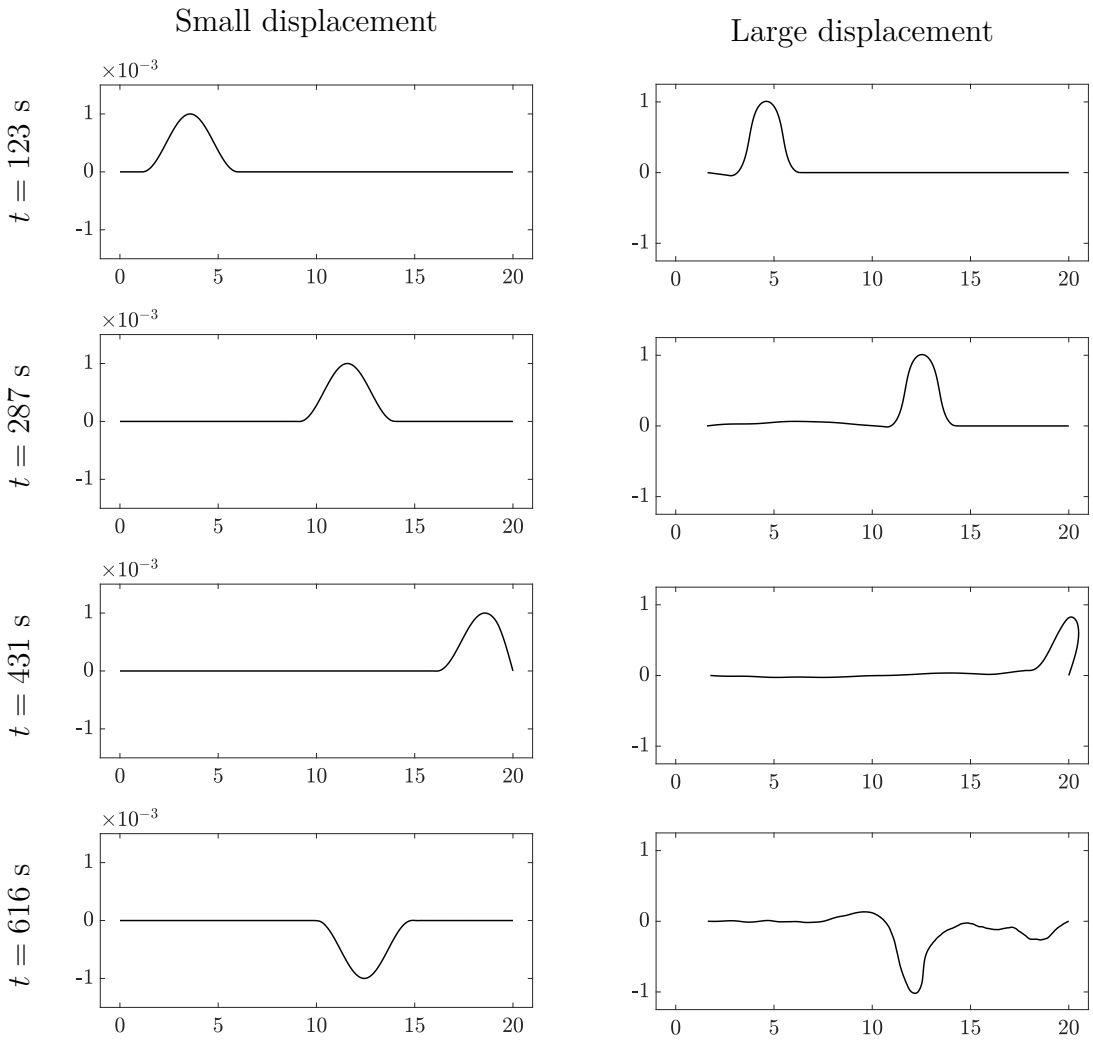

Figure 3.23.: Wave propagation on a string; snapshots of the wave travelling along the string.

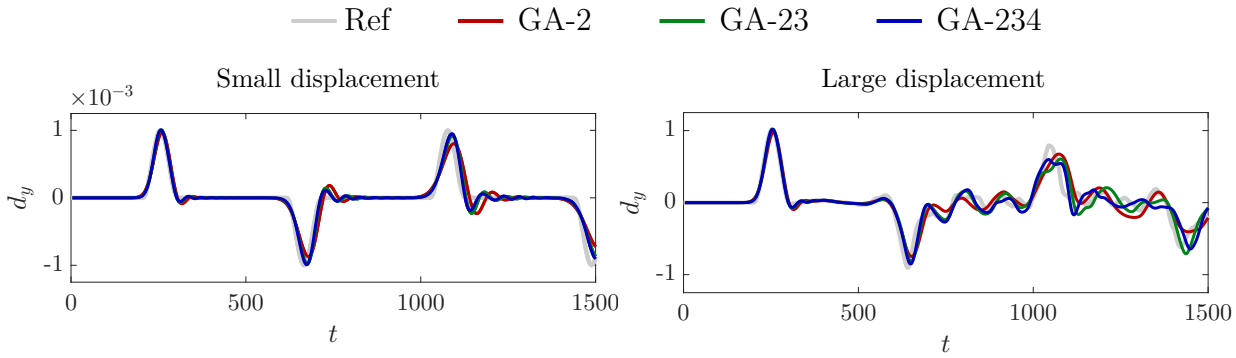

Figure 3.24.: Wave propagation on a string; vertical displacement at the midpoint of the string obtained using $\rho_\infty = 0$ and $\Delta t = 4$ ms.

Chapter 4

Staggered Schemes for Fluid–Structure Interaction

Fluid-structure interaction (FSI) is a complex multiphysics phenomenon observed in various engineering and biomedical fields, including aerospace, biomedical, civil, and energy engineering [45, 46, 81, 110, 111]. Extensive experimental and computational investigations have been carried out to enhance the understanding of FSI problems. However, due to the inherent complexity of FSI, there still remains a need for advanced numerical methods that ensure robust, accurate, and efficient solutions.

4.1. Coupling Strategies

A key aspect of FSI modelling is the coupling strategy, which governs the interaction between the fluid and solid solvers. The two predominant approaches in the literature are the monolithic and partitioned methods.

- **Monolithic Approach:** In the monolithic approach, the governing equations for both fluid and solid domains are combined into a single system and solved simultaneously. This strong coupling ensures accurate interaction between the two domains at each time step, improving numerical stability and accuracy.

However, solving a fully coupled system is computationally demanding, as it involves managing a large set of interdependent equations. Additionally, integrating existing single-physics solvers into a monolithic framework can be challenging. It typically necessitates substantial modifications or the development of entirely new computational frameworks to accommodate the coupled nature of the problem. [11, 35, 55, 67].

- **Partitioned Approach:** The partitioned approach solves the fluid and solid domains separately and enforces interface conditions asynchronously [34]. This approach is widely used due to its flexibility and compatibility with existing, reliable, and optimised computational fluid dynamics and structural mechanics solvers. However, partitioned methods can encounter stability and convergence issues, particularly in problems involving strong fluid-structure coupling [44, 51, 92, 119]. Partitioned approaches are generally classified into two categories

  - **Explicit coupling:** Also known as loosely or weakly coupled schemes, or staggered schemes, this approach executes the fluid and solid solvers once per time step without iteration, making it computationally efficient [47, 51]. However, this method does not fully enforce equilibrium conditions at the fluid-structure interface, leading to potential instability. This instability can arise under certain physical parameter choices, particularly when the fluid and structure densities are comparable or when the domain has a slender shape, irrespective of the chosen time step [24, 51].

  - **Implicit coupling:** Also known as strongly coupled, this approach ensures equilibrium of traction and velocity or displacement at the fluid-structure interface in each time step. This is achieved by iterating between solvers until convergence [65, 112]. While this improves numerical stability and is well-suited for strongly coupled interactions, it is computationally demanding. Additionally, convergence can be slow or even fail, particularly when dealing with an incompressible fluid [18]. To improve convergence in such procedures, adaptive relaxation strategies such as the Aitken acceleration method have been widely adopted, as described in [84].

Remark 4.1.1: Figure 4.1 illustrates the different coupling strategies for solving fluid-structure interaction problems, highlighting their computational structures. *Monolithic coupling* solves the fluid and solid equations as a unified system at each time step, ensuring strong coupling but at a high computational cost. *Partitioned explicit coupling* solves the solid and fluid equations sequentially without iteration, making it computationally efficient but potentially unstable. *Partitioned implicit coupling* iterates between solvers until convergence is achieved, enhancing stability at the expense of increased computational effort.

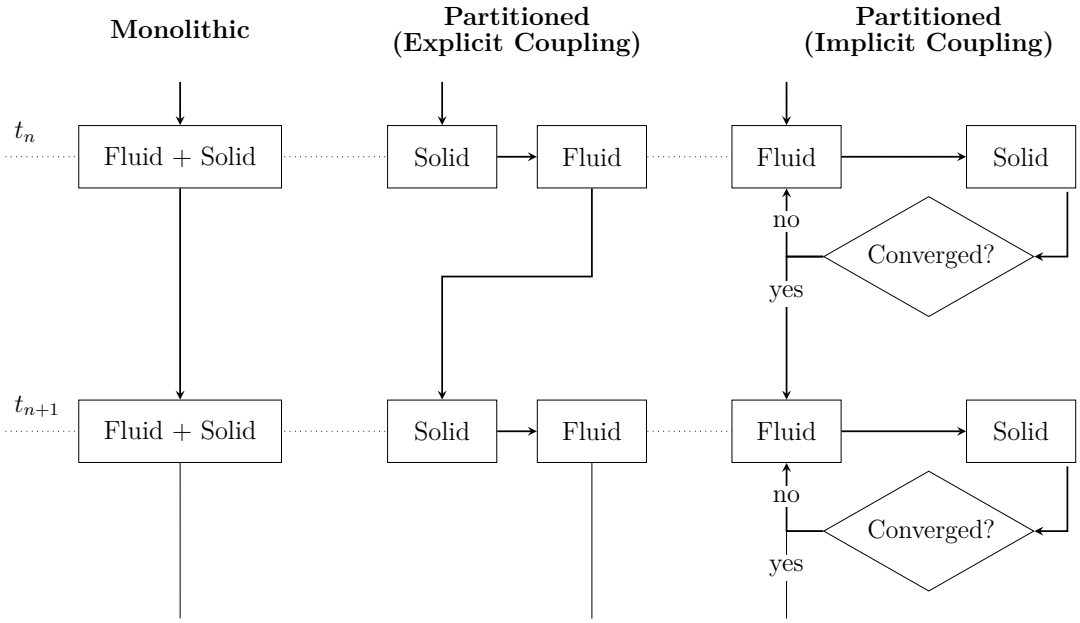

Figure 4.1.: FSI coupling strategies.

4.2. Interface Boundary Conditions

The interaction between the fluid and solid domains must satisfy two coupling conditions: kinematic continuity and traction equilibrium across the interface at all times. Kinematic continuity ensures that velocity and displacement remain equal at the interface, while traction equilibrium ensures a balance of forces between the fluid and solid. These conditions are typically enforced using the following strategies:

- **Dirichlet–Neumann (D–N):** Dirichlet–Neumann coupling is the most traditional and widely implemented approach, known for its straightforward implementation and computational efficiency. In this approach, the structural solver determines the interface displacement, which is then imposed as a Dirichlet boundary condition in the fluid solver. After solving for the fluid dynamics, the fluid solver computes the interface forces and returns them to the structural solver as a Neumann boundary condition [32, 33].

  Dirichlet–Neumann coupling is extensively used in both commercial and open-source software. As discussed in Section 4.1, the partitioned approach allows different solvers to be used for fluid and solid domains, with coupling libraries facilitating their interaction. One of the most widely used open-source libraries for multi-physics simulations is `PreCICE` [19], which natively supports Dirichlet–Neumann coupling as a standard interface condition. Another notable library is `MpCCI` [52], primarily designed for industry-standard fluid-structure interaction applications, where Dirichlet–Neumann coupling is the default approach. Additionally, `CWIPI`, mainly used in aerospace applications, also employs Dirichlet–Neumann coupling as a common interface condition. Note that while Dirichlet–Neumann coupling is standard, these libraries also support alternative strategies.

  Despite its merits, Dirichlet–Neumann coupling (see, for instance, [24, 51, 56, 69]) is well known to suffer from severe instabilities due to the added-mass effect. To address this, [35] introduced a quasi-Newton technique that significantly improves convergence and has been successfully applied to a wide range of problems involving strong added-mass effects. However, the approach remains inherently iterative. In addition, [38] proposed a staggered scheme that improves stability while avoiding the need for iterative coupling procedures.

- **Robin-type interface conditions:** The Robin boundary condition, which is a weighted, linear combination of Dirichlet and Neumann boundary conditions, has been extensively explored in the literature in the context of fluid-structure interaction (see, for instance, [3, 17, 49, 95]).

A notable contribution was made in [4], where a general Robin–Robin algorithm was introduced, generating an entire family of partitioned procedures. This includes the classical Dirichlet–Neumann (D–N) scheme, as well as novel approaches such as Robin–Dirichlet (R–D), Robin–Neumann (R–N), Dirichlet–Robin (D–R), and Neumann–Robin (N–R) coupling methods.

The analysis in [4] shows that among all the investigated methods, the Robin–Neumann algorithm exhibits excellent convergence properties, making it highly appealing. It consistently converges without the need for relaxation and remains unaffected by the added-mass effect. This robustness explains its frequent use in the literature. However, it is noteworthy that its implementation is more complex than the traditional Dirichlet–Neumann approach, as it requires modifications to the fluid solver to properly enforce the Robin boundary condition and careful tuning of the interface weighting parameter.

Other strategies include the Nitsche method [20, 21, 22], though it is not as widely adopted as Robin or Dirichlet–Neumann schemes. This is mainly due to the complexity associated with its implementation and its sensitivity to interface parameter selection.

4.3. Staggered Scheme Framework

The following sections present the formulation and analysis of three staggered schemes based on Dirichlet–Neumann coupling. To evaluate the stability and accuracy of the proposed methods, a linear model problem originally introduced in [24] is employed. These approaches incorporate newly developed time integration schemes. Specifically, the fluid subproblem is advanced using the methods described in Chapter 2, while the solid subproblem is solved using those from Chapter 3. As a result, three distinct schemes are formulated: one based on GA-2, another based on GA-23, and a third employing GA-234.

The staggered scheme framework implemented in this work follows the approach originally proposed in [38]. The process begins by predicting the interface traction force using the history of the previous time step, followed by solving the solid problem. The fluid mesh is then updated accordingly before solving the fluid problem. Once the fluid solution is obtained, the force exerted by the fluid on the solid is computed, and a correction step is applied, updating the force using a weighted average of the predicted and computed values, regulated by a relaxation parameter β. Finally, the time step advances, and the procedure repeats. Figure 4.2 outlines the main steps of the proposed staggered scheme.

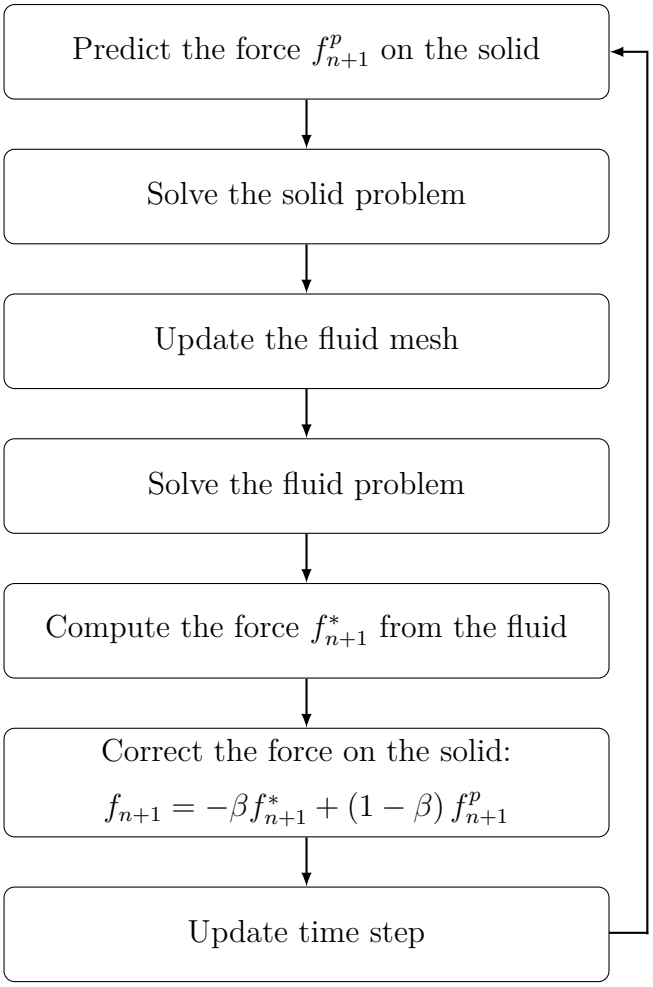

Figure 4.2.: Overview of the staggered scheme steps.

In [38], the first order generalised-α method from [68] was employed for the fluid problem, while the second order generalised-α scheme from [27] was used for the solid problem. A similar approach, following the same steps, was later implemented in [75], where the same scheme was adopted for the fluid problem, and the second order scheme from [73] was applied to the solid problem. Notably, the scheme based on GA-2 is equivalent to that presented in [75], whereas the methods based on GA-23 and GA-234 represent newly developed.

4.4. Model Problem

The simplified fluid-structure interaction model problem introduced in [24] is adopted to assess the performance and analyse the proposed staggered schemes. The problem consists of a thin-walled elastic tube with a circular cross-section containing fluid. The fluid flow is governed by the Navier-Stokes equations, while the tube wall is assumed to be linearly elastic. The radius R, length L, interface Σ, and the fluid and solid domains Ω_F and Ω_S are defined as shown in Figure 4.3.

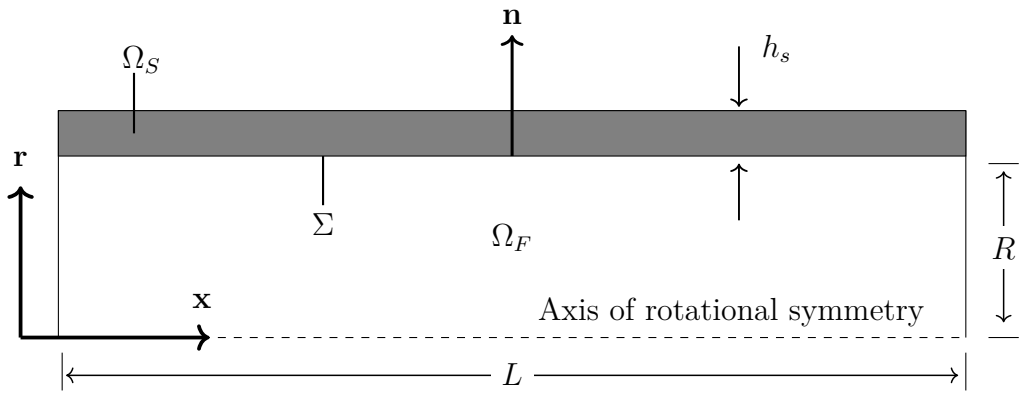

Figure 4.3.: Thin-walled elastic tube.

In accordance with [24], the fluid is assumed to be incompressible and inviscid, with negligible convection effects. Structural displacements are considered small, and the axial stiffness of the tube wall is assumed to be insignificant. Hence, the conservation of momentum and mass for the fluid are given by

$$\left.\begin{aligned} \rho_f\,\dot{\mathbf{u}} + \nabla p = \mathbf{0} \\ \nabla\cdot\mathbf{u} = 0 \end{aligned}\right\} \quad \text{in} \quad \Omega_F \tag{4.1a, 4.1b}$$

where $\mathbf{u}$ is the fluid velocity, p is the pressure, and ρ_f is the fluid density. The radial displacement η of the elastic tube wall is governed by

$$\rho_s\, h_s\, \ddot{\eta} + a\,\eta = f \qquad \text{in} \quad \Omega_S \tag{4.2}$$

where ρ_s is the wall density, h_s is the wall thickness, a represents the stiffness of the wall, and f is the external traction force acting at the interface. The coupling between the fluid and structure at the interface Σ is governed by

$$\left.\begin{aligned} \mathbf{u}\cdot\mathbf{n} = \dot{\eta} \\ f = p \end{aligned}\right\} \quad \text{in} \quad \Sigma \tag{4.3a, 4.3b}$$

where Equation (4.3a) represents the kinematic continuity condition, Equation (4.3b) represents the equilibrium of traction forces, and $\mathbf{n} = \{1, 0\}^T$ is the outward unit normal vector on Σ.

The solution to the coupled problem, governed by Equations (4.1), (4.2), and (4.3), can be expressed as a superposition of fundamental solutions, as presented in [39]

$$\eta = \sum \eta_k, \quad \mathbf{u} = \sum \mathbf{u}_k, \quad p = \sum p_k, \quad f = \sum f_k, \quad k = 1, 2, \ldots \tag{4.4}$$

where the displacement field is given by

$$\eta_k(x,t) = \hat{\eta}_k(t) \sin\left(\frac{\pi k x}{L}\right), \tag{4.5}$$

the velocity field is expressed as

$$\mathbf{u}_k(r,x,t) = \frac{\dot{\hat{\eta}}_k}{I_1\left(\frac{R\pi k}{L}\right)} \begin{cases} \sin\left(\frac{\pi k x}{L}\right) I_1\left(\frac{\pi k r}{L}\right) \\ \cos\left(\frac{\pi k x}{L}\right) I_0\left(\frac{\pi k r}{L}\right) \end{cases}, \tag{4.6}$$

the pressure field is given by

$$p_k(r,x,t) = -\rho_f \frac{L}{\pi k} \ddot{\hat{\eta}}_k \sin\left(\frac{\pi k x}{L}\right) \frac{I_0\left(\frac{\pi k r}{L}\right)}{I_1\left(\frac{\pi k R}{L}\right)}, \tag{4.7}$$

the traction force at the interface is defined as

$$f_k(x,t) = -\rho_f \frac{L}{\pi k} \ddot{\hat{\eta}}_k \sin\left(\frac{\pi k x}{L}\right) \frac{I_0\left(\frac{\pi k R}{L}\right)}{I_1\left(\frac{\pi k R}{L}\right)}. \tag{4.8}$$

The modified Bessel functions $I_0(\bullet)$ and $I_1(\bullet)$ are expressed as

$$I_n(z) = \sum_{m=0}^{\infty} \frac{1}{m!(m+n)!} \left(\frac{z}{2}\right)^{2m+n}. \tag{4.9}$$

Using Equations (4.4) to (4.8) and defining

$$\mu_k := \frac{L}{\pi k} \frac{I_0\left(\frac{\pi k R}{L}\right)}{I_1\left(\frac{\pi k R}{L}\right)} \tag{4.10}$$

the problem described by Equations (4.1) to (4.3) reduces to a set of differential equations governing the scalar amplitudes of the wall displacement $\hat{\eta}_k$

$$\rho_s\, h_s\, \ddot{\hat{\eta}}_k + a\, \hat{\eta}_k = \hat{f}_k, \tag{4.11}$$

$$\rho_f\, \mu_k\, \ddot{\hat{\eta}}_k = -\hat{f}_k. \tag{4.12}$$

By defining

$$\alpha := \frac{\rho_s h_s}{\rho_s h_s + \rho_f \mu_k}, \quad \omega := \sqrt{\frac{a}{\rho_s h_s + \rho_f \mu_k}}, \quad d := \hat{\eta}_k, \quad f := \frac{\hat{f}_k}{\rho_s h_s + \rho_f \mu_k}.$$

Equations (4.11) and (4.12) are reformulated as

$$\alpha\, \ddot{d} + \omega^2\, d = f, \tag{4.13}$$

$$(1-\alpha)\, \ddot{d} = -f. \tag{4.14}$$

Introducing a viscous term with a damping coefficient ξ in Equation (4.14) renders

$$\alpha\,\ddot{d} + \omega^2\,d = f \qquad \text{(solid)} \tag{4.15}$$

$$(1-\alpha)\,\ddot{d} + 2\,\xi\,\omega\,\dot{d} \;= -f \qquad \text{(fluid)} \tag{4.16}$$

This formulation represents a system consisting of an elastic spring, a dashpot, and two point masses, as illustrated in Figure 4.4. It also recovers the model problem used by [38].

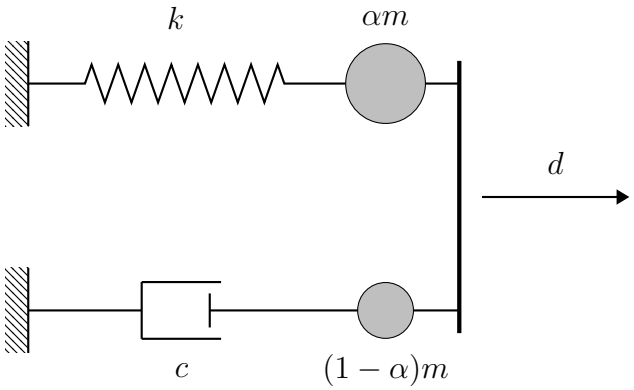

Figure 4.4.: One-dimensional linear model problem.

The parameter α represents the ratio of solid mass to total mass, including added fluid mass, and is bounded between 0 and 1.

- A strong added mass effect is associated with values of α close to 0.
- A small added mass effect is associated with values of α close to 1.

Many applications, including the modelling of components of the vascular system, are associated with very small values of α.

By discretising Equations (4.15) and (4.16) using the time integration schemes presented in Chapters 2 and 3, the following formulation is derived

$$\alpha\,\dot{v}_{n+\beta} \;+\; \omega^2\,d_{n+\alpha} \;=\; f_{n+\alpha} \tag{4.17}$$

$$(1-\alpha)\,\dot{v}_{n+\beta} \;+\; 2\,\xi\,\omega\,v_{n+\alpha} \;=\; -f_{n+\alpha} \tag{4.18}$$

4.5. Single-Cycle Schemes

To ensure that the staggered schemes maintain second order accuracy and remain unconditionally stable up to a critical added-mass limit, the traction force predictor must not exceed the second order predictor given by

$$f_{n+1}^{p} = 2f_n - f_{n-1}. \tag{4.19}$$

Using higher order predictors can improve the accuracy of the staggered scheme. However, their stability limits become significantly more restrictive [75]. A linear combination of the second order predictor and higher order predictors can provide an enhanced second order predictor with improved accuracy.

Following the same methodology used in the development of GA-23 and GA-234 in Chapter 2, the following linear combination is considered

$$f_{n+1}^{p} \;=\; \delta_3\, f_{n+1}^{(3)} \;+\; (1-\delta_3)\, f_{n+1}^{(2)}, \tag{4.20}$$

where $f_{n+1}^{(3)} = 3f_n - 3f_{n-1} + f_{n-2}$ is the third order predictor, and $f_{n+1}^{(2)}$ is the second order predictor given in Equation (4.19).

Using Jury stability analysis, the largest possible δ_3 is

$$\delta_3 = \frac{(1-\rho_\infty)^2}{2(1-\rho_\infty+\rho_\infty^2)}, \tag{4.21}$$

where ρ_∞ is a user-defined parameter in the time integration scheme that represents the spectral radius at an infinitely large time step and governs numerical damping. In the following analysis, ρ_∞ is set to zero, which leads to $\delta_3 = \frac{1}{2}$, resulting in

$$f_{n+1}^{p} = \frac{5}{2}\, f_n - 2\, f_{n-1} + \frac{1}{2}\, f_{n-2}. \tag{4.22}$$

A linear combination of the second, third, and fourth order predictors can also be formulated as

$$f_{n+1}^{p} = \delta_4\, f_{n+1}^{(4)} + (1-\delta_4)\, \left(\delta_3\, f_{n+1}^{(3)} + (1-\delta_3)\, f_{n+1}^{(2)}\right), \tag{4.23}$$

where the fourth order predictor is given by $f_{n+1}^{(4)} = 4f_n - 6f_{n-1} + 4f_{n-2} - f_{n-3}$. Using Jury stability analysis, the largest possible δ_4 is obtained as

$$\delta_4 = \frac{(1-\rho_\infty)^2}{5(1+\rho_\infty^2)}. \tag{4.24}$$

For $\rho_\infty = 0$, $\delta_4 = \frac{1}{5}$, resulting in

$$f_{n+1}^p \;=\; \frac{14}{5}\, f_n - \frac{14}{5}\, f_{n-1} + \frac{6}{5}\, f_{n-2} - \frac{1}{5}\, f_{n-3}. \tag{4.25}$$

The second order predictor given in Equation (4.19) will be used for the method based on GA-2. The predictor in Equation (4.22) will be used in schemes based on GA-23, and the predictor in Equation (4.25) will be used in the method based on GA-234.

Setting $\rho_\infty = 0$ in the equation sets from Boxes 3 and 9, and substituting them into Equations (4.17) and (4.18) for GA-2, yields

$$d_{n+1} = \frac{4\,\Delta t^2\, f_{n+1}^p + 9\,\alpha\, d_n + 3\,\alpha\,\Delta t\,\dot{d}_n + 6\,\alpha\,\Delta t\, v_n + 2\,\alpha\,\Delta t^2\,\dot{v}_n}{4\Delta t^2\omega^2 + 9\alpha}, \tag{4.26}$$

$$f_{n+1} = -\left((1-\alpha)\left(\frac{3}{2}\dot{v}_{n+1} + \frac{1}{2}\dot{v}_n\right) - \omega\xi v_{n+1}\right). \tag{4.27}$$

Equation (4.26) represents the *solid solver*, which is formulated in terms of the variables $(f_{n+1}^p, d_n, \dot{d}_n, v_n, \dot{v}_n)$. Similarly, Equation (4.27) defines the *fluid solver*, which is expressed using the variables $(v_{n+1}, \dot{v}_{n+1}, \ddot{v}_n)$.

A similar procedure can be applied to GA-23 and GA-234 but is omitted for brevity. Boxes 14 to 16 provide a summary of the staggered schemes for GA-2, GA-23, and GA-234 with $\rho_\infty = 0$ in the context of the model problem. Each box presents the predictor expressions, details the execution steps of the solid and fluid solvers, and outlines the auxiliary terms required for each scheme.

The system of equations presented in Boxes 14 to 16 can be expressed in matrix form as

$$\mathbf{X}_{n+1} \;=\; \mathbf{A}_{\text{stag}}\, \mathbf{X}_n, \tag{4.28}$$

1. set traction force predictor	$f^p_{n+1} = 2\,f_n - f_{n-1}$
2. execute solid solver	$d_{n+1} = \text{solid}(f^p_{n+1}, d_n, \dot{d}_n, v_n, \dot{v}_n)$
	$\dot{d}_{n+1} = \frac{1}{\Delta t}\,(d_{n+1} - d_n)$
	$v_{n+1} = \frac{3}{2}\,\dot{d}_{n+1} - \frac{1}{2}\,\dot{d}_n$
	$\dot{v}_{n+1} = \frac{1}{\Delta t}\,(v_{n+1} - v_n)$
3. execute fluid solver	$f^*_{n+1} = \text{fluid}(v_{n+1}, \dot{v}_{n+1}, \dot{v}_n)$
4. compute traction force	$f_{n+1} = (1 - \beta)\,f^p_{n+1} + \beta\,f^*_{n+1}$
5. proceed to next time step	$n \leftarrow n+1$

Box 14: Summary of the staggered scheme formulated using GA-2 with $\rho_\infty = 0$.

1. set traction force predictor	$f^p_{n+1} = \frac{5}{2}\,f_n - 2f_{n-1} + \frac{1}{2}\,f_{n-2}$
2. execute solid solver	$d_{n+1} = \text{solid}(f^p_{n+1}, d_n, \dot{d}_n, \ddot{d}_n, v_n, \dot{v}_n, \ddot{v}_n)$
	$d^{(i+1)'}_{n+1} = \frac{1}{\Delta t}\,(d^{(i)'}_{n+1} - d^{(i)'}_n) \quad \text{for } i = 0, 1$
	$v_{n+1} = \frac{5}{3}\,\dot{d}_{n+1} - \frac{2}{3}\,\dot{d}_n - \frac{1}{6}\,\ddot{d}_n\,\Delta t$
	$v^{(i+1)'}_{n+1} = \frac{1}{\Delta t}\,(v^{(i)'}_{n+1} - v^{(i)'}_n) \quad \text{for } i = 0, 1$
3. execute fluid solver	$f^*_{n+1} = \text{fluid}(v_{n+1}, \dot{v}_{n+1}, \dot{v}_n, \ddot{v}_n)$
4. compute traction force	$f_{n+1} = (1 - \beta)\,f^p_{n+1} + \beta\,f^*_{n+1}$
5. proceed to next time step	$n \leftarrow n+1$

Box 15: Summary of the staggered scheme formulated using GA-23 with $\rho_\infty = 0$.

1. set traction force predictor	$f^p_{n+1} = \frac{14}{5} f_n - \frac{14}{5} f_{n-1} + \frac{6}{5} f_{n-2} - \frac{1}{5} f_{n-3}$
2. execute solid solver	$d_{n+1} = \text{solid}(f^p_{n+1}, d_n, \dot{d}_n, \ddot{d}_n, \dddot{d}_n, v_n, \dot{v}_n, \ddot{v}_n, \dddot{v}_n)$
	$d^{(i+1)'}_{n+1} = \frac{1}{\Delta t}(d^{(i)'}_{n+1} - d^{(i)'}_n) \quad \text{for } i = 0, 1, 2$
	$v_{n+1} = \frac{7}{4}\dot{d}_{n+1} - \frac{3}{4}\dot{d}_n - \frac{1}{4}\ddot{d}_n \Delta t - \frac{1}{20}\dddot{d}_n \Delta t^2$
	$v^{(i+1)'}_{n+1} = \frac{1}{\Delta t}(v^{(i)'}_{n+1} - v^{(i)'}_n) \quad \text{for } i = 0, 1, 2$
3. execute fluid solver	$f^*_{n+1} = \text{fluid}(v_{n+1}, \dot{v}_{n+1}, \dot{v}_n, \ddot{v}_n, \dddot{v}_n)$
4. compute traction force	$f_{n+1} = (1 - \beta) f^p_{n+1} + \beta f^*_{n+1}$
5. proceed to next time step	$n \leftarrow n + 1$

Box 16: Summary of the staggered scheme formulated using GA-234 with $\rho_\infty = 0$.

where $\mathbf{A}_{\text{stag}}$ denotes the amplification matrix associated with each scheme. The amplification matrix for the GA-2 scheme with $\xi = 0$ is given in Equation (4.29). The matrices for GA-23 and GA-234 are considerably larger and are therefore omitted, although they can be derived easily using symbolic mathematics software. The coefficients of these matrices depend on the parameters Δt, ω, and ξ, which govern the temporal and dynamic behaviour of the system.

$$\mathbf{A}_{\text{stag}} = \frac{1}{e}\begin{bmatrix} 9\alpha & 3\alpha & 6\alpha & 2\alpha & 8 & -4 \\ -4\,\Delta t^2\,\omega^2 & 3\alpha & 6\alpha & 2\alpha & 8 & -4 \\ -6\,\Delta t^2\,\omega^2 & -2\,\Delta t^2\,\omega^2 & 9\alpha & 3\alpha & 12 & -6 \\ -6\,\Delta t^2\,\omega^2 & -2\,\Delta t^2\,\omega^2 & -4\,\Delta t^2\,\omega^2 & 3\alpha & 12 & -6 \\ -9z & -3z & -6z & -2z & 2x & -x \\ 0 & 0 & 0 & 0 & 1 & 0 \end{bmatrix} \tag{4.29}$$

where $e = 4\,\Delta t^2\,\omega^2 + 9\alpha$, $z = \beta\,\Delta t^2\,\omega^2\,(\alpha - 1)$, and $x = 9(\alpha - \beta) + 4\,\Delta t^2\,\omega^2\,(1 - \beta)$. It should be noted that, in this chapter, the parameter α represents the added-mass effect, and β serves as the relaxation factor; these are not the time-integration parameters introduced in Chapters 2 and 3.

4.6. Stability Analysis

For stability in the time domain, the spectral radius $\rho(\mathbf{A}_{\text{stag}})$, defined as $\rho(\mathbf{A}_{\text{stag}}) = \max(|\lambda_1|, |\lambda_2|, \cdots, |\lambda_i|)$, where λ_i are the eigenvalues of the amplification matrix, must not exceed one. To investigate the performance of the scheme, it is convenient to consider the spectral radius in the limiting cases of small ($\Delta t \to 0$) and large ($\Delta t \to \infty$) time steps.

For GA-2

$$\lim_{\Delta t \to 0} \rho(\mathbf{A}_{\text{stag}}) = \max\left(\frac{1}{3},\, 1,\, \left|\frac{\alpha - \beta - \sqrt{\beta}\sqrt{\beta - \alpha}}{\alpha}\right|\right), \tag{4.30}$$

$$\lim_{\Delta t \to \infty} \rho(\mathbf{A}_{\text{stag}}) = \max\left(0, \sqrt{1 - \beta}\right). \tag{4.31}$$

Equation (4.30) states that for the scheme based on GA-2 to be unconditionally stable, β must satisfy the following condition

$$0 \leq \beta \leq \frac{4\alpha}{3}. \tag{4.32}$$

which indicates that smaller β values are needed for smaller α. The expression for numerical damping is derived from Equation (4.31) and shows that as β decreases, the spectral radius approaches one. The same limit case evaluations have been conducted for the staggered schemes based on GA-23 and GA-234. However, the expressions are lengthy and omitted for brevity. The critical conditions for β are obtained as

$$\text{For GA-23:} \qquad 0 \leq \beta \leq \frac{6\alpha}{5}, \tag{4.33}$$

$$\text{For GA-234:} \qquad 0 \leq \beta \leq \frac{8\alpha}{7}. \tag{4.34}$$

The expression for $\lim_{\Delta t \to \infty}$, which characterises the numerical damping behaviour of the schemes based on GA-23 and GA-234, is excessively complex to derive analytically. However, the results presented in the following section demonstrate that it exhibits a similar trend to GA-2.

4.7. Multi-Cycle Schemes

Section 4.5 introduced a conventional staggered scheme in which the solid and fluid solvers are executed once per time step. While this approach is computationally efficient, its accuracy can be limited. To improve accuracy without sacrificing efficiency, a non-iterative n-cycle variant of the three staggered schemes based on GA-2, GA-23, and GA-234 is proposed. In this formulation, a predefined number of computational cycles is performed within each time step. Unlike classical iterative methods that require an unpredictable and often large number of iterations to reach convergence, the n-cycle approach retains efficiency by using a fixed number of updates. This controlled cycling not only enhances solution accuracy but also significantly reduces computational cost compared to fully iterative schemes.

The stability analysis presented in Section 4.6 has been carried out for the n-cycle schemes. However, the resulting expressions are highly complex and not suitable for direct analytical evaluation. Therefore, the stability criteria were assessed through numerical experiments. These investigations indicate that, for $n > 1$, the critical value of the relaxation parameter β in all three schemes based on GA-2, GA-23, and GA-234 deviates from the expressions given in Equations (4.32), (4.33), and (4.34), and instead tends toward $\beta \approx \alpha$. Therefore, in the following analysis, the critical value of β is set as $\beta = \alpha$ for $n > 1$, whereas for $n = 1$, the expressions derived in Equations (4.32), (4.33), and (4.34) are used.

Figure 4.5 shows the spectral radius of the amplification matrix for the three staggered schemes as a function of Δt, evaluated for various values of n and α. As the number of computational cycles increases, the spectral radius

generally decreases, indicating enhanced damping characteristics. However, in the presence of a strong added-mass effect ($\alpha \to 0$), the spectral radius remains close to 1, reflecting weak damping.

Figure 4.6 presents the response of the model problem obtained using the three staggered schemes with different computational cycles for $\Delta t = 0.1$ and various values of α, alongside the exact solution. The exact solution can be expressed in compact form as

$$\mathbf{u}_{n+1} = \exp\left(\mathbf{M}\,\Delta t\right)\mathbf{u}_n\,, \quad \text{with} \quad \mathbf{u}_n = \begin{bmatrix} d_n \\ \dot{d}_n \end{bmatrix}, \quad \mathbf{M} = \begin{bmatrix} 0 & 1 \\ -\omega^2 & -2\xi\omega \end{bmatrix}. \tag{4.35}$$

Figure 4.6 shows that for $n = 1$, significant phase and amplitude discrepancies are observed between the staggered methods and the exact solution, particularly for smaller α, where the added-mass effect is more pronounced. This effect is most evident in GA-2, while GA-23 and GA-234 exhibit smaller discrepancies. As n increases, the discrepancies diminish, leading to a closer agreement with the exact solution. For larger α, the influence of the added-mass effect is less significant, resulting in improved agreement with the exact solution even for $n = 1$. For this case, five computational cycles ($n = 5$) appear to be sufficient to achieve satisfactory accuracy, as further increasing n to 10 yields only marginal improvements. This suggests that beyond a certain point, increasing n provides minimal accuracy improvement, making excessively large values unnecessary.

Figures 4.7 to 4.10 illustrate the convergence of the staggered solutions based on GA-2, GA-23, and GA-234 for different values of α and various computational cycles n. A monolithic approach using GA-2, GA-23, and GA-234 is also included. Since the monolithic solution remains unaffected by added-mass effects, it serves as a reference for assessing accuracy. The error ε is calculated by comparing the exact displacement $\tilde{d}$ with the numerical displacement $\bar{d}$ obtained from each method

$$\varepsilon(t_N) = \sqrt{\frac{t_N}{N}\sum_{i=1}^{N}\left|\tilde{d}(t_i) - \bar{d}(t_i)\right|^2}, \tag{4.36}$$

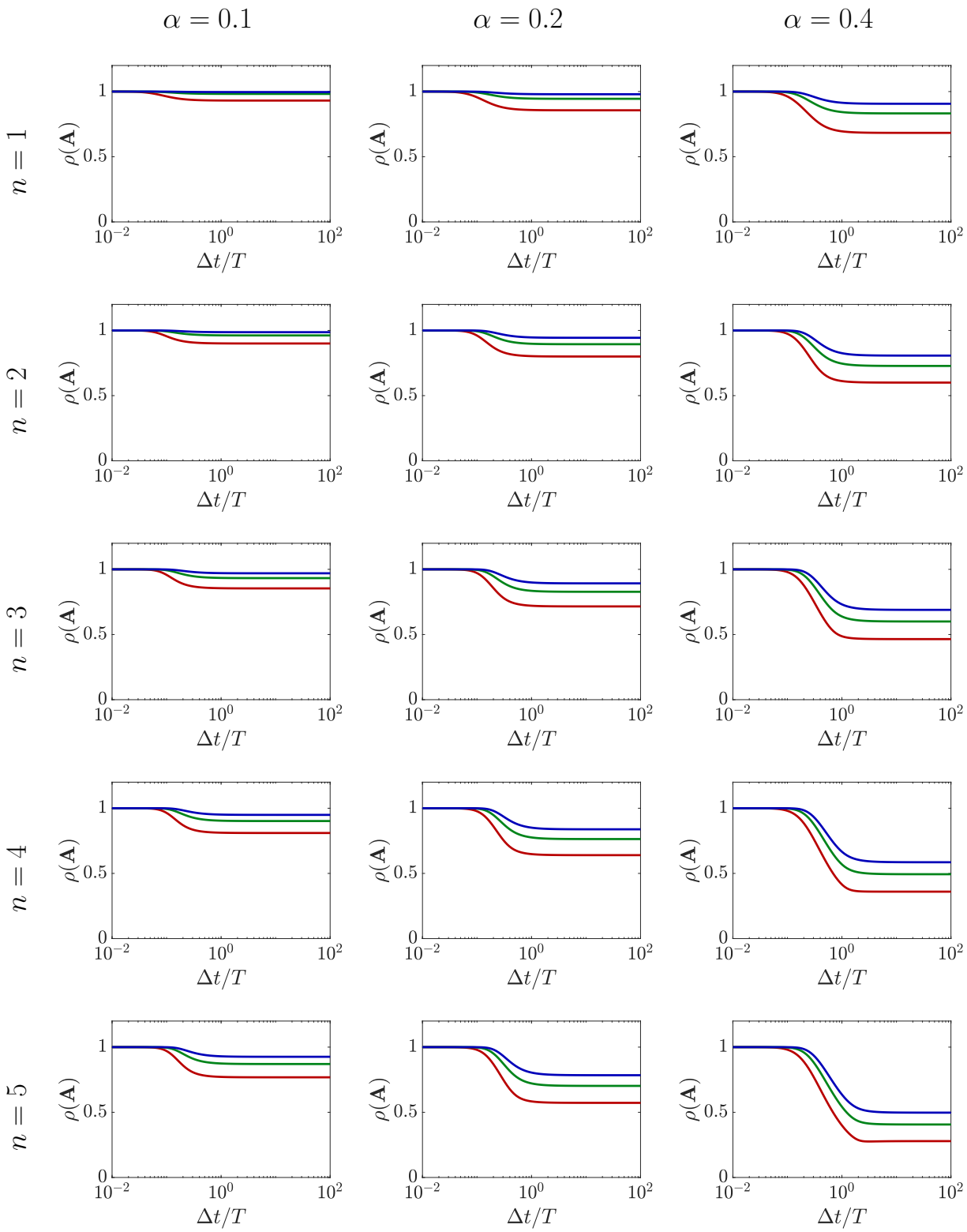

Figure 4.5.: Model problem; spectral radii of the three proposed staggered schemes based on GA-2 (red), GA-23 (green), and GA-234 (blue) for different computational cycles.

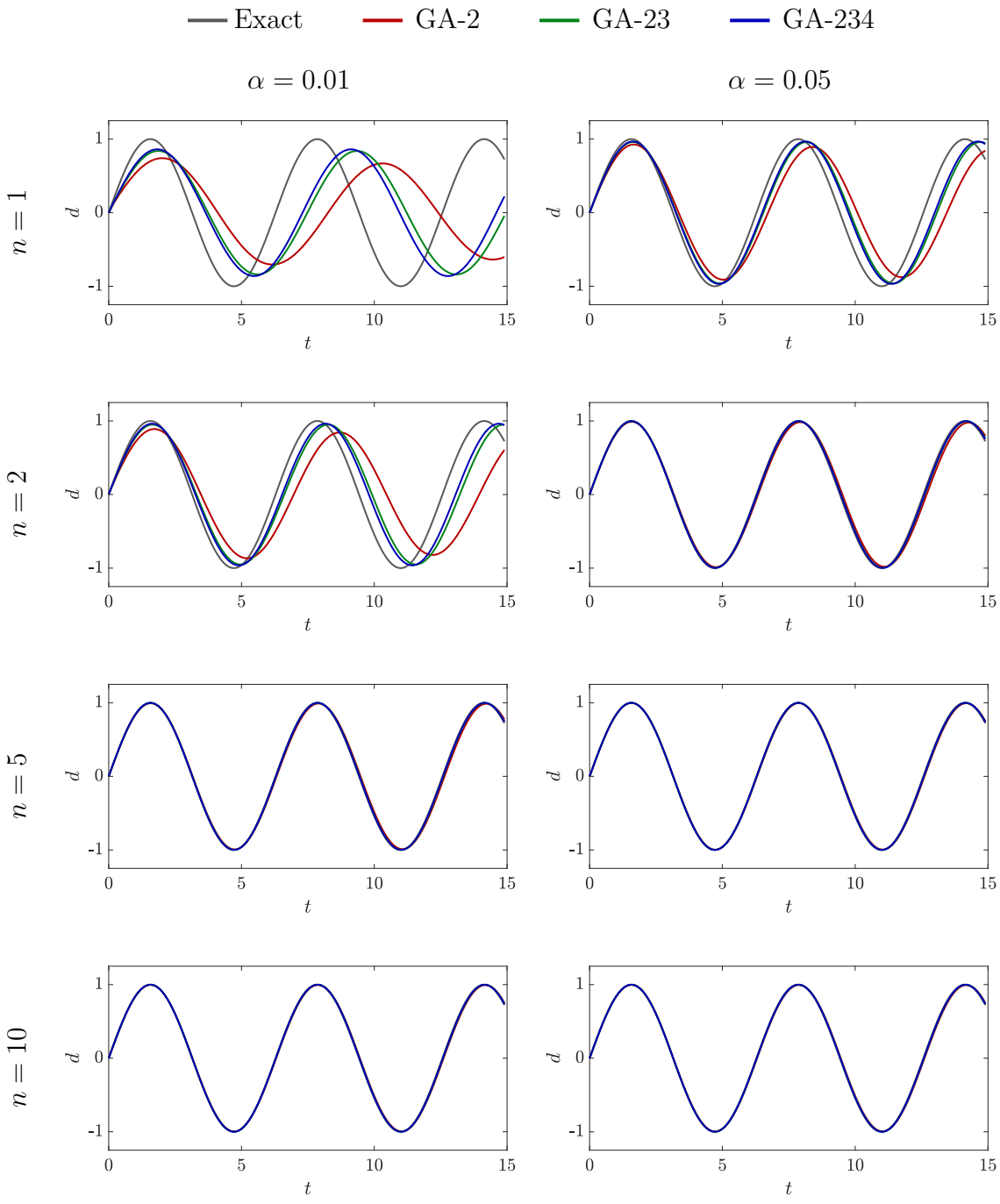

Figure 4.6.: Model problem; displacement response obtained with $\Delta t = 0.1$.

where N denotes the total number of time steps in the computation.

The following observations are made from Figures 4.7 to 4.11:

- For small values of α, the discrepancy between the monolithic and staggered schemes is more pronounced, particularly in the staggered schemes with fewer computational cycles.
- As α increases, the influence of the added-mass effect diminishes, leading to improved accuracy of the staggered schemes and reducing the gap between the monolithic and staggered solutions.
- Increasing the number of computational cycles enhances the accuracy of the staggered schemes, as additional iterations improve the coupling consistency between the structural and fluid fields.
- Among the staggered approaches, the scheme based on GA-234 exhibits a substantial reduction in numerical errors compared with GA-2.

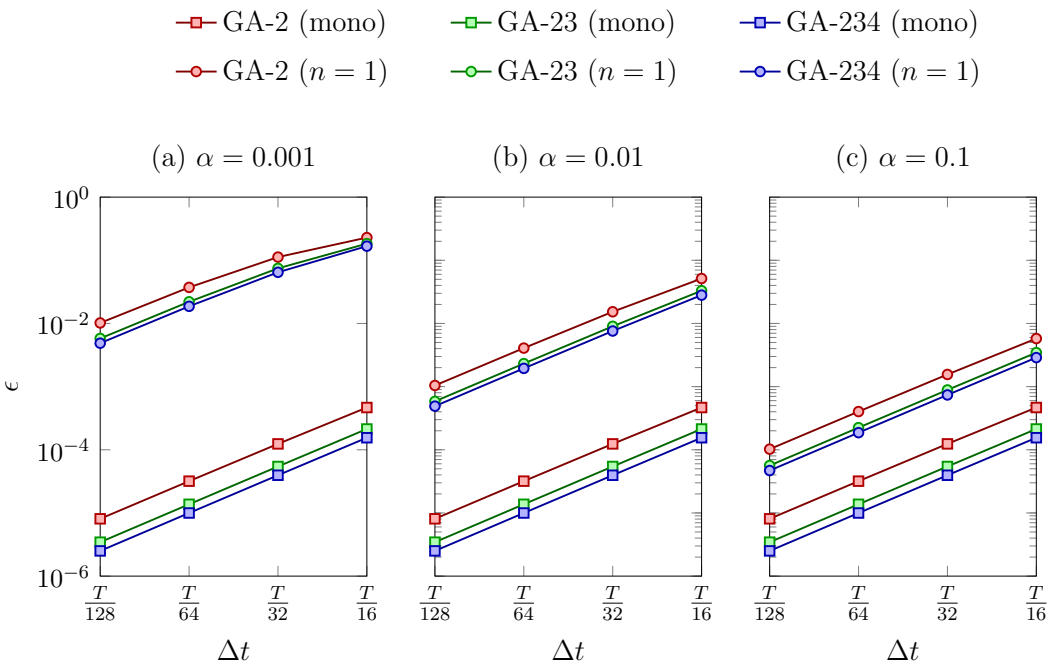

Figure 4.7.: Model problem; convergence rates obtained using the monolithic solution and the staggered schemes with $n = 1$.

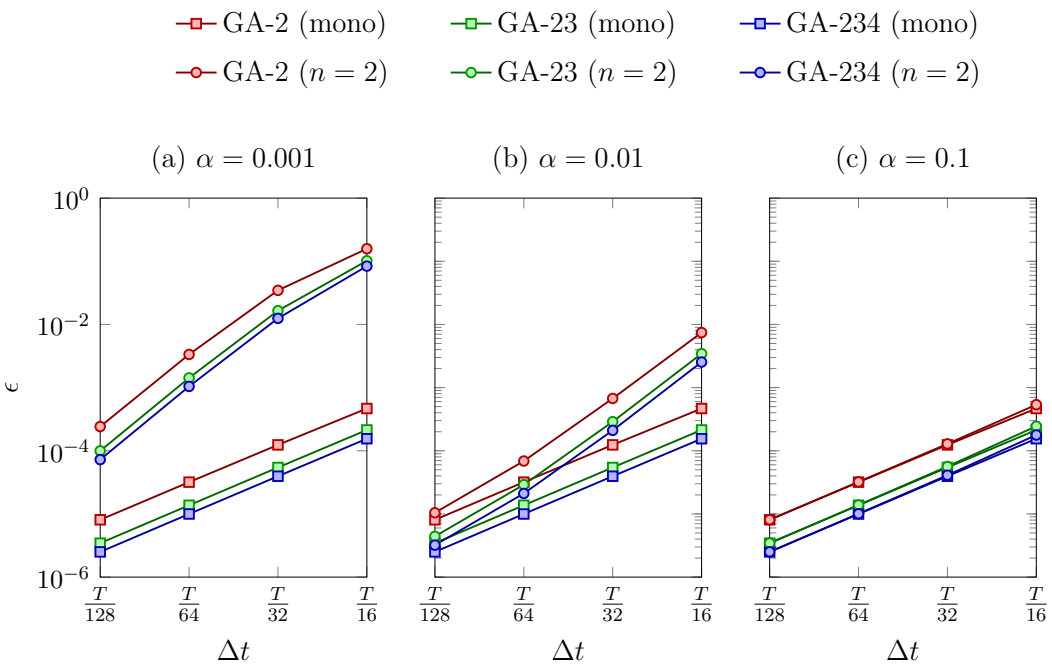

Figure 4.8.: Model problem; convergence rates obtained using the monolithic solution and the staggered schemes with $n = 2$.

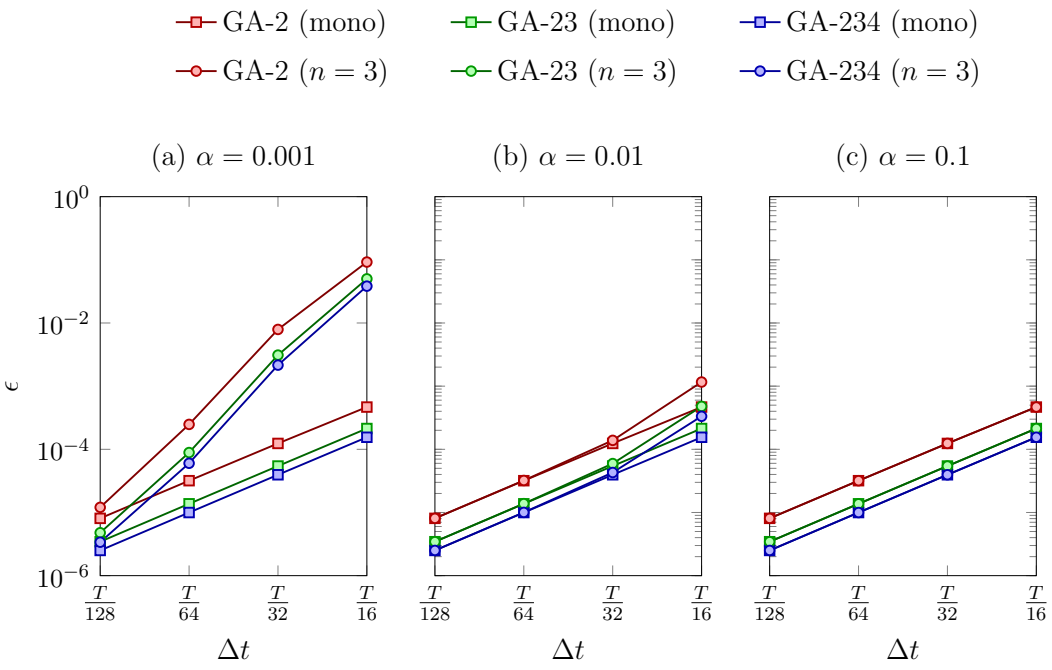

Figure 4.9.: Model problem; convergence rates obtained using the monolithic solution and the staggered schemes with $n = 3$.

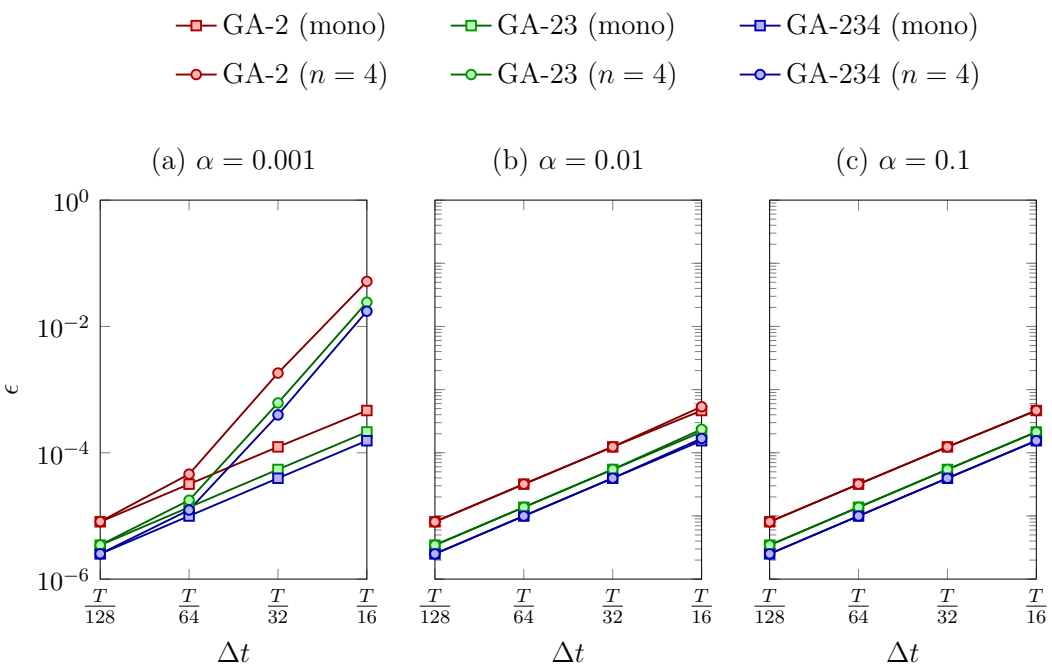

Figure 4.10.: Model problem; convergence rates obtained using the monolithic solution and the staggered schemes with $n = 4$.

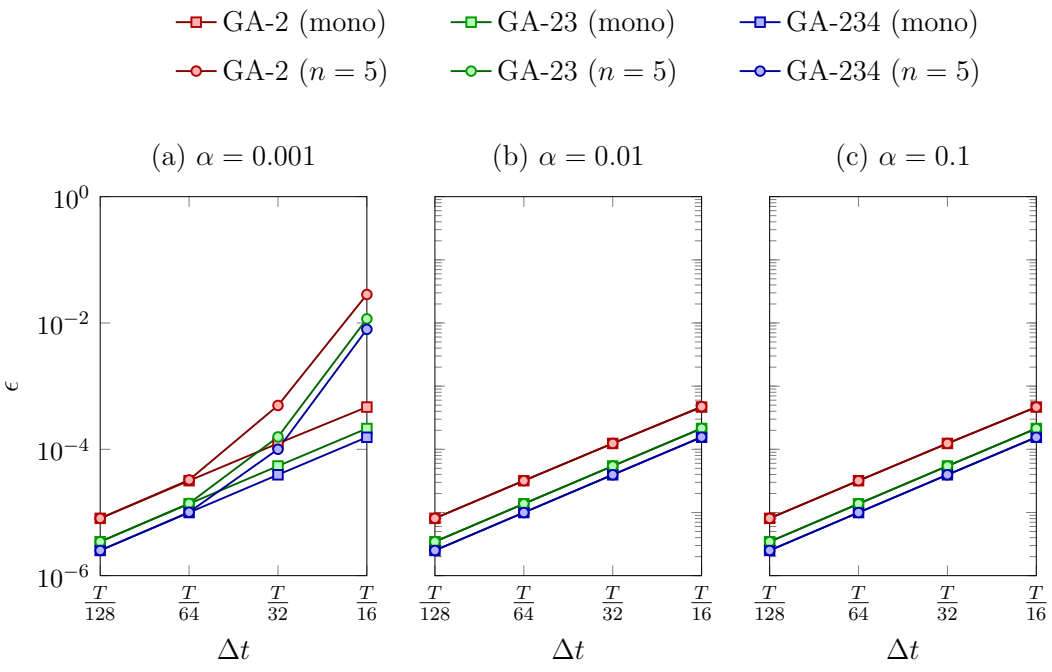

Figure 4.11.: Model problem; convergence rates obtained using the monolithic solution and the staggered schemes with $n = 5$.

Chapter 5

Numerical Examples for Fluid-Structure Interaction

This chapter evaluates the proposed staggered scheme strategies, introduced in Chapter 4, by applying them to a range of numerical examples in fluid–structure interaction to assess their accuracy, stability, and efficiency. The examples include flow around a flexibly supported rigid cylinder, flow-induced vibrations of a flexible beam, and flow through a flexible tube.

5.1. Example 1: Flow Around a Flexibly Supported Rigid Cylinder

This section validates the model problem analysis presented in Sections 4.4 and 4.5 by applying it to a two-dimensional fluid–structure interaction system. The system consists of a rigid cylinder submerged in a square domain and attached to a spring. The fluid is incompressible, with a density of $\rho_f = 1\,\mathrm{kg/m^3}$ and a dynamic viscosity of $\mu_f = 0.01$ Pa s. The cylinder has a diameter of $d = 1$ m and is mounted on a spring with a stiffness of $k = 15$ N/m. It is subjected to an inflow velocity u_{in} that gradually increases to a maximum of $u_{\max} = 1.4334$ m/s before decreasing smoothly back to zero. At peak inflow, the Reynolds number is approximately $\mathrm{Re} = 143.34$.

The fluid domain is discretised using linear triangular elements within a stabilised finite element framework for incompressible flow. The formulation includes SUPG and PSPG stabilisation. The geometry and boundary conditions are illustrated in Figure 5.1. The employed mesh, shown in Figure 5.2, consists of 6,205 nodes, 12,258 elements, and 18,412 degrees of freedom.

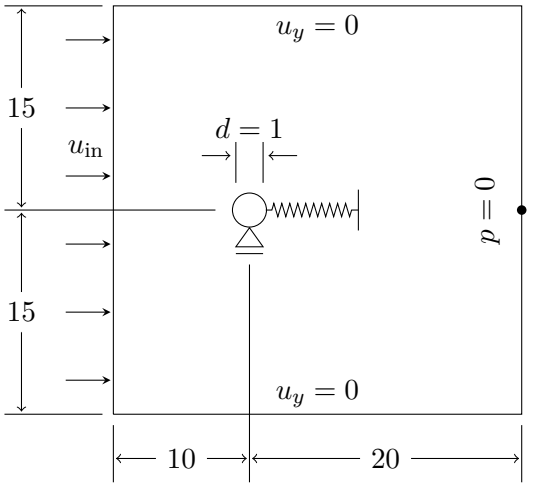

Figure 5.1.: Flow around flexibly supported rigid cylinder; geometry and boundary conditions.

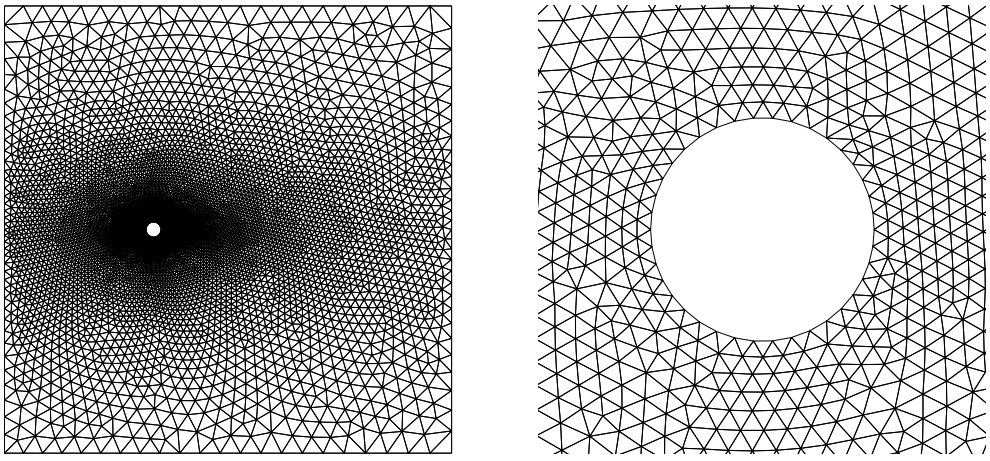

(a) (b)

Figure 5.2.: Flow around flexibly supported rigid cylinder; finite element mesh (a), mesh refinement around the cylinder (b).

For such problems, it is well-known that the added fluid mass is equivalent to the mass of the displaced fluid [15, 39]. Assuming the system can be modeled by a single mode, a representative value for the parameter α is obtained as

$$\alpha = \frac{\rho_s}{\rho_s + \rho_f}. \tag{5.1}$$

Different values of α are investigated by changing the solid density ρ_s.

To determine the critical values for the relaxation parameter β, simulations were conducted for various combinations of α and β. Simulations are considered stable if no spurious oscillations occur within the time domain $0 < t \leq 12$. The largest values of β that result in stable simulations for different values of α, obtained with $\Delta t = 0.1$, are shown in Figure 5.3. A sufficient number of simulations were performed to accurately determine the first two significant digits of the critical relaxation parameter. It can be observed that for all three staggered schemes based on GA-2, GA-23, and GA-234, with computational cycles $n = 1$ and $n = 2$, the largest obtained values align well with the analytical expressions derived from the model problem analysis, confirming both the relevance of the model problem and the validity of the analysis.

The diagrams in Figures 5.4, 5.5, and 5.6 illustrate the evolution of the interface traction force and cylinder velocity for the three staggered schemes with computational cycles $n = 1$ and $n = 2$ for $\alpha = 0.05$, obtained using time steps $\Delta t = 0.01$, $\Delta t = 0.05$, and $\Delta t = 0.1$. The figures also include reference solutions obtained using the iterative method, where each reference solution is based on the same time integration scheme as the corresponding staggered solution.

For $\Delta t = 0.01$, all staggered schemes accurately recover the reference solution. For $\Delta t = 0.05$ and $n = 1$, all staggered solutions closely follow the reference solution throughout the time evolution. However, phase shifts and amplitude discrepancies become more noticeable in the single-cycle ($n = 1$) solutions, particularly in the GA-2 scheme. For $\Delta t = 0.05$ and $n = 2$, the additional computational cycle helps mitigate phase errors and oscillations, leading to improved accuracy. For $\Delta t = 0.1$ and $n = 1$, errors become more

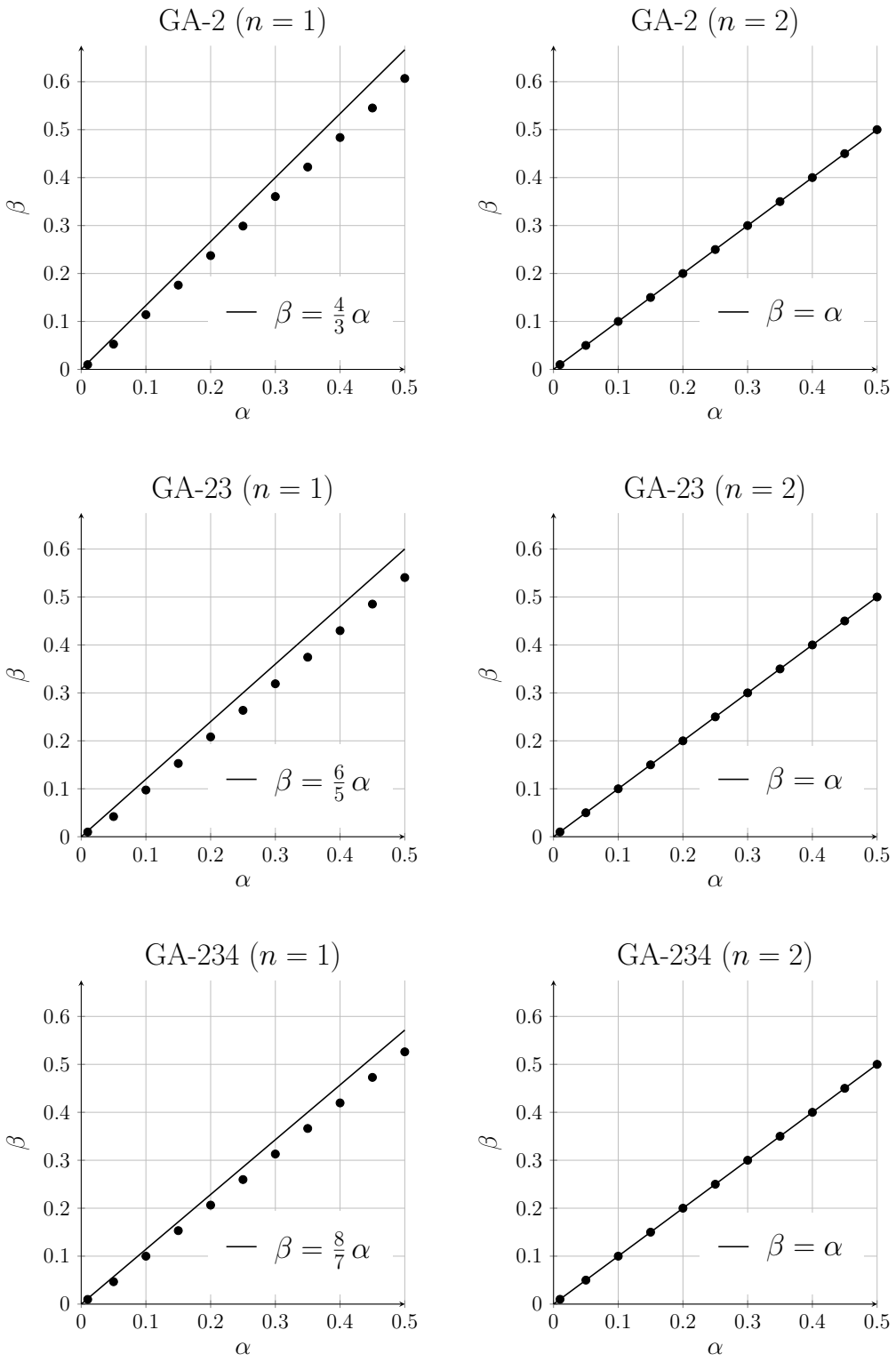

Figure 5.3.: Flow around a flexibly supported rigid cylinder; The dots represent the largest values of β that result in stable simulations for the time step $\Delta t = 0.1$. The solid lines denote the critical values obtained from the model problem analysis.

prominent in all single-cycle solutions. For $n = 2$, the solutions based on GA-23 and GA-234 maintain better agreement with the reference solution, but some discrepancies are still observed, suggesting that additional computational cycles may be required to further improve accuracy.

5.2. Example 2: Flow Induced Vibrations of a Flexible Beam

This problem, originally introduced in [114], has been widely utilised as a benchmark for validating the accuracy and stability of numerical methods in computational fluid–structure interaction [13, 37, 65, 91, 120].

The setup consists of an elastic beam attached to a rigid square, both immersed in an incompressible fluid flow. As the fluid moves past the rigid square, vortex shedding occurs in its wake, generating unsteady forces that induce large-amplitude oscillations in the beam. The inlet velocity is maintained at a uniform value of $u = u_\infty = 51.3$ m/s with $v = 0$ m/s, while the top and bottom walls function as slip boundaries, enforcing $v = 0$ m/s. The rigid square remains fixed, while the beam is clamped at its left end and is free to oscillate under the influence of fluid forces. The detailed geometry and boundary conditions are illustrated in Figure 5.7.

The material parameters for both the fluid and solid are taken from [114]. The fluid has a dynamic viscosity of $\mu^f = 1.82 \times 10^{-4}$ Pa s and a density of $\rho^f = 1.18 \times 10^{-3}$ kg/m^3. The solid is characterised by a shear modulus of $\mu^s = 9.2593 \times 10^5$ Pa, a bulk modulus of $K^s = 2.78 \times 10^6$ Pa, and a density of $\rho^s = 0.1$ kg/m^3. These parameters correspond to a Young's modulus of $E = 2.5 \times 10^6$ Pa and a Poisson's ratio of $\nu = 0.35$. The Reynolds number, calculated using the inlet velocity, the side length of the square, and the fluid viscosity, is obtained as $Re = \frac{\rho^f D u_\infty}{\mu^f} = 333$. The beam is modelled using 20 nine-noded quadratic continuum elements under plane-stress conditions, with

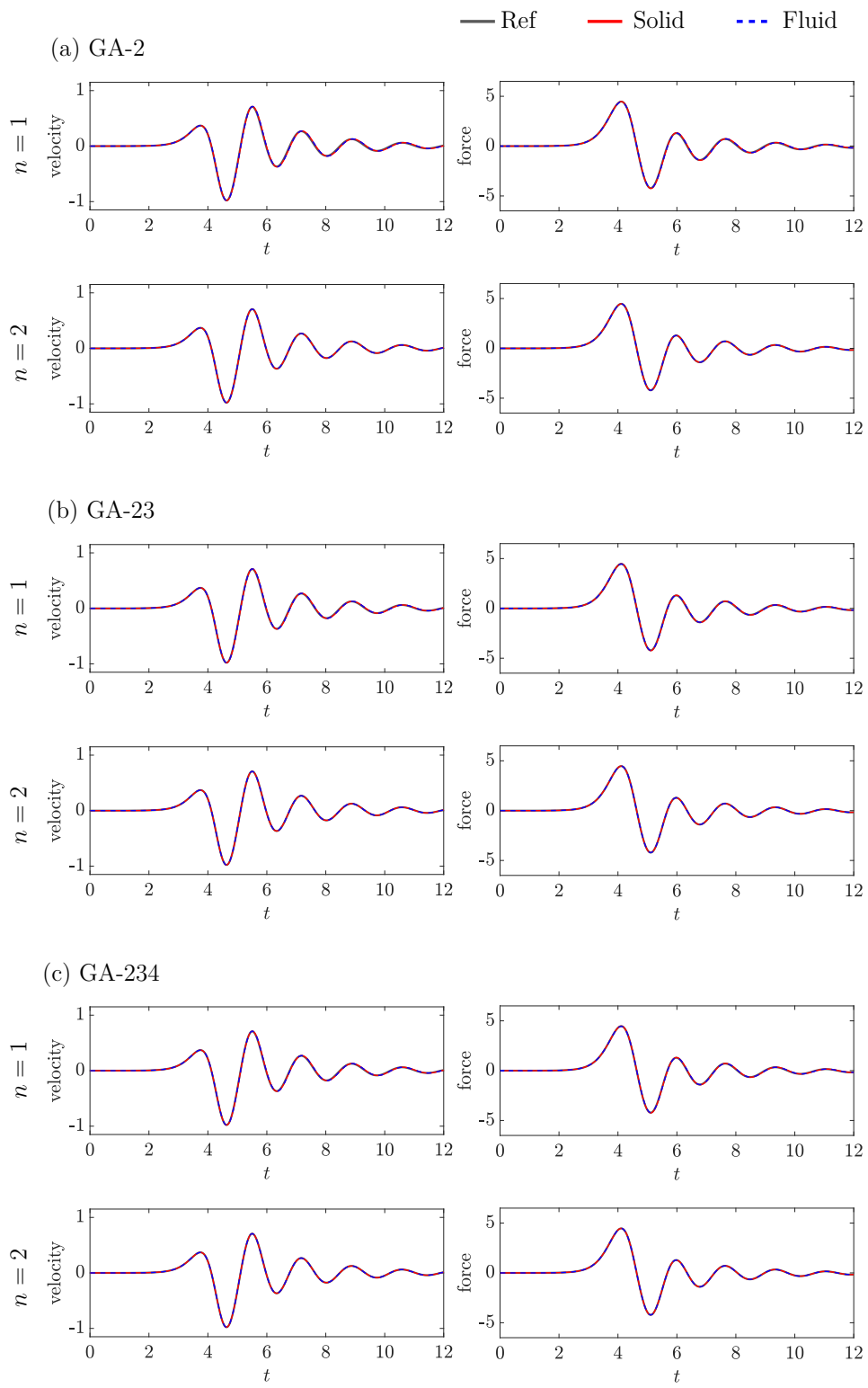

Figure 5.4.: Flow around flexibly supported rigid cylinder; evolution of traction force and velocity for $\alpha = 0.05$ and $\Delta t = 0.01$.

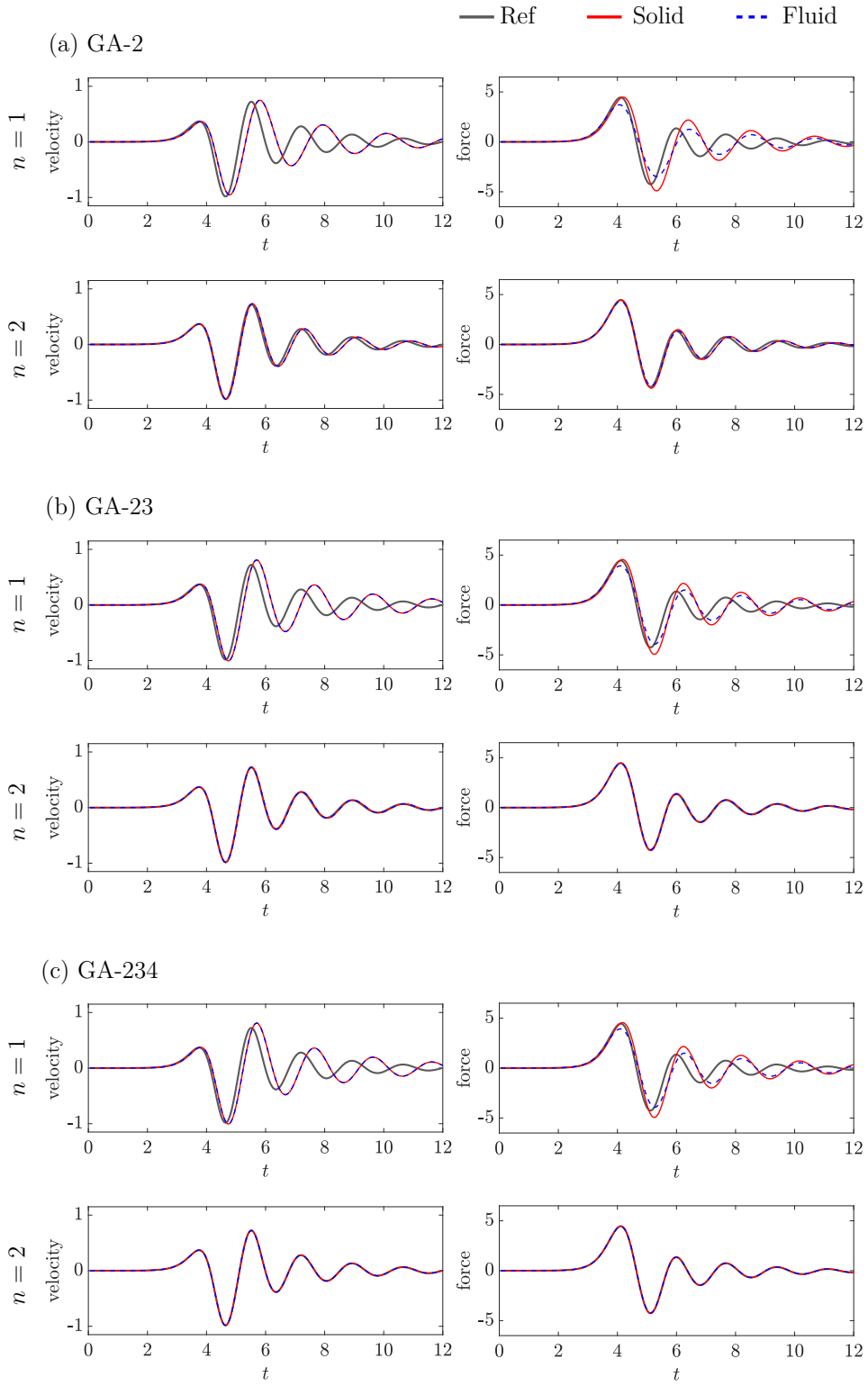

Figure 5.5.: Flow around flexibly supported rigid cylinder; evolution of traction force and velocity for $\alpha = 0.05$ and $\Delta t = 0.05$.

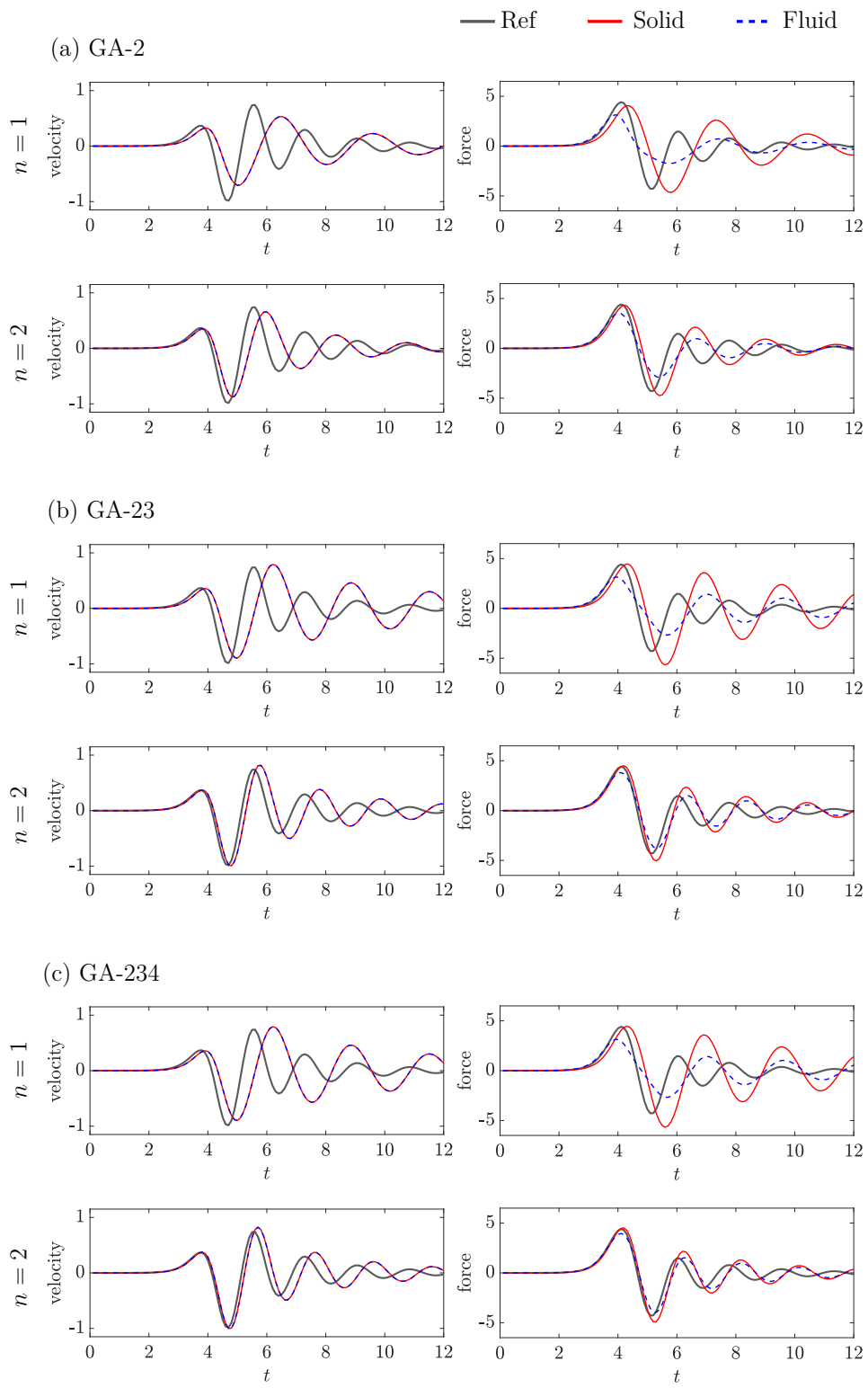

Figure 5.6.: Flow around flexibly supported rigid cylinder; evolution of traction force and velocity for $\alpha = 0.05$ and $\Delta t = 0.1$.

an incompressible Neo-Hookean material model. The fluid domain is discretised using 4,336 linear triangular elements with SUPG and PSPG stabilisation. The employed mesh is shown in Figure 5.8.

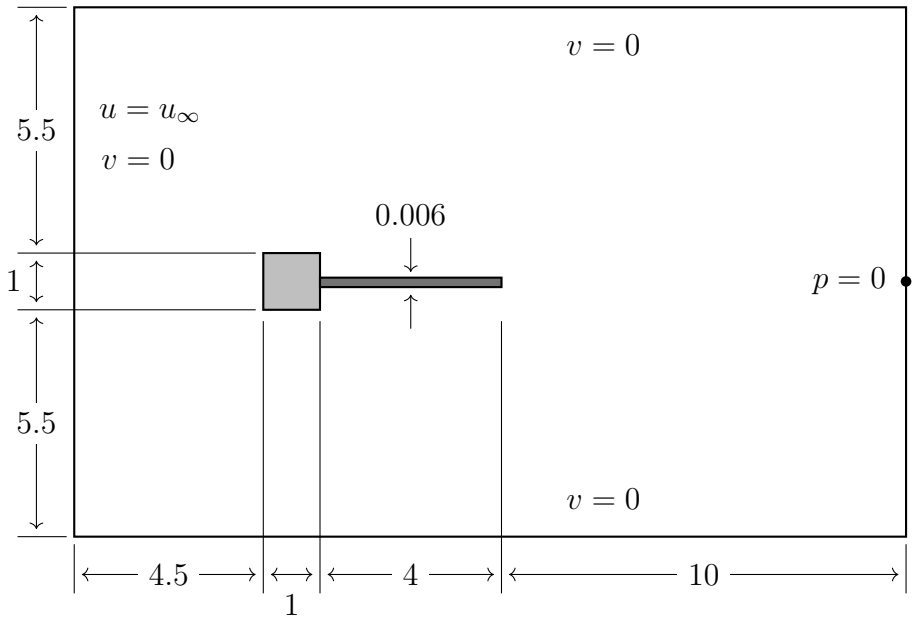

Figure 5.7.: Flow induced vibrations of a flexible beam; geometry and boundary conditions.

The vertical displacement of the beam tip is presented for $\Delta t = 0.01$ and $\Delta t = 0.005$ in Figures 5.9 and 5.10, respectively. The figures show the results obtained from the three staggered schemes based on GA-2, GA-23, and GA-234 for two computational cycles, $n = 1$ and $n = 2$. The relaxation factor β is set to $\beta = 0.7$, $\beta = 0.63$, and $\beta = 0.6$ for the schemes based on GA-2, GA-23, and GA-234, respectively. The results are compared with a reference solution computed using an iterative solution strategy, where each reference solution follows the same time integration scheme as its corresponding staggered solution.

The results demonstrate that all three staggered schemes, across both time steps and computational cycles, accurately align with the reference solution and effectively capture the oscillations. The oscillations remain stable and consistent in all cases, with no visible phase shifts or amplitude deviations.

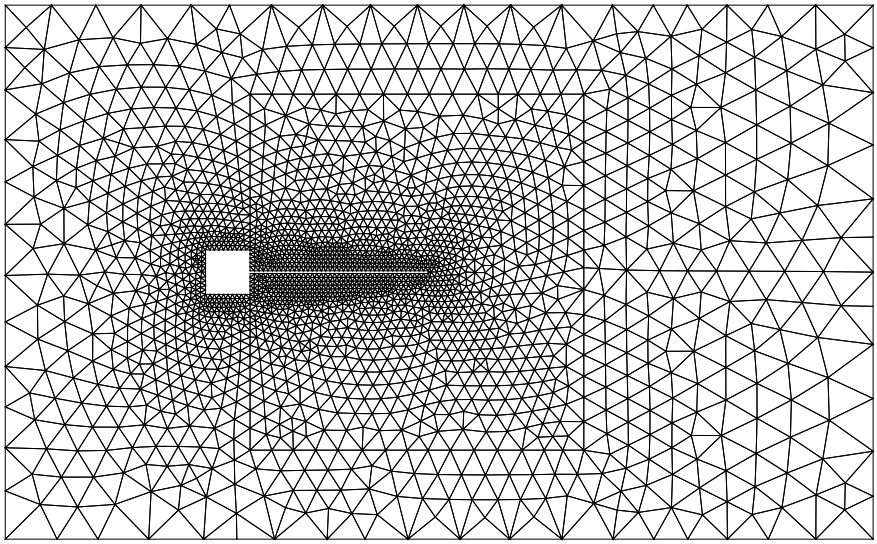

(a)

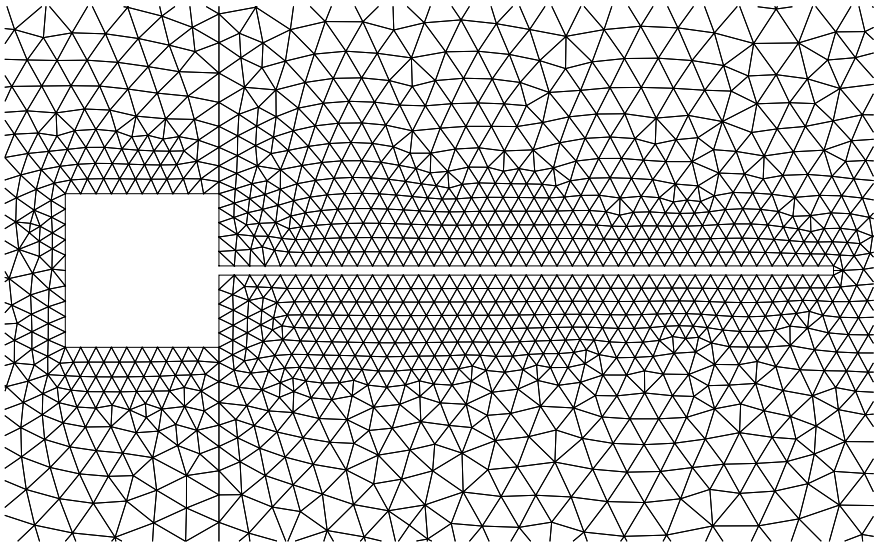

(b)

Figure 5.8.: Flow induced vibrations of a flexible beam; finite element mesh (a), mesh refinement around the beam (b).

Additionally, there is no significant difference between the solutions obtained with $n = 1$ and $n = 2$, suggesting that a single computational cycle may already be sufficient for accurate results in this case. Figure 5.11 shows the vorticity and velocity magnitude distributions during stable long-term oscillations.

Table 5.1 presents a comparison of the amplitude and frequency results obtained from the three staggered schemes for $\Delta t = 0.01$ and $n = 1$ with values reported in the literature. The results are consistent with previous studies and fall within the range of reported values. For the schemes based on GA-23 and GA-234, the obtained frequency is 3.26, with an amplitude of 1.26. The scheme based on GA-2 produces a slightly lower frequency of 3.18 and a slightly higher amplitude of 1.30.

Method	**Amplitude**	**Frequency**
GA-234	1.26	3.26
GA-23	1.26	3.26
GA-2	1.30	3.18
Wood et al. [120]	1.15	2.94
Habchi et al. [59]	1.02	3.25
Garg et al. [53]	1.01 - 1.23	3.14 - 3.32
Dettmer et al. [37]	1.10 - 1.40	2.96 - 3.31

Table 5.1.: Flow induced vibrations of a flexible beam; vertical tip displacement amplitude and frequency response obtained with $\Delta t = 0.01$.

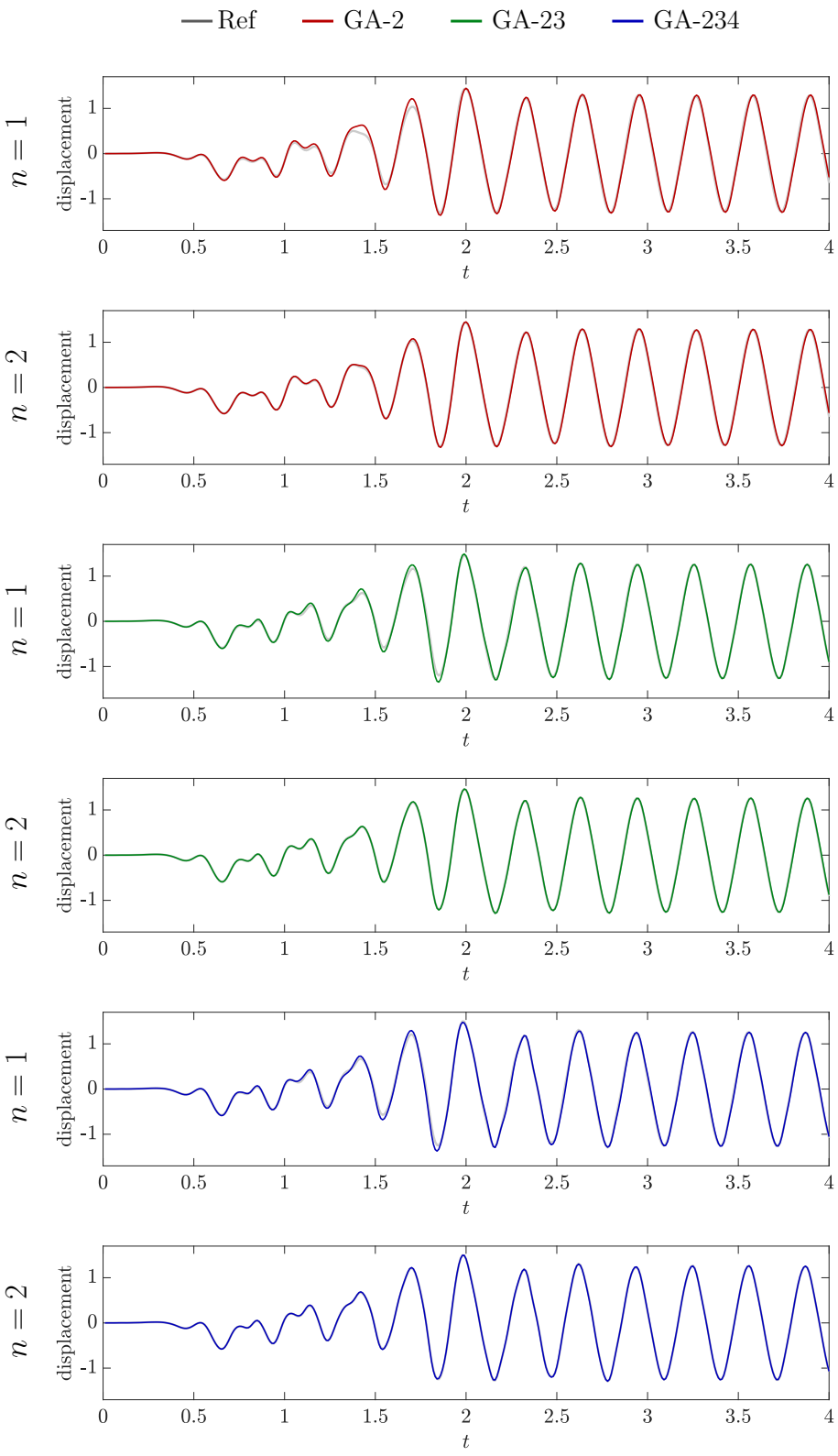

Figure 5.9.: Flow induced vibrations of a flexible beam; vertical tip displacement obtained with $\Delta t = 0.01$.

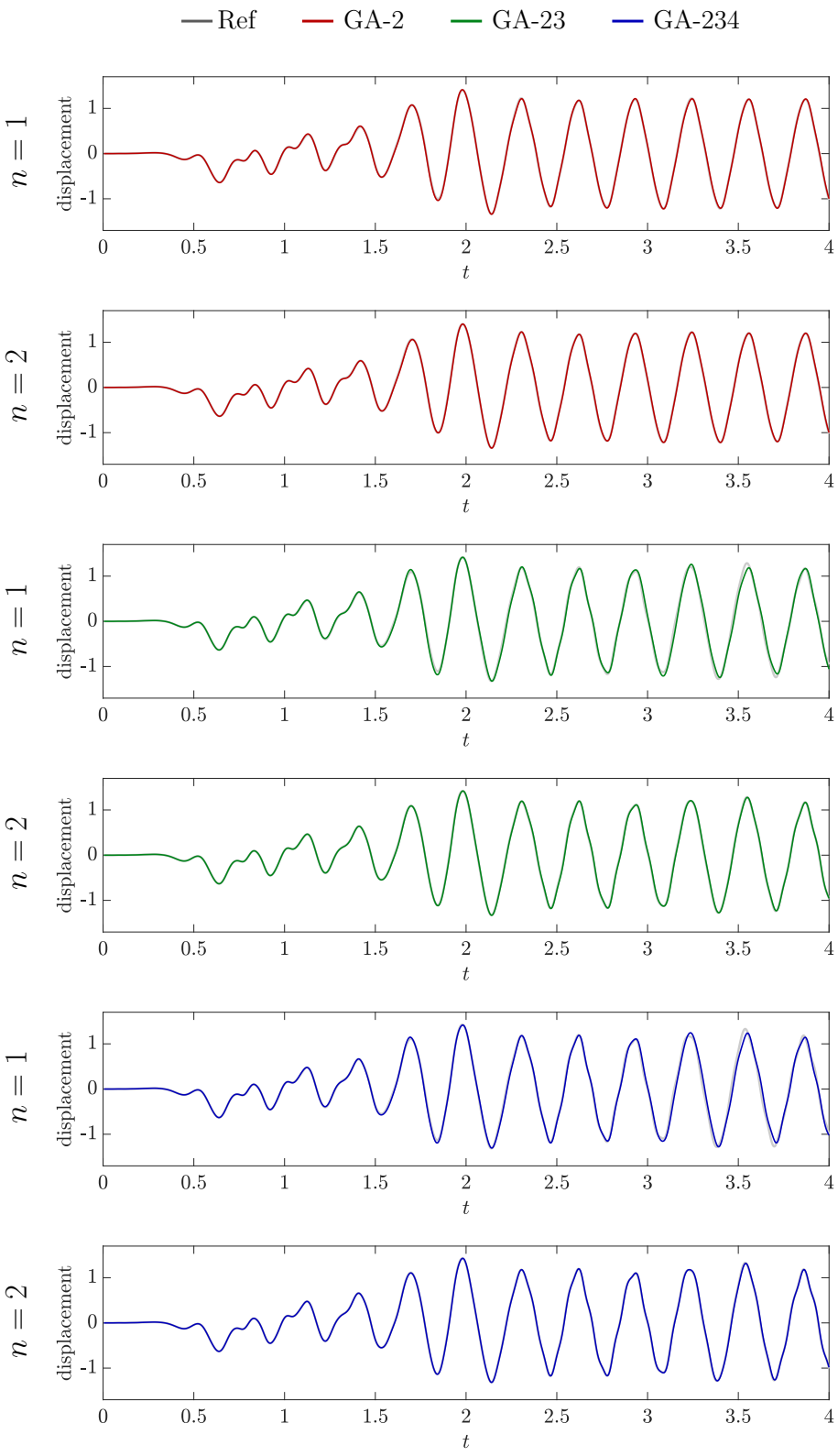

Figure 5.10.: Flow induced vibrations of a flexible beam; vertical tip displacement obtained with $\Delta t = 0.005$.

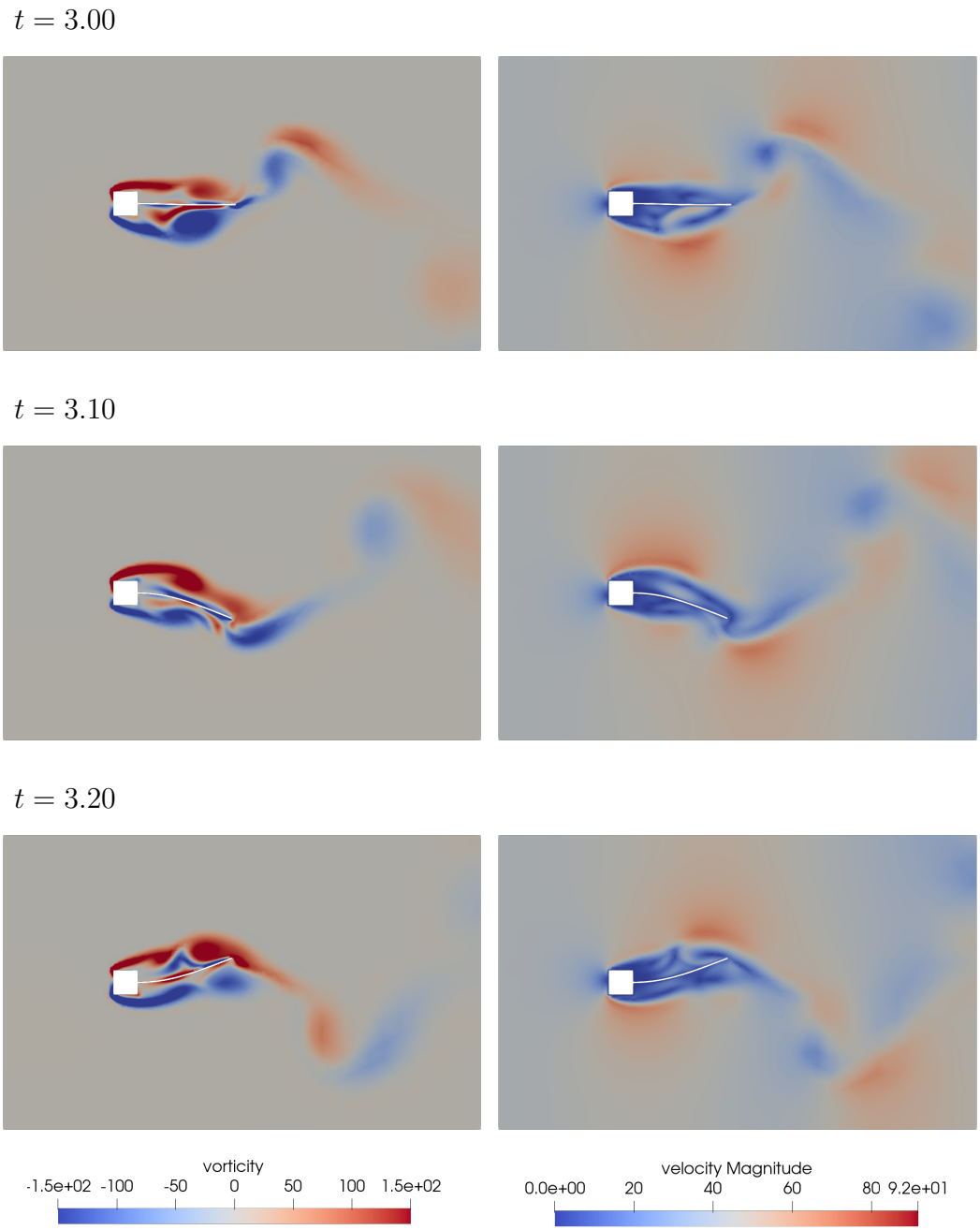

Figure 5.11.: Flow induced vibrations of a flexible beam; typical vorticity (right) and velocity magnitude (left) distribution during stable long-term oscillations.

5.3. Example 3: Flow Through a Flexible Tube

The following benchmark problem examines fluid flow through a flexible tube. The problem was originally introduced in [50] and has since been widely examined in the literature (see, for instance, [42, 88, 106, 121]). In the original setup, excitation was applied through a pressure boundary condition. A modified version of the problem was later proposed in [109], where the excitation is introduced by prescribing an inflow velocity at the inlet instead of using a pressure condition. The following presents a preliminary analysis, in which excitation is introduced via an imposed inflow velocity. The geometric dimensions and physical parameters remain consistent with the original configuration. The fluid domain consists of a straight tube with a radius of $R = 0.5\,\mathrm{cm}$. The study considers three tube lengths: $L = 1.5\,\mathrm{cm}$, $L = 3\,\mathrm{cm}$, and $L = 5\,\mathrm{cm}$. Figure 5.12 presents the computational mesh used for each case. The tube wall has a uniform thickness of $h = 0.1\,\mathrm{cm}$. The boundary conditions for the fluid domain consist of a prescribed axial velocity with a parabolic profile applied at the inlet, while the transverse velocity components are fixed. At the outlet, the pressure is set to zero. The solid is clamped at the inlet and free at the outlet.

The fluid is assumed to be incompressible, with a density $\rho_f = 1\,\mathrm{g/cm^3}$ and a dynamic viscosity $\mu = 0.3\,\mathrm{g/(cm \cdot s)}$. The fluid flow is solved using a stabilised finite element method based on the SUPG/PSPG formulation. The solid tube wall has a density $\rho_s = 1.2\,\mathrm{g/cm^3}$, a Young's modulus $E = 3 \times 10^6\,\mathrm{dyn/cm^2}$, and a Poisson's ratio $\nu = 0.3$. The solid is modelled using a Neo-Hookean formulation. All quantities are expressed in CGS units unless otherwise specified. The inflow velocity is prescribed as

$$u_{\mathrm{in}}(t) = \begin{cases} 500\,(1 - \cos(5\pi t))\,, & \text{for } t \leq 0.4 \\ 0, & \text{otherwise} \end{cases} \tag{5.2}$$

The added mass can be approximated as

$$\alpha = \frac{\rho_s h \pi^2 R}{\rho_s h \pi^2 R + 2\rho_f L^2} \tag{5.3}$$

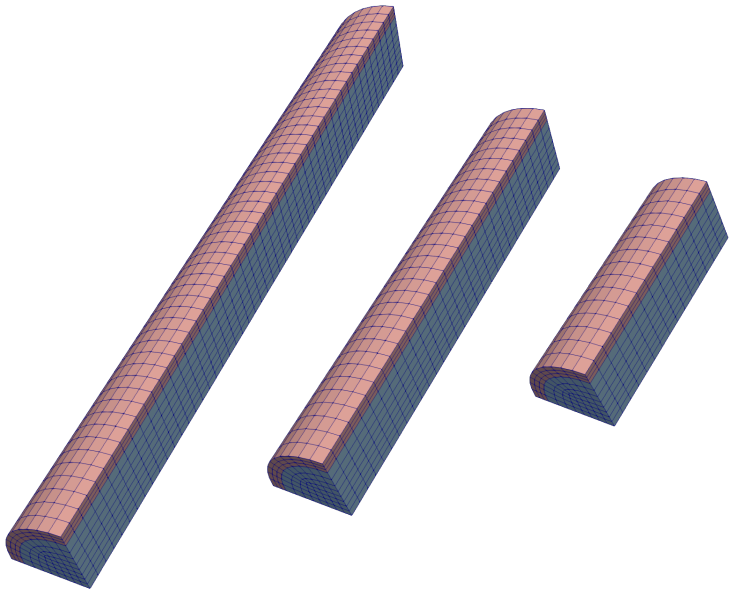

$L = 5.0$ $L = 3.0$ $L = 1.5$

Figure 5.12.: Flow through a flexible tube; finite element meshes for the three different tube lengths. The red region represents the solid domain, and the blue region represents the fluid domain.

For the considered tube lengths, the corresponding values of α are $\alpha \approx 0.012$ for $L = 5\,\text{cm}$, $\alpha \approx 0.032$ for $L = 3\,\text{cm}$, and $\alpha \approx 0.12$ for $L = 1.5\,\text{cm}$.

Figure 5.13 presents the displacement magnitude at the midpoint for the three cases, computed using staggered schemes based on GA-2, GA-23, and GA-234 with $n = 1$. Results were obtained using time steps of $\Delta t = 0.001$ and $\Delta t = 0.002$, and are compared against a reference solution computed with $\Delta t = 0.0005$.

The results demonstrate that the proposed staggered methods are capable of capturing a wide range of added-mass effects. As the time step increases, numerical errors become more pronounced, particularly for the GA-2 scheme. Additionally, for larger values of α , all methods closely follow the reference solution, exhibiting only minor deviations. As expected, increasing α leads to a notable reduction in the overall displacement magnitude.

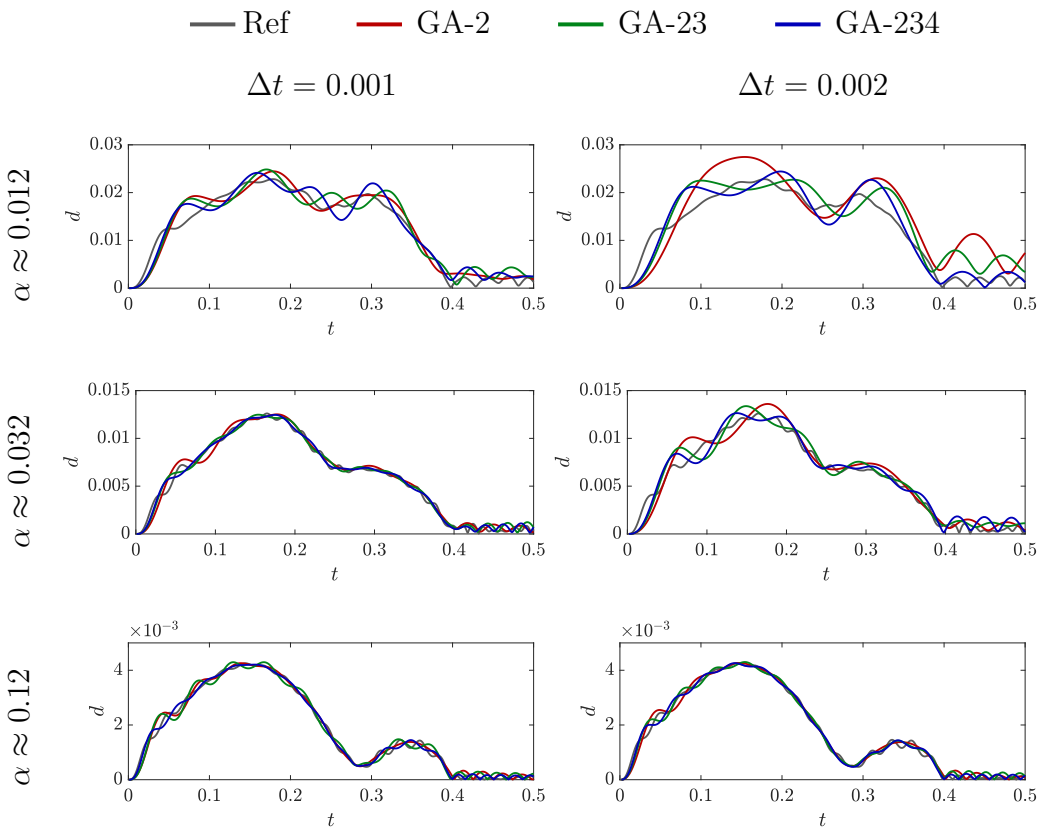

Figure 5.13.: Flow through a flexible tube; displacement magnitude at the midpoint for three tube lengths using staggered schemes with $n = 1$.

Chapter 6

Conclusions

The primary objectives of this thesis, as outlined in Section 1.1, have been successfully achieved. The research has focused on the development of a new family of time integration schemes for dynamic systems, ranging from first order to second order problems, and the development of new staggered methods for fluid–structure interaction based on Dirichlet–Neumann coupling. The following section outlines the main contributions and conclusions of the work presented in this thesis.

6.1. Achievements and Conclusions

This thesis presents the formulation of a novel family of implicit time integration schemes that retain the desirable properties of the generalised-α method, namely second order accuracy, unconditional stability, and user-controlled high-frequency numerical damping via the parameter ρ_∞, while offering enhanced numerical dissipation and improved accuracy characteristics. These schemes were constructed using a linearly weighted combination of the standard second order generalised-α method and its higher order extensions. The weighting factors were systematically determined using the Jury stability criterion, ensuring that the resulting methods remain unconditionally stable.

The schemes were initially formulated for first order systems typically encountered in fluid dynamics, and were later extended to second order problems commonly found in structural dynamics, using a standard order reduction approach in which auxiliary solution variables were introduced to recast the system into first order form. This extension enabled the schemes to retain their theoretical properties while adapting naturally to the second order differential formulation.

A wide range of numerical tests, covering both first order and second order problems, was conducted to evaluate the performance of the proposed methods. The results consistently demonstrated the robustness, enhanced accuracy, and broad applicability of the schemes.

Next, three new staggered partitioned schemes for fluid–structure interaction problems were developed based on the newly formulated time integration methods. These schemes employ Dirichlet–Neumann boundary conditions and were designed to address the well-known stability limitations of conventional staggered approaches. The proposed methods incorporate a force predictor in the initial step, along with a relaxation step in which the final interface force is computed as a weighted average of the predicted and computed values.

In these staggered schemes, the fluid subproblem used the time integration method from Chapter 2, while the solid subproblem followed the approach from Chapter 3. Furthermore, an enhanced second order predictor was developed using a strategy analogous to that employed in the formulation of the time integrators; namely, by linearly combining a standard second order predictor with higher order predictors. A non-iterative n-cycle version of the staggered schemes was also introduced and evaluated. This approach improves accuracy by performing a fixed number of computational cycles. In contrast to classical iterative schemes, which enforce coupling through repeated convergence checks, the n-cycle approach avoids the high and unpredictable computational cost typically associated with this process, offering a more efficient alternative with fixed computational effort per time step. A comprehensive theoretical and numerical investigation of the stability and accuracy of these schemes, for

both $n = 1$ and $n > 1$, was conducted using a benchmark fluid–structure interaction problem involving a thin-walled elastic tube with a circular cross-section conveying fluid.

The proposed single-cycle and multi-cycle versions of the staggered schemes were evaluated in two-dimensional and three-dimensional fluid-structure interaction problems. The results from these simulations demonstrate that the proposed schemes are capable of handling a wide range of FSI problems. Notably, the methods were shown to remain stable and accurate even under critical added-mass conditions.

6.2. Future Work

The following suggestions are made for future research

- The proposed staggered methods should be tested on more complex problems, and a more in-depth analysis should be conducted to evaluate their scalability, robustness, and practical relevance. The flow through a flexible tube problem presented in Section 5.3 represents a benchmark case in the field of fluid–structure interaction. In this work, it has only been addressed at a preliminary level, and a more detailed investigation is required to fully assess the performance and limitations of the proposed schemes in a strongly coupled setting.
- Replacing the current finite element framework with a finite volume approach, particularly one that uses pressure–velocity segregation, could lead to significant performance gains. Such strategies are common in industrial CFD software and may provide more efficient handling of incompressible flow problems.
- Due to their computational efficiency, the staggered schemes developed in this thesis are well suited for use in optimisation and control applications. This potential should be further investigated.

Bibliography

[1] O. H. Ammann, T. Von Kármán, and G. B. Woodruff. "The failure of the Tacoma Narrows bridge". In: *Federal Works Agency* (1941).

[2] M. Arnold and O. Brüls. "Convergence of the generalized-α scheme for constrained mechanical systems". In: *Multibody System Dynamics* 18.2 (2007), pp. 185–202. DOI: 10.1007/s11044-007-9084-0.

[3] M. Astorino, F. Chouly, and M. A. Fernández. "Robin Based Semi-Implicit Coupling in Fluid-Structure Interaction: Stability Analysis and Numerics". In: *SIAM Journal on Scientific Computing* 31.6 (2010), pp. 4041–4065.

[4] S. Badia, F. Nobile, and C. Vergara. "Fluid–structure partitioned procedures based on Robin transmission conditions". In: *Journal of Computational Physics* 227.14 (2008), pp. 7027–7051. ISSN: 0021-9991.

[5] C. Baiocchi and M. Crouzeix. "On the equivalence of a-stability and g-stability". In: *Applied Numerical Mathematics* 5.1 (1989), pp. 19–22. ISSN: 0168-9274.

[6] K.-J. Bathe. "Conserving energy and momentum in nonlinear dynamics: A simple implicit time integration scheme". In: *Computers and Structures* 85 (2007), pp. 437–445.

[7] K.-J. Bathe and M. Baig. "On a composite implicit time integration procedure for nonlinear dynamics". In: *Computers and Structures* 83 (Dec. 2005), pp. 2513–2524.

[8] K.-J. Bathe and G. Noh. "Insight into an implicit time integration scheme for structural dynamics". In: *Computers and Structures* 98-99 (2012), pp. 1–6. ISSN: 0045-7949.

[9] G. Bauer, P. Gamnitzer, V. Gravemeier, and W. A. Wall. "An isogeometric variational multiscale method for large-eddy simulation of coupled multi-ion transport in turbulent flow". In: *Journal of Computational Physics* 251 (2013), pp. 194–208. ISSN: 0021-9991.

[10] Y. Bazilevs, V. Calo, J. Cottrell, T. Hughes, A. Reali, and G. Scovazzi. "Variational multiscale residual-based turbulence modeling for large eddy simulation of incompressible flows". In: *Computer Methods in Applied Mechanics and Engineering* 197.1 (2007), pp. 173–201. ISSN: 0045-7825.

[11] Y. Bazilevs, V. Calo, T. Hughes, and Y. Zhang. "Isogeometric fluid-structure interaction: Theory, algorithms, and computations". In: *Computational Mechanics* 43 (Dec. 2008), pp. 3–37.

[12] Y. Bazilevs, K. Takizawa, and T. E. Tezduyar. *Computational fluid-structure interaction: methods and applications*. John Wiley & Sons, 2013.

[13] F.-K. Benra, H. J. Dohmen, J. Pei, S. Schuster, and B. Wan. "A comparison of one-way and two-way coupling methods for numerical analysis of fluid-structure interactions". In: *Journal of applied mathematics* 2011.1 (2011), p. 853560.

[14] K. Y. Billah and R. H. Scanlan. "Resonance, Tacoma Narrows bridge failure, and undergraduate physics textbooks". In: *American Journal of Physics* 59 (1991), pp. 118–124.

[15] R. Blevins. *Flow-induced Vibration*. Van Nostrand Reinhold, 1990. ISBN: 9780442206512.

[16] R. Brayton, F. Gustavson, and G. Hachtel. "A new efficient algorithm for solving differential-algebraic systems using implicit backward differentiation formulas". In: *Proceedings of the IEEE* 60.1 (1972), pp. 98–108.

[17] M. Bukač, S. Čanić, R. Glowinski, J. Tambača, and A. Quaini. "Fluid structure interaction in blood flow capturing non-zero longitudinal structure displacement". In: *Journal of Computational Physics* 235 (2013), pp. 515–541. ISSN: 0021-9991.

[18] M. Bukač and B. Muha. "Stability and convergence analysis of the kinematically coupled scheme and its extensions for the fluid-structure interaction". In: *SIAM Journal on Numerical Analysis* 54 (Jan. 2016). DOI: 10.1137/16M1055396.

[19] H.-J. Bungartz, F. Lindner, B. Gatzhammer, M. Mehl, K. Scheufele, A. Shukaev, and B. Uekermann. "preCICE – A fully parallel library for multi-physics surface coupling". In: *Computers and Fluids* 141 (2016). Advances in Fluid-Structure Interaction, pp. 250–258. ISSN: 0045-7930.

[20] E. Burman, M. A. Fernández, and S. Frei. "A Nitsche-based formulation for fluid-structure interactions with contact". In: *ESAIM: Mathematical Modelling and Numerical Analysis* 54.2 (2020), pp. 531–564.

[21] E. Burman and M. A. Fernández. "Stabilization of explicit coupling in fluid–structure interaction involving fluid incompressibility". In: *Computer Methods in Applied Mechanics and Engineering* 198.5 (2009), pp. 766–784. ISSN: 0045-7825.

[22] E. Burman and M. A. Fernández. "Explicit strategies for incompressible fluid-structure interaction problems: Nitsche type mortaring versus Robin–Robin coupling". In: *International Journal for Numerical Methods in Engineering* 97.10 (2014), pp. 739–758.

[23] J. C. Butcher. *Numerical methods for ordinary differential equations*. John Wiley and Sons, 2016.

[24] P. Causin, J. Gerbeau, and F. Nobile. "Added-mass effect in the design of partitioned algorithms for fluid–structure problems". In: *Computer Methods in Applied Mechanics and Engineering* 194.42 (2005), pp. 4506–4527. ISSN: 0045-7825.

[25] Y. Choo and D. Kim. "Schur Stability of Complex Polynomials". In: *Journal of Institute of Control, Robotics and Systems* 15.7 (2009), pp. 671–674. DOI: 10.5302/j.icos.2009.15.7.671.

[26] C. Chu. "Numerical methods in fluid dynamics". In: *Advances in applied mechanics* 18 (1979), pp. 285–331.

[27] J. Chung and G. M. Hulbert. "A Time Integration Algorithm for Structural Dynamics With Improved Numerical Dissipation: The Generalized-α Method". In: *Journal of Applied Mechanics* 60.2 (June 1993), pp. 371–375. ISSN: 0021-8936.

[28] B. I. Cohen, A. Langdon, and A. Friedman. "Implicit time integration for plasma simulation". In: *Journal of Computational Physics* 46.1 (1982), pp. 15–38. ISSN: 0021-9991.

[29] J. Crank and P. Nicolson. "A practical method for numerical evaluation of solutions of partial differential equations of the heat-conduction type". In: *Mathematical Proceedings of the Cambridge Philosophical Society* 43.1 (1947), pp. 50–67.

[30] G. Dahlquist. "Convergence and Stability in the Numerical Integration of Ordinary Differential Equations". In: *Mathematica Scandinavica* 4.1 (1956), pp. 33–53. ISSN: 00255521, 19031807.

[31] G. Dahlquist. "A special stability problem for linear multistep methods". In: *BIT Numerical Mathematics* 3 (1963), pp. 27–43.

[32] J. Degroote, J. Bols, and L. Taelman. "Comparison between Two Different Decompositions for the Solution of Fluid-Structure Interaction Problems". In: (2013), pp. 1000–1008.

[33] J. Degroote. "On the similarity between Dirichlet–Neumann with interface artificial compressibility and Robin–Neumann schemes for the solution of fluid-structure interaction problems". In: *Journal of Computational Physics* 230.17 (2011), pp. 6399–6403. ISSN: 0021-9991.

[34] J. Degroote. "Partitioned simulation of fluid-structure interaction: Coupling black-box solvers with quasi-Newton techniques". In: *Archives of computational methods in engineering* 20.3 (2013), pp. 185–238.

[35] J. Degroote, K.-J. Bathe, and J. Vierendeels. "Performance of a new partitioned procedure versus a monolithic procedure in fluid–structure interaction". In: *Computers and Structures* 87.11 (2009). Fifth MIT Conference on Computational Fluid and Solid Mechanics, pp. 793–801. ISSN: 0045-7949.

[36] W. Dettmer and D. Perić. "An analysis of the time integration algorithms for the finite element solutions of incompressible Navier–Stokes equations based on a stabilised formulation". In: *Computer Methods in Applied Mechanics and Engineering* 192.9 (2003), pp. 1177–1226. ISSN: 0045-7825.

[37] W. Dettmer and D. Perić. "A computational framework for fluid–structure interaction: Finite element formulation and applications". In: *Computer Methods in Applied Mechanics and Engineering* 195.41 (2006). John H. Argyris Memorial Issue. Part II, pp. 5754–5779.

[38] W. Dettmer and D. Perić. "A new staggered scheme for fluid-structure interaction". In: *International Journal for Numerical Methods in Engineering* 93 (Jan. 2013), pp. 1–22.

[39] W. G. Dettmer, A. Lovrić, C. Kadapa, and D. Perić. "New iterative and staggered solution schemes for incompressible fluid-structure interaction based on Dirichlet-Neumann coupling". In: *International Journal for Numerical Methods in Engineering* 122.19 (2021), pp. 5204–5235.

[40] M. Dokainish and K. Subbaraj. "A survey of direct time-integration methods in computational structural dynamics—I. Explicit methods". In: *Computers and Structures* 32.6 (1989), pp. 1371–1386. ISSN: 0045-7949.

[41] D. Durran. *Numerical Methods for Fluid Dynamics: With Applications to Geophysics*. Texts in Applied Mathematics. Springer New York, 2010. ISBN: 9781441964120.

[42] A. Eken and M. Sahin. "A parallel monolithic algorithm for the numerical simulation of large-scale fluid structure interaction problems". In: *International Journal for Numerical Methods in Fluids* 80.12 (2016), pp. 687–714.

[43] S. Erlicher, L. Bonaventura, and O. Bursi. "The analysis of the Generalized-α method for non-linear dynamic problems". In: *Computational Mechanics* 28 (Jan. 2002), pp. 83–104.

[44] M. Ezkurra, J. Esnaola, M. Martinez Agirre, U. Etxeberria, U. Lertxundi, L. Colomo, M. Begiristain, and I. Zurutuza. "Analysis of One-Way and Two-Way FSI Approaches to Characterise the Flow Regime and the Mechanical Behaviour during Closing Manoeuvring Operation of a Butterfly Valve". In: *World Academy of Science, Engineering and Technology, International Journal of Mechanical and Materials Engineering* 12 (Apr. 2018), pp. 313–319.

[45] C. Farhat. "CFD-Based Nonlinear Computational Aeroelasticity". In: *Encyclopedia of Computational Mechanics*. Ed. by E. Stein, R. de Borst, and T. J. R. Hughes. John Wiley and Sons, Ltd, 2004. Chap. 13. ISBN: 9780470091357. DOI: 10.1002/0470091355.ecm063.

[46] C. Farhat, P. Geuzaine, and G. Brown. "Application of a three-field nonlinear fluid–structure formulation to the prediction of the aeroelastic parameters of an F-16 fighter". In: *Computers and Fluids* 32.1 (2003), pp. 3–29. ISSN: 0045-7930.

[47] C. Felippa, K. C. Park, and J. Deruntz. "Stabilization of staggered solution procedures for fluid–structure interaction analysis". In: *American Society of Mechanical Engineers, Applied Mechanics Division, AMD* 26 (Jan. 1977).

[48] L. Feng, H. Gao, and X. Luo. "Whole-heart modelling with valves in a fluid–structure interaction framework". In: *Computer Methods in Applied Mechanics and Engineering* 420 (2024), p. 116724. ISSN: 0045-7825.

[49] M. A. Fernández. "Incremental displacement-correction schemes for incompressible fluid-structure interaction: stability and convergence analysis". In: *Numerische Mathematik* 123.1 (2013), pp. 21–65.

[50] L. Formaggia, J. Gerbeau, F. Nobile, and A. Quarteroni. "On the coupling of 3D and 1D Navier–Stokes equations for flow problems in compliant vessels". In: *Computer Methods in Applied Mechanics and Engineering* 191.6 (2001). Minisymposium on Methods for Flow Simulation and Modeling, pp. 561–582. ISSN: 0045-7825.

[51] C. Förster, W. A. Wall, and E. Ramm. "Artificial added mass instabilities in sequential staggered coupling of nonlinear structures and incompressible viscous flows". In: *Computer Methods in Applied Mechanics and Engineering* 196.7 (2007), pp. 1278–1293. ISSN: 0045-7825.

[52] Fraunhofer Institute for Algorithms and Scientific Computing (SCAI). *MpCCI 4.7.1-1 Documentation*. Accessed: March 2025. Fraunhofer SCAI. Sankt Augustin, Germany, 2023. URL: `https://www.mpcci.de/content/dam/scai/mpcci/documents/MpCCIdoc.pdf`.

[53] D. Garg, P. Papale, and A. Longo. "A partitioned solver for compressible/incompressible fluid flow and light structure". In: *Computers and Mathematics with Applications* 100 (2021), pp. 182–195. ISSN: 0898-1221.

[54] C. Gear. *Numerical Initial Value Problems in Ordinary Differential Equations*. Automatic Computation Series. Prentice-Hall, 1971. ISBN: 9780136266068.

[55] M. Gee, U. Küttler, and W. Wall. "Truly monolithic algebraic multigrid for fluid–structure interaction". In: *International Journal for Numerical Methods in Engineering* 85 (Feb. 2011), pp. 987–1016.

[56] L. Gerardo-Giorda, F. Nobile, and C. Vergara. "Analysis And Optimization Of Robin-Robin Partitioned Procedures In Fluid-Structure Interaction Problems". In: *SIAM J Numer Anal* 48 (Jan. 2010). DOI: `10.1137/09076605X`.

[57] D. Givoli. "Dahlquist's barriers and much beyond". In: *Journal of Computational Physics* 475 (2023), p. 111836. ISSN: 0021-9991.

[58] O. Guerri, A. Hamdouni, and A. Sakout. "Fluid Structure Interaction of Wind Turbine Airfoils". In: *Wind Engineering* 32 (Dec. 2008). DOI: `10.1260/030952408787548875`.

[59] C. Habchi, S. Russeil, D. Bougeard, J.-L. Harion, T. Lemenand, A. Ghanem, D. D. Valle, and H. Peerhossaini. "Partitioned solver for strongly coupled fluid–structure interaction". In: *Computers and Fluids* 71 (2013), pp. 306–319. ISSN: 0045-7930.

[60] E. Hairer, S. Nørsett, and G. Wanner. *Solving Ordinary Differential Equations II: Stiff and Differential-Algebraic Problems*. Solving Ordinary Differential Equations II: Stiff and Differential-algebraic Problems. Springer, 1993. ISBN: 9783540604525.

[61] T. He. "On a Partitioned Strong Coupling Algorithm for Modeling Fluid–Structure Interaction". In: *International Journal of Applied Mechanics* 07.02 (2015), p. 1550021.

[62] T. He. "A strongly-coupled cell-based smoothed finite element solver for unsteady viscoelastic fluid–structure interaction". In: *Computers and Structures* 235 (2020), p. 106264. ISSN: 0045-7949.

[63] H. M. Hilber, T. J. Hughes, and R. L. Taylor. "Improved numerical dissipation for time integration algorithms in structural dynamics". In: *Earthquake Engineering and Structural Dynamics* 5.3 (1977), pp. 283–292.

[64] J. C. Houbolt. "A recurrence matrix solution for the dynamic response of elastic aircraft". In: *Journal of the Aeronautical Sciences* 17.9 (1950), pp. 540–550.

[65] B. Hübner, E. Walhorn, and D. Dinkler. "A monolithic approach to fluid–structure interaction using space–time finite elements". In: *Computer Methods in Applied Mechanics and Engineering* 193.23 (2004), pp. 2087–2104. ISSN: 0045-7825.

[66] T. Hughes. *The Finite Element Method: Linear Static and Dynamic Finite Element Analysis*. Dover Civil and Mechanical Engineering. Dover Publications, 2012. ISBN: 9780486135021.

[67] D. Ishihara and S. Yoshimura. "A monolithic approach for interaction of incompressible viscous fluid and an elastic body based on fluid pressure Poisson equation". In: *International Journal for Numerical Methods in Engineering* 64.2 (2005), pp. 167–203.

[68] K. E. Jansen, C. H. Whiting, and G. M. Hulbert. "A generalized-α method for integrating the filtered Navier-Stokes equations with a stabilized finite element method". In: *Computer Methods in Applied Mechanics and Engineering* 190.3 (2000), pp. 305–319. ISSN: 0045-7825.

[69] M. M. Joosten, W. G. Dettmer, and D. Perić. "Analysis of the block Gauss–Seidel solution procedure for a strongly coupled model problem with reference to fluid–structure interaction". In: *International Journal for Numerical Methods in Engineering* 78.7 (2009), pp. 757–778.

[70] M. M. Joosten, W. G. Dettmer, and D. Perić. "On the temporal stability and accuracy of coupled problems with reference to fluid–structure interaction". In: *International Journal for Numerical Methods in Fluids* 64.10-12 (2010), pp. 1363–1378.

[71] E. I. Jury. "A Simplified Stability Criterion for Linear Discrete Systems". In: *Proceedings of the IRE* 50.6 (1962), pp. 1493–1500.

[72] E. Jury. *Theory and Application of the Z-transform Method*. Wiley, 1964. ISBN: 9780471453451.

[73] C. Kadapa, W. Dettmer, and D. Perić. "On the advantages of using the first-order generalised-alpha scheme for structural dynamic problems". In: *Computers and Structures* 193 (2017), pp. 226–238.

[74] C. Kadapa, W. Dettmer, and D. Perić. "A stabilised immersed framework on hierarchical b-spline grids for fluid-flexible structure interaction with solid–solid contact". In: *Computer Methods in Applied Mechanics and Engineering* 335 (2018), pp. 472–489. ISSN: 0045-7825.

[75] C. Kadapa. "A second-order accurate non-intrusive staggered scheme for the interaction of ultra-lightweight rigid bodies with fluid flow". In: *Ocean Engineering* 217 (2020), p. 107940. ISSN: 0029-8018.

[76] C. Kadapa, W. Dettmer, and D. Perić. "Accurate iteration-free mixed-stabilised formulation for laminar incompressible Navier-Stokes: Applications to fluid-structure interaction". In: *Journal of Fluids and Structures* 97 (June 2020).

[77] C. Kadapa, W. G. Dettmer, and D. Perić. "Accurate iteration-free mixed-stabilised formulation for laminar incompressible Navier–Stokes: Applications to fluid–structure interaction". In: *Journal of Fluids and Structures* 97 (2020), p. 103077. ISSN: 0889-9746.

[78] C. Kees, I. Akkerman, M. Farthing, and Y. Bazilevs. "A conservative level set method suitable for variable-order approximations and unstructured meshes". In: *Journal of Computational Physics* 230.12 (2011), pp. 4536–4558. ISSN: 0021-9991.

[79] H. Kim, H. Rundfeldt, I. Lee, and S. Lee. "Tissue-growth-based synthetic tree generation and perfusion simulation". In: *Biomechanics and Modeling in Mechanobiology* 22 (Mar. 2023), pp. 1–18.

[80] K.-T. Kim and K.-J. Bathe. "Accurate solution of wave propagation problems in elasticity". In: *Computers and Structures* 249 (2021), p. 106502.

[81] W. Kim and H. Choi. "Immersed boundary methods for fluid-structure interaction: A review". In: *International Journal of Heat and Fluid Flow* 75 (2019), pp. 301–309. ISSN: 0142-727X.

[82] W. Kim and S. Y. Choi. "An improved implicit time integration algorithm: The generalized composite time integration algorithm". In: *Computers and Structures* 196 (2018), pp. 341–354.

[83] D. Kreculj and B. Rasuo. "7 - Impact damage modeling in laminated composite aircraft structures". In: *Sustainable Composites for Aerospace Applications*. Ed. by M. Jawaid and M. Thariq. Woodhead Publishing Series in Composites Science and Engineering. Woodhead Publishing, 2018, pp. 125–153. ISBN: 978-0-08-102131-6.

[84] U. Küttler and W. Wall. "Fixed-point fluid-structure interaction solvers with dynamic relaxation". In: *Computational Mechanics* 43 (Jan. 2008), pp. 61–72.

[85] S.-B. Kwon, K.-J. Bathe, and G. Noh. "An analysis of implicit time integration schemes for wave propagations". In: *Computers and Structures* 230 (2020), p. 106188. ISSN: 0045-7949.

[86] C. Lee, K.-J. Bathe, and G. Noh. "Stability of the Bathe implicit time integration methods in the presence of physical damping". In: *Computers and Structures* 295 (2024), p. 107294.

[87] Y.-J. Lee, Y.-T. Jhan, and C.-H. Chung. "Fluid–structure interaction of FRP wind turbine blades under aerodynamic effect". In: *Composites Part B: Engineering* 43.5 (2012), pp. 2180–2191. ISSN: 1359-8368.

[88] A. Lozovskiy, M. A. Olshanskii, and Y. V. Vassilevski. "Analysis and assessment of a monolithic FSI finite element method". In: *Computers and Fluids* 179 (2019), pp. 277–288. ISSN: 0045-7930.

[89] M. Malakiyeh, S. Shojaee, S. Hamzehei-Javaran, and K.-J. Bathe. "New insights into the β_1/β_2-Bathe time integration scheme when L-stable". In: *Computers and Structures* 245 (Mar. 2021), p. 106433.

[90] M. M. Malakiyeh, S. Shojaee, and K.-J. Bathe. "The Bathe time integration method revisited for prescribing desired numerical dissipation". In: *Computers and Structures* 212 (2019), pp. 289–298. ISSN: 0045-7949.

[91] H. G. Matthies and J. Steindorf. "Partitioned strong coupling algorithms for fluid–structure interaction". In: *Computers and Structures* 81.8 (2003). K.J Bathe 60th Anniversary Issue, pp. 805–812. ISSN: 0045-7949.

[92] C. Michler, S. J. Hulshoff, E. H. van Brummelen, and R. de Borst. "A monolithic approach to fluid-structure interaction". In: *Computers and Fluids* 33 (2004), pp. 839–848. ISSN: 0045-7930.

[93] N. M. Newmark. "A method of computation for structural dynamics". In: *Journal of the engineering mechanics division* 85.3 (1959), pp. 67–94.

[94] K. Nilsson and F. Tornberg. "On blowdown analysis with efficient and reliable direct time integration methods for wave propagation and fluid-structure-interaction response". In: *Computers and Structures* 216 (2019), pp. 1–14. ISSN: 0045-7949.

[95] F. Nobile and C. Vergara. "An effective fluid-structure interaction formulation for vascular dynamics by generalized Robin conditions". In: *SIAM Journal on Scientific Computing* 30.2 (2008), pp. 731–763.

[96] G. Noh and K.-J. Bathe. "The Bathe time integration method with controllable spectral radius: The ρ_∞-Bathe method". In: *Computers and Structures* 212 (Feb. 2019), pp. 299–310.

[97] K. Ogata. *Discrete-time Control Systems*. Prentice-Hall International Editions. Prentice-Hall, 1987. ISBN: 9780132161022.

[98] D. W. Olson, S. F. Wolf, and J. M. Hook. "The tacoma narrows bridge collapse". In: *Physics today* 68.11 (2015), pp. 64–65.

[99] E. Oñate, I. de Pouplana, and F. Zárate. "Explicit time integration scheme with large time steps for first order transient problems using finite increment calculus". In: *Computer Methods in Applied Mechanics and Engineering* 402 (2022). A Special Issue in Honor of the Lifetime Achievements of J. Tinsley Oden, p. 115332. ISSN: 0045-7825.

[100] K. C. Park. "An Improved Stiffly Stable Method for Direct Integration of Nonlinear Structural Dynamic Equations". In: *Journal of Applied Mechanics* 42.2 (June 1975), pp. 464–470. ISSN: 0021-8936.

[101] M. Pfaller, J. Hörmann, M. Weigl, A. Nagler, R. Chabiniok, C. Bertoglio, and W. Wall. "The importance of the pericardium for cardiac biomechanics: From physiology to computational modeling". In: *Biomechanics and Modeling in Mechanobiology* 18 (Apr. 2019). DOI: 10.1007/s10237-018-1098-4.

[102] A. Presas, Y. Luo, Z. Wang, and B. Guo. "Fatigue life estimation of Francis turbines based on experimental strain measurements: Review of the actual data and future trends". In: *Renewable and Sustainable Energy Reviews* 102 (2019), pp. 96–110. ISSN: 1364-0321.

[103] A. Quarteroni, R. Sacco, and F. Saleri. *Numerical Mathematics*. Springer Berlin Heidelberg, 2006. ISBN: 9783540346586.

[104] R. Raible. "A simplification of Jury's tabular form". In: *IEEE Transactions on Automatic Control* 19.3 (1974), pp. 248–250. DOI: 10.1109/TAC.1974.1100574.

[105] R. H. Raible. "A Simplification of Jury's Tabular Form". In: *IEEE Transactions on Automatic Control* 19.3 (1974), pp. 248–250.

[106] P. Ryzhakov, J. M. Marti, and N. Dialami. "A Unified Arbitrary Lagrangian–Eulerian Model for Fluid–Structure Interaction Problems Involving Flows in Flexible Channels". In: *Journal of Scientific Computing* 90 (Mar. 2022).

[107] L. A. Sangalli and A. L. Braun. "A fluid-structure interaction model for numerical simulation of bridge flutter using sectional models with active control devices. Preliminary results". In: *Journal of Sound and Vibration* 477 (2020), p. 115338. ISSN: 0022-460X.

[108] R. Sevilla, A. J. Gil, and M. Weberstadt. "A high-order stabilised ALE finite element formulation for the Euler equations on deformable domains". In: *Computers and Structures* 181 (2017), pp. 89–102. ISSN: 0045-7949.

[109] T. Spenke, M. Make, and N. Hosters. "A Robin-Neumann scheme with quasi-Newton acceleration for partitioned fluid-structure interaction". In: *International Journal for Numerical Methods in Engineering* 124.4 (2023), pp. 979–997.

[110] T. E. Tezduyar, S. Sathe, T. Cragin, B. Nanna, B. S. Conklin, J. Pausewang, and M. Schwaab. "Modelling of fluid–structure interactions with the space–time finite elements: Arterial fluid mechanics". In: *International Journal for Numerical Methods in Fluids* 54.6-8 (2007), pp. 901–922.

[111] R. Torii, M. Oshima, T. Kobayashi, K. Takagi, and T. E. Tezduyar. "Computer modeling of cardiovascular fluid–structure interactions with the deforming-spatial-domain/stabilized space–time formulation". In: *Computer Methods in Applied Mechanics and Engineering* 195.13 (2006). A Tribute to Thomas J.R. Hughes on the Occasion of his 60th Birthday, pp. 1885–1895. ISSN: 0045-7825.

[112] H. Van Brummelen. "Added Mass Effects of Compressible and Incompressible Flows in Fluid-Structure Interaction". In: *Journal of Applied Mechanics* 76 (Mar. 2009), pp. 021206–. DOI: 10.1115/1.3059565.

[113] V. Vatsa, M. Carpenter, and D. Lockard. "Re-evaluation of an Optimized Second Order Backward Difference (BDF2OPT) Scheme for Unsteady Flow Applications". In: *48th AIAA Aerospace Sciences Meeting Including the New Horizons Forum and Aerospace Exposition* (Jan. 2010).

[114] W. Wall. *Fluid–structure interaction with stabilized finite elements*. 1999.

[115] X. Wang, X. Yue, H. Dai, H. Feng, and S. Atluri. *Computational Methods for Nonlinear Dynamical Systems: Theory and Applications in Aerospace Engineering*. Elsevier Science, 2022. ISBN: 9780323991131.

[116] W. Wen, K. Wei, H. Lei, S. Duan, and D. Fang. "A novel sub-step composite implicit time integration scheme for structural dynamics". In: *Computers and Structures* 182 (2017), pp. 176–186.

[117] a. Wheaton Richard. *Numerical Simulation Methods for Predicting Reservoir Performance*. 1st ed. Amsterdam, [Netherlands] : Gulf Professional Publishing, 2016. ISBN: 0-08-101019-2.

[118] E. L. Wilson. *A computer program for the dynamic stress analysis of underground structures*. Tech. rep. University of California, Berkeley, 1962.

[119] K. K. L. Wong, P. Thavornpattanapong, S. C. P. Cheung, and J. Tu. "Numerical Stability of Partitioned Approach in Fluid-Structure Interaction for a Deformable Thin-Walled Vessel". In: *Computational and Mathematical Methods in Medicine* 2013.1 (2013), p. 638519.

[120] C. Wood, A. Gil, O. Hassan, and J. Bonet. "Partitioned block-Gauss–Seidel coupling for dynamic fluid–structure interaction". In: *Computers and Structures* 88.23 (2010). Special Issue: Association of Computational Mechanics – United Kingdom, pp. 1367–1382. ISSN: 0045-7949.

[121] Y. Xu and Y. T. Peet. "Verification and convergence study of a spectral-element numerical methodology for fluid-structure interaction". In: *Journal of Computational Physics: X* 10 (2021), p. 100084. ISSN: 2590-0552.

[122] J. Zhang, Y. Liu, and D. Liu. "Accuracy of a composite implicit time integration scheme for structural dynamics". In: *International Journal for Numerical Methods in Engineering* 109.3 (2017), pp. 368–406.

[123] J. Zhang, M. Chen, B. Shen, D. Zhang, and S. C. P. Cheung. "Numerical approaches to capture fluid–structure interaction considering interfaces for offshore structures". In: *International Journal of Fluid Engineering* 2.2 (Jan. 2025), p. 020601. ISSN: 2994-9009.

[124] O. Zienkiewicz, R. Taylor, and P. Nithiarasu. *The Finite Element Method for Fluid Dynamics*. The Finite Element Method. Butterworth–Heinemann, 2013. ISBN: 9780080951379.

Appendix A.The Jury Stability Criterion

The root distribution of the characteristic polynomial with respect to the unit circle is a fundamental indicator of stability in discrete-time systems. To examine the root distribution and evaluate system stability, several analytical methods can be employed, including the Schur–Cohn stability criterion, the Jury stability criterion, and the bilinear transformation combined with the Routh–Hurwitz criterion [97].

A.1. Constructing the Jury Table

The Jury stability criterion offers an algebraic method for determining the stability of discrete-time systems by applying a sequence of numerical tests to the coefficients of the characteristic polynomial [25, 104]. These tests are organised into what is known as the Jury table, where each subsequent row is systematically derived from the previous one. By evaluating specific conditions from this table, the criterion determines whether the system's poles lie within the unit circle, thus establishing stability or instability.

Consider the characteristic polynomial

$$F(z) = a_n z^n + a_{n-1} z^{n-1} + \cdots + a_1 z + a_0. \tag{A.1}$$

A system is said to be stable if all roots of $F(z)$ lie within the unit circle, that is, $|z| < 1$. To evaluate this, the coefficients of $F(z)$ are arranged to form the Jury table (Table A.1), from which the stability conditions are derived.

Table A.1.: Formation of the Jury Table.

a_n	a_{n-1}	a_{n-2}	$\cdots$	a_2	a_1	a_0	k_a
b_0	b_1	b_2	$\cdots$	b_{n-2}	b_{n-1}	–	k_b
c_0	c_1	c_2	$\cdots$	c_{n-2}	–	–	k_c
$\vdots$	$\vdots$	$\vdots$	$\ddots$	$\vdots$	$\vdots$		$\vdots$
ζ_0	ζ_1						k_ζ
ω_0							

where

$$k_a = \frac{a_0}{a_n}, \qquad k_b = \frac{b_{n-1}}{b_0}, \qquad k_i = \frac{c_{n-2}}{c_0}, \quad \ldots, \quad k_\zeta = \frac{\zeta_1}{\zeta_0}, \tag{A.2}$$

and the coefficients are calculated recursively as

$$\begin{aligned} b_{n-i} &= a_{n-i+1} - k_a a_{i-1}, && \text{for } i = 1, 2, \ldots, n, \\ c_{n-i} &= b_{n-i+1} - k_b b_{i-2}, && \text{for } i = 2, 3, \ldots, n, \\ &\vdots \\ \omega_0 &= \zeta_0 - k_\zeta \zeta_1. \end{aligned} \tag{A.3}$$

Note that this procedure applies to real polynomials. A minor modification is required to implement the Jury stability criterion for complex polynomials (see [25]).

A.2. Formulation of GA-23 Using the Jury Test

The characteristic polynomial of GA-23 is obtained from the first order initial value problem presented in Chapter 2, which is defined by

$$\delta_3 \, \dot{u}^{(3)}_{n+\beta} \; + \; (1 - \delta_3) \, \dot{u}^{(2)}_{n+\beta} \; - \; \lambda \, u_{n+\alpha} \; = \; 0, \tag{A.4}$$

and is expressed as follows

$$p(z) = z^3 - \frac{\Big(6\,\delta_3(\rho_\infty^3+1) + 9\,\rho_\infty(2\,\Delta t\,\lambda - 1) + 3\,\rho_\infty^2(\rho_\infty - 6) + 12\Big)\,z^2}{3\,\rho_\infty(2-\rho_\infty) + 2\,\delta_3(1+\rho_\infty^3) - 6\,\Delta t\,\lambda + 9}$$
$$+\frac{\Big(6\,\delta_3(\rho_\infty^3+1) - 9\,\rho_\infty^2(2\,\Delta t\,\lambda + 1) + 6\,\rho_\infty(2\,\rho_\infty^2 - 3) + 3\Big)\,z}{3\,\rho_\infty(2-\rho_\infty) + 2\,\delta_3(1+\rho_\infty^3) - 6\,\Delta t\,\lambda + 9}$$
$$-\frac{2\,\delta_3(\rho_\infty^3+1) + 3\,\rho_\infty^3(2\,\Delta t\,\lambda + 3) + 3\,\rho_\infty(2\,\rho_\infty - 1)}{3\,\rho_\infty(2-\rho_\infty) + 2\,\delta_3(1+\rho_\infty^3) - 6\,\Delta t\,\lambda + 9}.$$

The following stability conditions are obtained from the Jury table:

- **Condition 1:** $1 > 0$,
- **Condition 2:** $1 - \dfrac{(s_{12} - 6\,\Delta t\,\omega\,\rho_\infty^3)\,(6\,\Delta t\,\omega\,\rho_\infty^3 + s_{12})}{(s_{11} - 6\,\Delta t\,\omega)\,(s_{11} + 6\,\Delta t\,\omega)} > 0$,
- **Condition 3:** $1 - s_2 + \dfrac{(s_7 - s_3\,s_6\,s_9)\,(s_8 - s_4\,s_5\,s_{10})}{s_2 - 1} > 0$,
- **Condition 4:** $s_1 - \dfrac{1}{s_1}\left[\left(s_{10} + \dfrac{(s_7 - s_3 s_6 s_9)(s_9 - s_4 s_5 s_7)}{s_2 - 1} - s_3 s_6 s_8\right)\right.$
$$\left.\times\left(s_9 + \frac{(s_8 - s_4 s_5 s_{10})(s_{10} - s_3 s_6 s_8)}{s_2 - 1} - s_4 s_5 s_7\right)\right] > 0.$$

The parameters used in the above conditions are defined as:

$$s_1 = 1 - s_2 + \frac{(s_7 - s_3\,s_6\,s_9)\,(s_8 - s_4\,s_5\,s_{10})}{s_2 - 1}$$
$$s_2 = \frac{(-6\,\Delta t\,\omega\,\rho_\infty^3 + s_{12})\,(6\,\Delta t\,\omega\,\rho_\infty^3 + s_{12})}{(s_{11} - 6\,\Delta t\,\omega)\,(s_{11} + 6\,\Delta t\,\omega)}$$
$$s_3 = \frac{1}{(s_{11} - 6\,\Delta t\,\omega)} \qquad s_4 = \frac{1}{(s_{11} + 6\,\Delta t\,\omega)}$$
$$s_5 = s_{12} - 6\,\Delta t\,\omega\,\rho_\infty^3 \qquad s_6 = s_{12} + 6\,\Delta t\,\omega\,\rho_\infty^3$$
$$s_7 = s_3\,(s_{13} - 18\,\Delta t\,\omega\,\rho_\infty^2) \qquad s_8 = s_4\,(s_{13} + 18\,\Delta t\,\omega\,\rho_\infty^2)$$
$$s_9 = s_4\,(s_{14} - 18\,\Delta t\,\omega\,\rho_\infty) \qquad s_{10} = s_3\,(s_{14} + 18\,\Delta t\,\omega\,\rho_\infty)$$

$$s_{11} = \delta_3\, 2i + \rho_\infty\, 6i + \delta_3\, \rho_\infty^3\, 2i - \rho_\infty^2\, 3i + \Delta t\, \xi\, 6i + 9i$$

$$s_{12} = \delta_3\, 2i - \rho_\infty\, 3i + \delta_3\, \rho_\infty^3\, 2i + \rho_\infty^2\, 6i + \rho_\infty^3\, 9i - \Delta t\, \rho_\infty^3\, \xi\, 6i$$

$$s_{13} = 3(\delta_3\, 2i - \rho_\infty\, 6i + \delta_3\, \rho_\infty^3\, 2i - \rho_\infty^2\, 3i + \rho_\infty^3\, 4i + \Delta t\, \rho_\infty^2\, \xi\, 6i + 1i)$$

$$s_{14} = 3(\delta_3\, 2i - \rho_\infty\, 3i + \delta_3\, \rho_\infty^3\, 2i - \rho_\infty^2\, 6i + \rho_\infty^3\, 1i - \Delta t\, \rho_\infty\, \xi\, 6i + 4i)$$

To ensure physical consistency, the following constraints are imposed:

$$\Delta t \geq 0, \qquad \xi \geq 0, \qquad \omega \geq 0, \qquad 0 \leq \rho_\infty \leq 1.$$

The stability analysis yields the following criteria for the parameter δ_3:

- Condition 1 is always satisfied.
- Condition 2 is satisfied if $\delta_3 \geq \dfrac{9\rho_\infty^2 - 6\rho_\infty + 9}{4\rho_\infty - 4\rho_\infty^2 - 4}$.
- Condition 3 is satisfied if $\delta_3 \geq \dfrac{3\rho_\infty^2 - 6\rho_\infty + 3}{2\rho_\infty - 2\rho_\infty^2 - 2}$.
- Condition 4 is satisfied if $\delta_3 \geq \dfrac{\rho_\infty^2 - 2\rho_\infty + 1}{2\rho_\infty^2 - 2\rho_\infty + 2}$.

The expression

$$\delta_3 = \frac{\rho_\infty^2 - 2\rho_\infty + 1}{2\rho_\infty^2 - 2\rho_\infty + 2} \tag{A.5}$$

satisfies all four stability requirements and therefore guarantees a stable GA-23 formulation. The same methodology is applied to GA-234 to determine the value of δ_4; however, the algebraic manipulation is extensive, and the resulting expressions are omitted here for brevity.